A Thesis Submitted for the Degree of PhD at the University of Warwick

Permanent WRAP URL:

http://wrap.warwick.ac.uk/163615
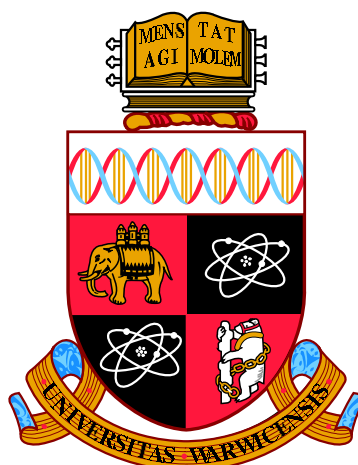
warwick.ac.uk/lib-publications

Symmetry Adapted Analysis of Lattice Dynamics and Local Distortions in Perovskite Related Materials

by

Tobias A. Bird

Thesis

Submitted to the University of Warwick

in partial fulfillment of requirements

for admissision to the degree of

Doctor of Philosophy

Department of Chemistry

August 2021

Contents

List of Tables

List of Figures

Acknowledgments

Firstly, I would like to thank my primary PhD supervisor, Mark Senn. Without Mark's encouragement and reassurance this work would have not been possible. Likewise, I would also like to thank my other supervisor, Nicholas Bristowe, who has provided me much assistance both at the start and end of my PhD.

I would like to thank all members of the Senn Group for making it an enjoyable environment to work and research in. In particular, thanks go to Gabriel Clarke, for being the other half of the early Senn Group and helping us both not go insane in an empty office, Jere Tidey, for providing a lot of helpful guidance in preparing this document, and Anna Herlihy, whose rigorous beta testing has helped make this work possible. I would also like to thank all the collaborators that have contributed to the work presented in this thesis.

I would additionally like to thank the students and staff at the MAS CDT, who have helped make the Masters' year, and all our conferences, enjoyable and engaging. I would particularly like to thank Aron Summer, for taking all the bad luck with experiments, and providing many useful discussions about total scattering.

I would also like to thank my parents for encouraging me to pursue a PhD and my friends for supporting me along the way. Finally, I would like to thank everyone involved with the Big Band for helping make the almost 9 years I have spent at Warwick an extremely enjoyable time.

Declarations

This thesis is submitted to the University of Warwick in support of my application to the degree of Doctor of Philosophy. It takes the form of a thesis by publication, where chapter 3 [Bird *et al.*, *Phys. Rev. B*, 2020, **101**, 064306] has been previously published and chapters 2, 4 and 5 have been submitted for publication. Chapters 4 and 5 are available on arXiv, with the identifiers 2108.03006 and 2108.05751

The work in this thesis has been carried out by the author except in the cases outlined below:

- Neutron pair distribution function data for $BaTiO_3$ used in the first presented paper was originally published in Senn *et al.*, *Phys. Rev. Lett.*, 2016, **116**, 207602

- X-ray pair distribution function data for $CaZrF_6$ in the second presented paper were generated by Jun Chen and L. Hu from total scattering data acquired by Y. Ren

- Neutron pair distribution function data for ReO_3 in the third presented paper were acquired and generated by A. E. Phillips and M. G. L. Wilkinson

- Density Functional Theory calculations in the third and fourth presented papers were carried out by N. C. Bristowe

- Sample preparation for the fourth presented paper was carried out by Jungshen Chen ($MAPbI_3$) and C. Stock ($MAPbBr_3$ and $MAPbCl_3$)

Abstract

The work presented in this thesis considers the effect of dynamic and static distortions on the local structure of perovskite-related materials. I systematically interrogate the pair distribution functions of the materials against phonon eigenvectors, determined using representation theory. I present the method for performing this Symmetry-Adapted Pair Distribution Function Analysis (SAPA) in chaper 2.

In the chapters 3 and 4, I perform this SAPA technique on the negative thermal expansion (NTE) materials ScF_3, $CaZrF_6$ and ReO_3. NTE is usually viewed as originating from a vibrational tension effect, commonly realised in materials *via* cooperative rotations of atomic polyhedra, termed rigid unit modes (RUMs). The results of our SAPA analysis show that scissoring modes, which distort the octahedral bond angles, dominate the local structure in ScF_3 and $CaZrF_6$ but not ReO_3, rather than the RUMs one might expect. I therefore conclude that structural flexibility is a key determining factor in the extent and magnitude of NTE observed in a material.

This theme of the importance of structural flexibility, in the form of scissoring modes, continues in the final results chapter. In this work, the local structure of the cubic phases of the methylammonium lead halides are analysed using the SAPA technique. We find that in all three hybrid perovskites studied, scissoring modes again describe the largest deviation from the average structure. These modes have a larger amplitude for these hybrid perovskites than for ScF_3, despite the presence of A-sites in the former. Using Density Functional Theory calculations, we show that these modes are linked to an opening of the electronic band gap.

Abbreviations

- ADP - anisotropic displacement parameter

- beq - B-factor equivalent

- BWMA - Boltzmann Weighted Mode Amplitude

- BZ - Brillouin Zone

- CBM - conduction band minimum

- CIF - crystallographic information file

- $D(g)$ - representation matrix of g

- DFT - density functional theory

- DOS - density of states

- g - symmetry element

- G - group

- irrep - irreducible representation

- MA - Methylammonium

- NMR - nuclear magnetic resonance

- NTE - negative thermal expansion

- OPD - order parameter direction

- PDF - pair distribution function

- PAW - projector augmented wave

- PTE - positive thermal expansion

- R_{wp} - weighted-phase R-factor

- RMC - reverse Monte Carlo

- RUM - rigid unit mode

- S - vector space of displacements

- SAPA - symmetry-adapted pair distribution function analysis

- SOC - spin-orbit coupling

- VASP - Vienna Ab Initio Simulation Package

- VBM - valence band maximum

- VdW - Van der Waals

Chapter 1

Introduction

1.1 Background and Motivation

The aim of this thesis is to present a novel technique for analysing the local structure of crystalline compounds by determining how the local structure deviates from the average structure. By doing this, we want to obtain insight into the materials properties. The dynamic distortions in a solid, which in quantum mechanics are described in terms of vibrational quanta named phonons, heavily influence the properties of a material and are the origin of some of the most fundamental physical processes, such as thermal expansion. The measure of local structure used for this work is the pair distribution function (PDF) which is obtained *via* the total scattering method for neutron and X-ray powder diffraction. I develop here a symmetry motivated approach to analysing PDFs that is based on using representation theory to construct a basis set of a "distortion space" in terms of zone-centre and zone-boundary displacements.

The motivation behind this work was to produce a technique which uses pair distribution functions to analyse distortions. Current methods, as discussed in section 1.2.11, introduce user input bias into the analysis, whereas the method we have developed uses only the symmetry of the structure to be studied as an input, thereby reducing the bias. The first presented paper details how to perform our developed technique, which we term symmetry-adapted PDF analysis. The remaining papers present applications of this technique to the negative thermal expansion materials ScF_3, $CaZrF_6$ and ReO_3 and the photovoltaic materials $(CH_3NH_3)PbX_3$, $X = I$, Br, Cl.

The analysis of the negative thermal expansion materials ScF_3, $CaZrF_6$ and ReO_3 was motivated for two primary reasons. The first is that they are simple, high

symmetry structures, so provide a good test case for our novel analysis method. The second is that despite the structural simplicity, the origin of phonon-driven negative thermal expansion is still not fully understood, with the traditional rigid unit mode model of NTE being challenged in recent years. Our analysis gives support to the idea that rigid unit modes, soft in these materials due to an incipient phase transition with applied pressure, are a key determinating factor for the presence of NTE, but that the flexibility of the structure plays a large role in the magnitude and temperature range of NTE. This structural flexibility gives a greater number of quasi-RUMs, modes with mixed RUM and octahedral deformation character, a negative Grüneisen parameter.

The motivation for the study on the methylammonium lead halides is that despite them being very promising candidate materials for low cost and high efficiency solar cells, the origin of their desirable properties as photovoltaics is still to be determined. We show that large amplitude scissoring modes are a dominant distortion in the cubic phases of these hybrid perovskites, which have the effect of opening up the band gap significantly. We also provide evidence that the organic cation and inorganic framework dynamics are linked.

1.2   Structure Determination

The primary method used in this work is the total scattering method. This is an extension of neutron and X-ray powder diffraction where as much of the scattering information as possible is collected during the experiment. The collected powder pattern will not only include information on the average structure from the sharp Bragg peaks, but will also contain information on local order. This local structural information appears in the data as fluctuations at high values of the scattering vector, Q, (Fig 1.1), so the Q-range for these experiments is maximised. This information is extracted by careful treatment of the data, such as subtracting any systematic contribution from the sample environment and modelling contributions from factors such as how densely packed the sample is within its environment. This section will first introduce the basics of crystallography. Following this, the theory of X-ray and neutron diffraction from the average crystal structure is presented and then extended to the formalism of total scattering. The processes used to generate the X-rays and neutrons for diffraction experiments and the analysis of diffraction data are also discussed.
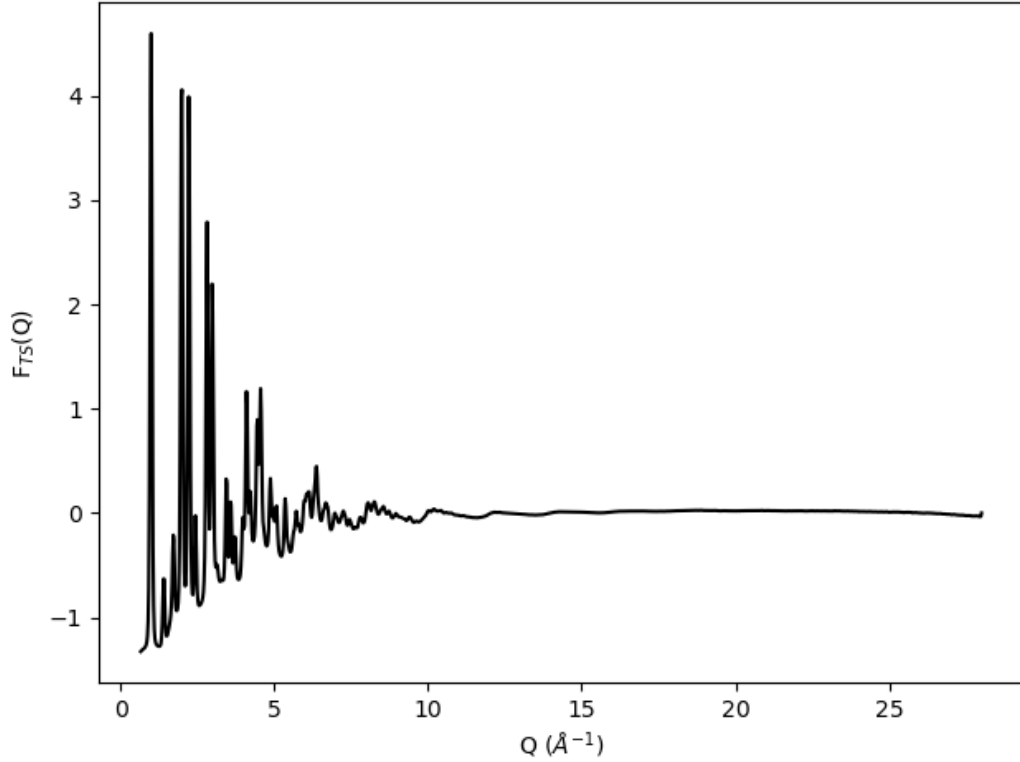
Figure 1.1: A plot of the total scattering structure factor for CsPbI$_3$ after data treatment has been performed. This shows the difference between a total scattering experiment and a traditional powder experiment. In the latter, the goal is to collect as high resolution as possible data for the low Q region, since it contains all the Bragg scattering. In the former, Q-resolution is often sacrificed so the Q-range can be maximised. These data was collected on the I15-1 beamline at Diamond Light Source. A wavelength of $\lambda = 0.161\,669\,\text{Å}$ was used.

1.2.1 Crystallography

The field of crystallography is the study of materials whose structure consists of a periodic arrangement of atoms. The structure of these crystalline materials can be described by a unit cell, the repeat unit of the periodic structure, and the lattice on which the unit cell is tiled. The lattice is characterised by its dimensions and centering. The dimensions of a lattice are described using three lattice parameters a, b and c (often termed lattice vectors when describing them in cartesian coordinates) and the angles between them, α, β and γ[5]. The simplest type of lattice, one with lattice points only at the cell corners, is termed primitive and denoted by P. Sometimes however the primitive cell does not fully describe the symmetry of the lattice, so more complex cells are used. These are body-centred (I), with an extra

3

atom at the point ($\mathbf{a}/2$, $\mathbf{b}/2$, $\mathbf{c}/2$) in unit cell coordinates; face-centred (F), with an extra atom at the centre of each face, and end-centred (A, B or C), with an extra atom at the centre of each of a pair of parallel faces. In addition, a hexagonal cell can be rhombohedrally-centered (R), with two additional lattice points along one body diagonal of the cell. In 3-dimensional space, there are 14 possible lattices, defined in Table 1.1, which were classified by Auguste Bravais in 1850 and hence termed Bravais lattices. The unit cell describes the positions of the atoms relative to one another and the symmetry elements that relate atoms therein. The combination of Bravais lattice and possible symmetry elements, including translational symmetry elements such as glide and screw axes, gives rise to 230 distinct space groups to describe the crystal symmetry[6]. The basic aim of crystallography is to be able to describe the structure of any solid state material through a choice of a space group, lattice parameters and a set of fractional coordinates. This is important since the structure of a material is a key factor in determining what properties it may have. For example, a material that crystallises in a centrosymmetric space group, *i.e.*, the space group has a centre of inversion, will not be able to exhibit proper ferroelectricity since polar distortions necessarily break this symmetry. In this thesis, the Hermann-Mauguin space group notation is used. In this notation, the first (capital) letter describes the lattice centering. The subsequent characters give the highest order symmetry operation along a particular axis. The axes that these labels refer to differ for different lattices. For example, the labels in orthorhombic lattices refer to the [1 0 0], [0 1 0] and [0 0 1] axes, but in cubic systems these are equivalent, so the first label refers to all 3 of those directions, the second to the <1 1 1> directions and the third typically to <1 1 0> directions.

The origin of crystallographic experiments dates back to the 17th century, when it was noticed that crystals of the same type will have the same angles between their faces. Later work by William Miller classified these faces using 3 integers *hkl*, a notation which is still used in modern crystallography. In the late 18th and early 19th centuries, René Juste Haüy broke down crystals into as small pieces as he could, and came to the conclusion that crystals were formed from orderly arrangements of "integrant molecules". Theoretical ideas of crystal symmetry built upon this work, but these ideas could not be experimentally confirmed until the advent of X-ray diffraction in the early 20th century and the work of Max von Laue, William H. and William L. Bragg, amongst others[7]. This technique, along with its sister technique of neutron diffraction, allows for the complete structural determination of a crystal and these techniques form the core of a modern crystallographer's toolbox.

Table 1.1: The different types of Bravais lattices. Where a lattice length does not appear in an entry, it means there is no restriction on it for that lattice type. * Note that by convention, lattices with rhombohedral symmetry are usually assigned a rhombohedrally-centered hexagonal cell rather than a primitive rhombohedral cell.

Unit Cell	Lattice Lengths	Lattice Angles	Centering
Cubic	$a = b = c$	$\alpha = \beta = \gamma = 90°$	P, I, F
Hexagonal	$a = b$	$\alpha = \beta = 90°, \gamma = 120°$	P, R^*
Rhombohedral	$a = b = c$	$\alpha = \beta = \gamma \neq 90°$	P
Tetragonal	$a = b \neq c$	$\alpha = \beta = \gamma = 90°$	P, I
Orthorhombic	$a \neq b \neq c$	$\alpha = \beta = \gamma = 90°$	P, I, F, A, B, C
Monoclinic	$a \neq c$	$\alpha = \gamma = 90°, \beta \neq 90°$	P, A, B, C
Triclinic		All other cases	P

1.2.2 Diffraction

It is a fundamental property of waves, or beams of wave-like particles, that the wave-fronts spread out and bend when incident on the corner of an obstacle, or when travelling through a gap in an obstacle. This phenomenon is known as diffraction. The diffracted wave acts as a spherical wave emanating from the gap causing the diffraction. If a wave is incident on multiple diffraction gaps, a so-called "diffraction grating", it will result in a series of spherical waves which interfere with each other, either reinforcing or cancelling. In neutron and X-ray diffraction, a regular array of atoms acts like a diffraction grating, producing a regular array of scattered waves. For most scattering angles, the individual intensities of these scattered waves cancel out, but for some, they combine in phase and are reinforced, producing a series of tight beams. When incident upon a detector, these beams form spots, the arrangement and varied intensities of which is known as a diffraction pattern. Constructive interference occurs for scattering angles where the path length between waves is equal to an integer number of wavelengths. Since the distance travelled by two waves after leaving the sample until they reach a particular point on a detector will be the same for both waves, any difference in path length will be caused by a difference in distance travelled within the sample (Fig 1.2). The picture becomes clearer if we consider the particle view of an incident beam of X-rays or neutrons. If we have a beam of our diffraction probe of choice incident at an angle, θ, to the normal of the sample surface, it could either scatter from the first plane of atoms or any subsequent plane. If the planes are separated by a distance, d, for example, this leads to an extra $2d \sin \theta$ travelled for scattering from the second plane. This
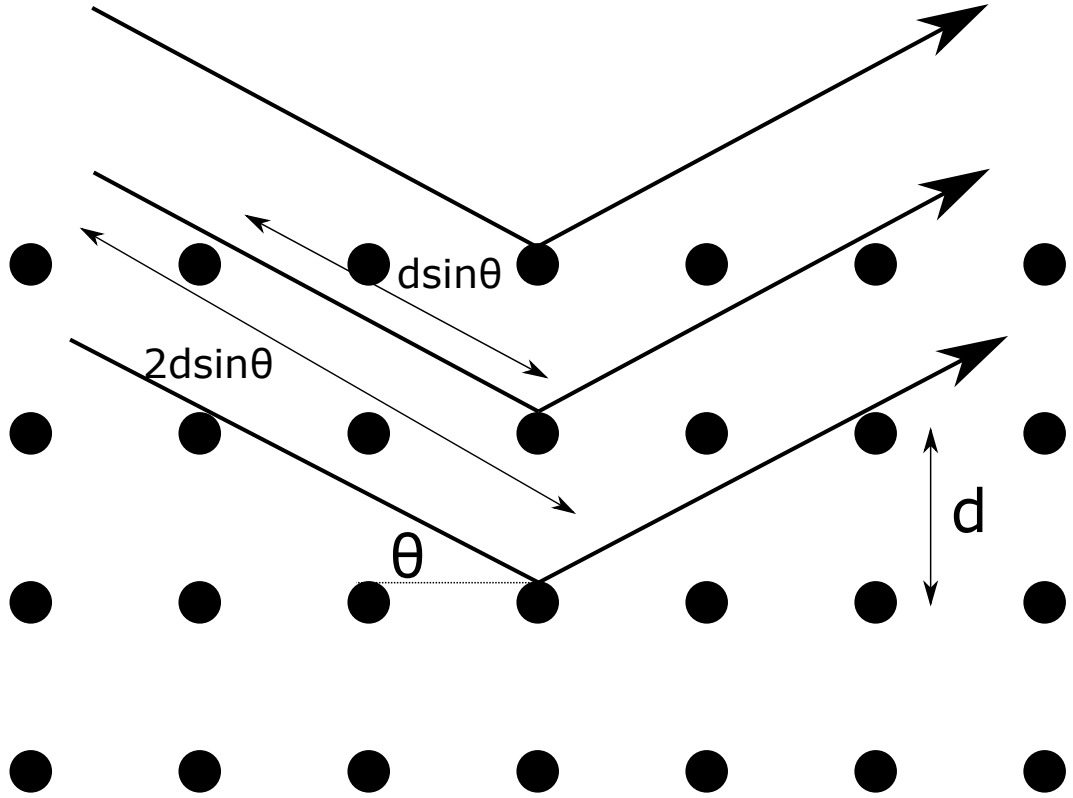
Figure 1.2: A diagram showing how a difference in path length of $2d\sin\theta$ can arise due to scattering of radiation from subsequent planes of atoms in a crystal.

idea is captured by Bragg's law:

$$n\lambda = 2d_{hkl}\sin\theta \qquad (1.1)$$

where λ is the wavelength of the incident radiation, d_{hkl} is the interplanar spacing and n is an integer[8]. The subscript of hkl in the interplanar spacing refers to the Miller index of the crystallographic plane, named after the aforementioned William Miller. The Miller index, usually written as $(h\ k\ l)$ for an individual plane or $\{h\ k\ l\}$ for a set of symmetry equivalent planes, denotes a plane that intercepts the unit cell at the points $\mathbf{a}/h$, $\mathbf{b}/k$ and $\mathbf{c}/l$, where $\mathbf{a}$, $\mathbf{b}$ and $\mathbf{c}$ are the lattice vectors of the unit cell.

The Laue conditions are another way to express the relationship between diffraction patterns and the incident radiation[9]. For an incident wave to be

diffracted by a crystal, the following must be satisfied:

$$\mathbf{a} \cdot \mathbf{Q} = 2\pi h \tag{1.2}$$

$$\mathbf{b} \cdot \mathbf{Q} = 2\pi k \tag{1.3}$$

$$\mathbf{c} \cdot \mathbf{Q} = 2\pi l \tag{1.4}$$

where h, k and l are Miller indices, $\mathbf{a}$, $\mathbf{b}$ and $\mathbf{c}$ are lattice vectors and $\mathbf{Q}$ is the scattering vector. The scattering vector, also known as the momentum transfer, is given by the difference between the incident and scattered wave vectors. For elastic scattering, $|\mathbf{Q}| = \frac{4\pi \sin \theta}{\lambda}$. This will become an important property when discussing total scattering. If these conditions are rearranged to isolate $\mathbf{Q}$, we get the concept of a reciprocal lattice. The reciprocal lattice is a Fourier transform of the real space crystal lattice, with vectors $\mathbf{a}^* = (\mathbf{b} \times \mathbf{c})/V$, $\mathbf{b}^* = (\mathbf{a} \times \mathbf{c})/V$ and $\mathbf{c}^* = (\mathbf{a} \times \mathbf{b})/V$ where V is the real space volume of the unit cell. The Laue condition tells us that the scattering vector can be expressed in terms of integer numbers of these reciprocal lattice vectors. This indicates that the image formed on a 2D detector by a beam of X-rays or neutrons incident on a single crystal will be a 2-dimensional projection of the reciprocal space. To get a full view of the structure from single crystal experiments, the diffraction pattern must be taken for different orientations of the crystal with respect to the incident radiation.

The focus of this thesis is on powder diffraction, where instead of diffraction from a single crystal we observe scattering from a powder that is formed from a large number of small crystallites which are randomly oriented with respect to each other. This has the effect of smearing out the diffraction spots into rings (Fig 1.3). The beam of radiation producing the pattern sees all the possible lattice plane spacings at the same time, meaning the experiments are typically much quicker than those of single crystal work. Planes with different d-spacings will give rise to rings at different angles from the path of the incident beam which has the effect of superimposing symmetry-equivalent reflections, e.g., the {1 0 0} reflections of a cubic structure. The pattern of rings on the detector is then radially integrated to give data in the form of intensity *vs.* scattering angle. This is subsequently modelled using computer software and a computed diffraction pattern is compared to the experimental one. The impact that simple properties of the crystal, such as the size of the lattice, has upon the diffraction pattern can be seen using Bragg's law. For example, if we are studying two samples with the same structure but one has larger lattice parameters, the peaks will shift to a lower scattering angle (2θ) since $\sin \theta$ will have to decrease
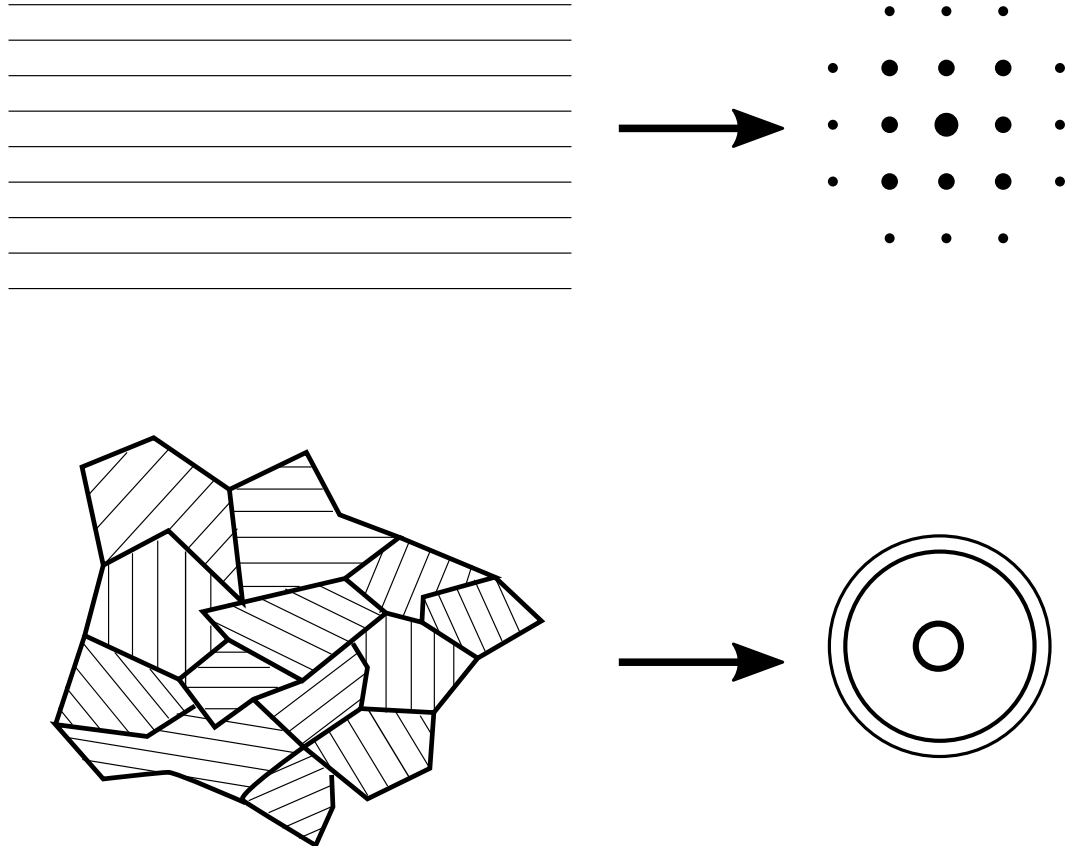
Figure 1.3: A diagram showing the qualitative difference between diffraction from a single crystal and diffraction from a powder of randomly oriented crystallites.

to compensate for the increased lattice spacings. To see how more complex factors affect the diffraction pattern, such as the arrangement of atoms in the unit cell, we move on to a more in depth discussion of diffraction theory.

1.2.3 Diffraction Theory

The principles underpinning the scattering of X-rays and neutrons by a crystal is similar and, therefore, the theory of diffraction will initially be discussed in terms of generic particles. For a beam of particles with an incident flux of I_0, the scattered flux (the number of scattered particles per unit area per unit time) is given by

$$I_s \propto I_0 \Delta\Omega \frac{d\sigma}{d\Omega} \qquad (1.5)$$

where $\Delta\Omega$ is the unit solid angle and $\frac{d\sigma}{d\Omega}$ is the differential cross section. The intensity of the scattered beam is also affected by factors such as absorbance, in-

coherent scattering and multiple scattering events. Using Fermi's Golden Rule that the differential cross-section will be proportional to the matrix element $| < Final|Interaction|Initial > |^2$[10, 11], we can get an expression for the differential cross-section. Scattering is an elastic process, and we assume that the wave before and after scattering are plane waves with wavevectors $\mathbf{k}_i$ and $\mathbf{k}_f$ respectively, with $|\mathbf{k}_i| = |\mathbf{k}_f|^1$. If the incoming particles are scattered by some potential, $V(r)$, then we have:

$$\frac{d\sigma}{d\Omega} \propto \left| \int_V \exp[-i(\mathbf{k}_f \cdot \mathbf{r})]V(\mathbf{r})\exp[i(\mathbf{k}_i \cdot \mathbf{r})]d^3\mathbf{r} \right|^2 \tag{1.6}$$

which, using the definition of the scattering vector $\mathbf{Q} = \mathbf{k}_i - \mathbf{k}_f$, simplifies to

$$\frac{d\sigma}{d\Omega} \propto \left| \int_V V(\mathbf{r})\exp[i(\mathbf{Q} \cdot \mathbf{r})]d^3\mathbf{r} \right|^2 \tag{1.7}$$

This efectively constitutes a Fourier transform of the scattering potential, which has the same periodicity as the crystal lattice. Therefore, to simulate a diffraction pattern, we need to determine the form of the scattering potential for X-rays and neutrons.

1.2.4   X-ray Scattering

X-rays are a form of electromagnetic radiation and are consequently scattered by the electrons surrounding the atoms which comprise the crystal. The scattering power for an X-ray incident on a single electron is e^2/mc^2[14]. The ratio of the amplitude of the X-ray scattered from an atom compared to that scattered by a single electron, termed the atomic form factor, is given by

$$f = \int_V \rho(\mathbf{r})\exp[i(\mathbf{Q} \cdot \mathbf{r})]d^3\mathbf{r} \tag{1.8}$$

where $\rho(\mathbf{r})$ is the number density of electrons surrounding the nucleus. X-rays scatter from a cloud of electrons of finite size, resulting in a path difference between X-rays scattered from different points of the cloud for non-zero scattering angles. Therefore, the atomic scattering factors decrease with increasing $\sin\theta/\lambda$ (Fig 1.4)[5, 1].

Since the atomic number $Z = \int_V \rho(\mathbf{r})d^3\mathbf{r}$, heavier elements display stronger scattering.

---

[1]This approximation is known as the Born approximation[12, 13]

9
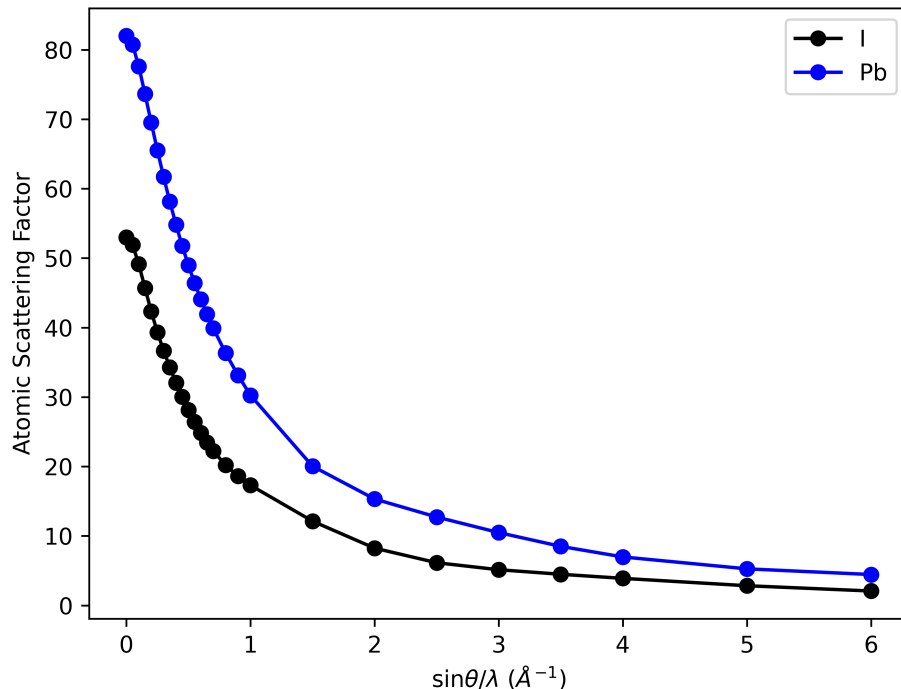
Figure 1.4: A plot showing the decrease in atomic scattering factors for Pb and I for increasing $\sin\theta/\lambda$. The values plotted are taken from the International Tables of Crystallography.[1]

1.2.5 Neutron Scattering

Neutrons are characterised by a wavevector, $\mathbf{k}$, determined by its de Broglie wavelength and also by a spin, σ. Neutrons can, therefore, interact with either the nucleus of an atom *via* the strong force or with any magnetic moment the atoms may have. Neutron diffraction from magnetic materials is beyond the scope of this thesis, so only the neutron-nuclear interaction will be discussed.

Since the interaction between the neutron and the nucleus occurs *via* the strong force, it tends to be of an "all-or-nothing" nature. Hence, we can approximate the scattering potential, $V(\mathbf{r})$, to be some constant, A, within a radius r_0 and zero outside this radius. We can define an atomic scattering factor for neutrons as

$$f = \int_V V(\mathbf{r}) \exp[i(\mathbf{Q} \cdot \mathbf{r})] d^3\mathbf{r} \tag{1.9}$$

Since $r_0 << |\mathbf{Q}|$ (the range of the nuclear potential is several orders of magni-

tude smaller than the wavelengths of neutrons used in diffraction experiments), $\exp[i(\mathbf{Q} \cdot \mathbf{r})] \approx 1$ and we have $f = A\left(\frac{4\pi r_0^3}{3}\right)$. There is no additional factor of $\sin\theta/\lambda$ as the scattering is from a point source and, since the atomic scattering factor is consequently a constant, it is usually denoted by a single letter, b, also called the neutron scattering length.

Neutron scattering from isotopes of the same element can be very different and will also be affected by spin effects, so the scattering length is usually split into two parts: a coherent scattering length, $b_{coh} = \langle b \rangle$, which describes scattering from the average, and an incoherent scattering length, $b_{inc}^2 = \langle b^2 \rangle - \langle b \rangle^2$, describing the scattering from fluctuations. For elastic scattering, the incoherent scattering appears in the diffraction pattern as a background-like contribution, making isotopes with a large incoherent scattering length undesirable, especially for total scattering studies. An example of an isotope with a large incoherent scattering length is ^{1}H, which makes accurately modelling hydrogen positions in neutron diffraction difficult. Consequently, samples containing hydrogen are typically deuterated, since deutirium has an insignificant incoherent scattering length. An important difference to X-rays is that the coherent scattering length has no uniform variation with atomic number and can even be negative[2]. Consequently, this gives neutron diffraction an advantage when studying materials with a wide range of atomic numbers amongst the constituent elements, since the diffraction pattern will not necessarily be dominated by contributions from the heavy elements and light atoms may still be well resolved.

1.2.6 Diffraction from a Crystal

When viewing diffraction from a series of atoms rather than a single isolated atom, the contribution of every atom to the scattering must be taken into account. The scattering amplitude for a sample is given by:

$$\Psi(\mathbf{Q}) = \frac{1}{\langle f \rangle} \sum_j f_j \exp(i\mathbf{Q} \cdot \mathbf{R}_j) \tag{1.10}$$

where f_j and $\mathbf{R}_j$ are the atomic form factor and position of atom j, respectively, and $\langle f \rangle$ is the mean form factor[15]. If this function could be reconstructed from a diffraction pattern, then we could perfectly reconstruct both the crystal lattice and the electron density in the unit cell. Diffraction experiments, however, detect the intensity of the diffracted beam, which is proportional to the product of the

---

[2]A negative neutron scattering length means the wave function of the scattered neutron is out of phase to that of the incident neutron.

scattering amplitude with its complex conjugate:

$$\frac{d\sigma}{d\Omega} = \frac{\langle f \rangle^2}{N} |\Psi(\mathbf{Q})|^2 = \frac{1}{N} \sum_{i,j} f_i f_j \exp[i\mathbf{Q} \cdot (\mathbf{R}_i - \mathbf{R}_j)] \tag{1.11}$$

where N is the number of atoms in the sample. From equation 1.11, we can see that diffraction experiments are only sensitive to the phase difference between scattered waves from different atoms. Without the phase information, we cannot reconstruct the electron density of the unit cell without using some method of phase retrieval. This is known as the phase problem in crystallography.

If the sample is crystalline, we can split the sum in equation 1.11 into a sum over a single unit cell and a sum over the crystal lattice:

$$\frac{d\sigma}{d\Omega} = \frac{1}{n_c} \sum_{\alpha,\kappa} f_\alpha f_\kappa \exp[i\mathbf{Q} \cdot (\mathbf{r}_\alpha - \mathbf{r}_\kappa)] \sum_{n,m} \exp[i\mathbf{Q} \cdot (\mathbf{R}_n - \mathbf{R}_m)] \tag{1.12}$$

where $\mathbf{r}_\alpha$ and $\mathbf{r}_\kappa$ are the positions of atoms α and κ within the unit cell, $\mathbf{R}_n$ is a direct lattice vector and n_c is the number of unit cells within the sample. This can also be expressed as:

$$\frac{d\sigma}{d\Omega} = \frac{1}{n_c} | \sum_j f_j \exp(i\mathbf{Q} \cdot \mathbf{r}_j)|^2 | \sum_n \exp(i\mathbf{Q} \cdot \mathbf{R}_n)|^2 \tag{1.13}$$

The first of these sums can be simplified further by recalling that for diffraction to occur, the scattering vector, $\mathbf{Q}$, is a reciprocal lattice vector. Letting $\mathbf{Q} = h\mathbf{a}^* + k\mathbf{b}^* + l\mathbf{c}^*$ and $\mathbf{r}_j = x_j\mathbf{a} + y_j\mathbf{b} + z_j\mathbf{c}$, where x_j, y_j and z_j are the fractional coordinates of atom j, we get the crystallographic structure factor:

$$F_{hkl} = \sum_j f_j(\mathbf{Q}) \exp[2\pi i(hx_j + ky_j + lz_j)] \tag{1.14}$$

For some combinations of h, k and l, and for unit cells with atoms on high symmetry positions, the exponentials in the above equation can sum to zero, leading to some reflections being missing from the diffraction pattern. These necessarily missing peaks, known as systematic absences, help to determine the space group of the structure. For example, for a reflection to be observed from a face-centred cubic lattice, h, k and l must either all be even or all be odd. Any other combination results in a systematic absence.

The latter sum, over the entire crystal lattice, doesn't tell us anything on its own about the intensity of the diffraction pattern. Chiefly, it affects the shape

of the diffraction peaks. For a sample with an infinite number of unit cells in each direction, the diffraction peaks are a series of delta functions at the reciprocal lattice points. For finite numbers of unit cells, the diffraction peaks spread out over a small Q-range.

For both neutrons and X-rays, the effect of thermal motion must be taken into account. It was mentioned earlier that since X-rays scatter from a cloud of electrons of finite size, the atomic form factor decreases with increasing $\sin\theta/\lambda$. The effect of temperature is that the atoms vibrate about their average position, which has the effect of spreading the atom out and attenuating the diffraction signal. This is taken into account by the Debye-Waller factor, $\exp(-\langle[\mathbf{Q}\cdot\mathbf{u}]^2\rangle)$, where u is the displacement of the atom relative to its average position and the angular brackets indicate that a time average is taken. Using the definition of Q, this becomes $\exp(-8\pi^2\langle u^2\rangle\sin^2\theta/\lambda^2)$, where $\langle u^2\rangle$ is the root mean square of the atomic displacement. In some programs, a B-factor is used, with $B = 8\pi^2\langle u^2\rangle$. This form of the equation for the Debye-Waller factor assumes the displacement is isotropic. However, this is clearly not physically precise and, in many cases, such an assumption is invalid. In this context, atomic displacement parameters (ADPs) can be used. The atoms can then have different displacive amplitudes in different directions, although this is still subject to the symmetry restraints of the space group. In crystal structure diagrams, ADPs are usually represented using ellipsoids. The shape of the ellipsoids is determined by the relative magnitudes of thermal vibration of the atom along the axes of choice. The size of the ellipsoid is scaled to encapsulate a particular probability of finding the electron density of the scatterer within the ellipsoid. This probability is usually 50 %.

1.2.7   Total Scattering

To describe the total scattering method, we will start with the derivation for neutrons, since the neutron scattering length is a constant, unlike the Q-dependent atomic form factor of X-rays. This work follows the formalism for total scattering as laid out by Keen[16, 17]. As discussed previously, the scattering is determined by the structure factor:

$$F^N(\mathbf{Q}) = \sum_j b_j \exp[i(\mathbf{Q}\cdot\mathbf{r}_j)] \tag{1.15}$$

where the superscript N denotes that this is for neutron scattering. The quantity we actually detect in a diffraction experiment is related to the square of this quantity:

$$S^N(\mathbf{Q}) = \frac{1}{N}\left|F^N(\mathbf{Q})\right|^2 = \frac{1}{N}\sum_{jk} b_j b_k \exp[i\mathbf{Q}(\mathbf{r}_j - \mathbf{r}_k)] = \frac{1}{N}\frac{d\sigma}{d\Omega} \qquad (1.16)$$

where $S^N(\mathbf{Q})$ is the scattered intensity per unit atom for a system of N atoms at positions $\mathbf{r}_1$ to $\mathbf{r}_N$. The sum in the above equation can be split into two components: the self-scattering term, for which $j = k$, and the differential or interference scattering term, where $j \neq k$. We can then define a total-scattering structure factor without the self-scattering term. Typically, this is also referred to as $F(Q)$ in the literature, but for clarity will be referred to as $F_{TS}(Q)$ below. Since total scattering is performed on powder samples, the orientational averaging means we can use $|\mathbf{r}_j - \mathbf{r}_k| = r$ and $Q = |\mathbf{Q}|$ in the following equations. The total scattering structure factor can be expressed as follows[17]:

$$F_{TS}^N(Q) = \sum_{j,k=1}^{n} c_j c_k b_j b_k [A_{jk}(Q) - 1] \qquad (1.17)$$

where $A_{jk}(Q)$ are the Faber-Ziman (or site-site) partial structure factors[18] and c_j is the proportion of atom species j. This sum is over n atom species, rather than N total atoms. These partial structure factors are related to partial radial (or pair) distribution functions $g_{jk}(r)$ by the following relations:

$$A_{jk}(Q) - 1 = \rho_0 \int_0^\infty 4\pi r^2 [g_{jk}(r) - 1]\frac{\sin Qr}{Qr} dr \qquad (1.18)$$

and

$$g_{jk}(r) - 1 = \frac{1}{(2\pi)^3 \rho_0} \int_0^\infty 4\pi Q^2 [A_{jk}(Q) - 1]\frac{\sin Qr}{Qr} dQ \qquad (1.19)$$

where ρ_0 is the average number density of the material. The partial pair distribution functions are defined by the following equation

$$g_{jk}(r) = \frac{n_{jk}(r)}{4\pi r^2 dr \rho_k} \qquad (1.20)$$

where $n_{jk}(r)$ is the number of particles of atom species k between a distance r and $r + dr$ from a particle of atom species j and $\rho_k = c_k \rho_0$. We can also define a total

radial distribution function:

$$G^N(r) = \sum_{j,k=1}^{n} c_j c_k b_j b_k [g_{jk}(Q) - 1] \tag{1.21}$$

and then write the total pair distribution function and total scattering structure factor in terms of each other:

$$F_{TS}^N(Q) = \rho_0 \int_0^\infty 4\pi r^2 G(r) \frac{\sin Qr}{Qr} dr \tag{1.22}$$

and

$$G^N(r) = \frac{1}{(2\pi)^3 \rho_0} \int_0^\infty 4\pi Q^2 F_{TS}^N(Q) \frac{\sin Qr}{Qr} dQ \tag{1.23}$$

-*i.e.*, they are related to each other *via* a sine Fourier transform.

In the PDF analysis performed in this thesis, two different normalisations of the pair distribution function, $D(r)$ and $G'(r)$, are used with the programs TOPAS and PDFGui respectively. They have the same relation to the PDF defined above for both neutrons and X-rays

$$D(r) = 4\pi r \rho_0 G(r) = \left(\sum_{i=1}^{n} c_i b_i \right)^2 G'(r) \tag{1.24}$$

The formalism for X-ray total scattering is slightly more complicated since the atomic form factor is Q-dependent and would get convoluted with the partial structure factors when Fourier transforming between $F_{TS}^X(Q)$ and $G^X(r)$. Consequently, the atomic form factors are approximated by assuming that form factors for different atomic species vary similarly with Q but are scaled by the number of electrons in that atom, *i.e.*, $f_j(Q) = e_j f_e(Q)$ where e_j is the number of electrons for atom j, and $f_e(Q)$ is the average scattering factor per electron, given by $f_e(Q) = \sum_{j=1}^{n} c_j f_j(Q) / \sum_{j=1}^{n} c_j Z_j$ where Z_j is the atomic number of atom j. With this approximation, we can define the relation between the total and partial pair distribution functions:

$$G^X(r) = \sum_{j,k=1}^{n} c_j c_k \frac{e_j e_k}{\langle \sum_{i=1}^{n} c_i Z_i \rangle^2} [g_{jk}(r) - 1] \tag{1.25}$$

which can be Fourier transformed without any convolution, so this approximation is what we aim to get when converting X-ray total scattering data to real space.

In X-ray total scattering, since the X-ray scattering factors decrease in intensity at high Q, a sharpening factor is used. Using the definition of the total

scattering structure factor as the difference between the differential cross section per atom and the self-scattering term, the sharpening term $B(Q)$ is included:

$$F_{TS}^X(Q) = \left(\frac{1}{N}\frac{d\sigma}{d\Omega} - \sum_{j=1}^{n} c_j f_j(Q)^2 \right) / B(Q) \tag{1.26}$$

There are two forms for $B(Q)$ with different cases for using each of them[19]. Most frequently $B(Q) = \left(\sum_{j=1}^{n} c_j f_j(Q) \right)^2$ is used, but there are some systems where the use of this function still retains Q dependence to the total scattering structure factor, which can inhibit refinement programs from finding the best fit to the PDF. In systems which can be expected to show this behaviour, such as uncorrelated systems, this problem is alleviated by using $B(Q) = \sum_{j=1}^{n} c_j f_j(Q)^2$ as the sharpening function.

The Fourier transform between the total scattering structure factor and the pair distribution function involves an integral over Q from 0 to ∞. In real experiments however, an infinite Q cannot be reached and the integral is performed between a Q_{min} and Q_{max}, which are instrument dependent. The effects of integrating from Q_{min} can largely be ignored in crystalline materials since it would only effect very low frequency information. In contrast, truncating the upper end of the integral at a finite value introduces fluctuations into the data, known as termination ripples, since the Fourier transform of a box function is a sinc function, which gets convoluted with the PDF and must be accounted for in data analysis. This effect is more significant for lower values of Q_{max}. The value of Q_{max} also determines the resolution in real space, since $\Delta r = 2\pi/Q_{max}$, and a high Q_{max} is consequently desirable. Real diffraction data also has a finite reciprocal space peak width, dQ, which can supress the higher radius parts of the PDF. In addition, diffraction peaks typically are broader at higher Q, serving to broaden the PDF peaks. These last two parameters are typically refined using a standard.

When converting total scattering data into pair distribution functions, we want to minimise contributions from sources of scattering that aren't the sample since, as we can see from the definition of the partial pair distribution functions, PDF data is on an absolute scale. Therefore measurements of the sample environment and an empty beam must be taken and subtracted from the scattering data with the sample. The self-scattering must also be subtracted, but this can't be distinguised from the differential scattering and consequently introduces features into the low-r region of the PDF after conversion to real space. To account for this, as well as any other effects that may produce a Q-dependent background, the data is convolved

with a top hat function given by $T(Q) = 3/4\pi Q_T^3$ for $Q \leq Q_T$ and 0 otherwise. Typically, $Q_T = 3/r_{min}$ is used, where r_{min} is the minimum radius of the PDF, below which there are no physically plausible peaks present in the PDF. The convolved data is then subtracted before the Fourier transformation is performed. Other factors that need to be taken into account for converting X-ray total scattering data are the beam polarisation and Compton scattering factor, which can both reduce the atomic form factor. For both types of total scattering, the efficiency of sample packing in its container must also be considered. Typically, a 50 % packing fraction is assumed.

1.2.8   X-ray Sources

There are two primary ways to generate X-rays for use in diffraction experiments. The laboratory-based method uses a high voltage to accelerate electrons towards a target. The high energy of the electrons is then converted to radiation and heat upon striking this target. The emitted radiation consists of a continuous spectrum of X-rays. The spectrum of radiation emitted also contains spikes at energies characteristic of the elements which comprise the target. These energy spikes are what we use for diffraction experiments, and the target material is chosen for its particular characteristic energies. Commonly, light metals such as copper or molybdenum are used. The beam produced from such a source typically doesn't have a high enough Q_{max} to produce decent quality total scattering data, therefore these sources are not used in this thesis. Recently however there have been instruments manufactured that can perform total scattering in a laboratory environment, which is a key step in making the technique more accessible. These instruments require detectors with good counting statistics and the use of shorter wavelength, and therefore higher energy, X-rays from Ag sources.

Another method of producing X-rays is to use a synchrotron source. Synchrotron radiation is the radiation emitted from an accelerating charged particle travelling at near the speed of light. In synchrotron sources, electrons are made to constantly accelerate by steering them in a large circle using a magnetic field. The electrons are accelerated to a very high energy (3 GeV at Diamond Light Source, the UK's national synchrotron facility) and as a result of this, the magnetic fields need to be very strong and the radius of the main storage ring needs to be large. Diamond Light Source has a main storage ring with a circumference of 561.6 m inside a 738 m circumference building. Other synchrotrons are even larger. For example, the storage ring of PETRA III at DESY in Hamburg is 2.3 km in circumference. The X-rays produced tangentially from the orbiting electrons are guided to different

Wiggler
Beam splitter 17m
Diamond window 22m
Side beam absorbers
Diamond window 22m
White beam slits 23m
White beam slits 25m
OH1
Double crystal monochromator (DCM) 26m
Attenuator
Horizontally focussing bent Laue monochromator (BLM) 27m
Beam position monitor
Monochromatic slits 30m
Vertically focussing multi-layer mirror (MLM) 32m
Quadrant detector
Vertical Slit
Vertically focussing mirror (VFM) 30m
OH1-A
Horizontally focussing mirror (HFM) 35m
EH2
Slit 42m Intermediate source point for VFM
Intermediate source point for HFM Clean-up slits
Filter wheel
Fast shutter
Pinhole
Quadrant detector

Extreme conditions I15

XPDF (I15-1)

Slits
I₀
Slits
Clean-up
EH3 XPDF
Sample position 35m
Area detectors 0.2 – 1.0m from sample

EH1 I15
Small KB mirrors
Clean-up disc
6-circle diffractometer 48m
Second table 51m
CCD detector
Area detector

Figure 1.5: The layout of the I15-1 beamline at Diamond Light Source. Taken from [2]

beamlines vis an array of optics. An example of this, for the beamlines I15 and I15-1 at Diamond Light Source, is shown in Fig 1.5. Each beamline has a specialised set of optics equipment to best serve its main functions. The result of this is a source of X-rays that has a much higher energy and flux than laboratory sources, with many specialised techniques available. For diffraction experiments, this results in a higher Q_{max} and greater resolution and a much shorter collection time. In addition, the synchrotron radiation is horizontally polarised in the plane of the electron orbit. The former aspect allows total scattering measurements to be performed, whilst the latter allows more measurements to be done in a given window of time. The flux tends to be significantly higher for synchrotron X-ray sources than neutron sources, although to a much lesser degree than the increased flux compared to laboratory sources. For the work carried out in this thesis, the I15-1 beamline at Diamond Light Source and the P02.1 beamline at PETRA III have been used.

In total scattering experiments, the detector is quite close to the sample so as much of the total Q-range as possible can be measured without having to increase the size of the detector. For dedicated PDF beamlines, a 2D detector is used, with the centre of the beam either at one corner of the detector to maximise the Q-range for a given beam wavelength or at the centre, providing a higher count rate since the former set up only collects a portion of the diffraction rings. Dual-purpose
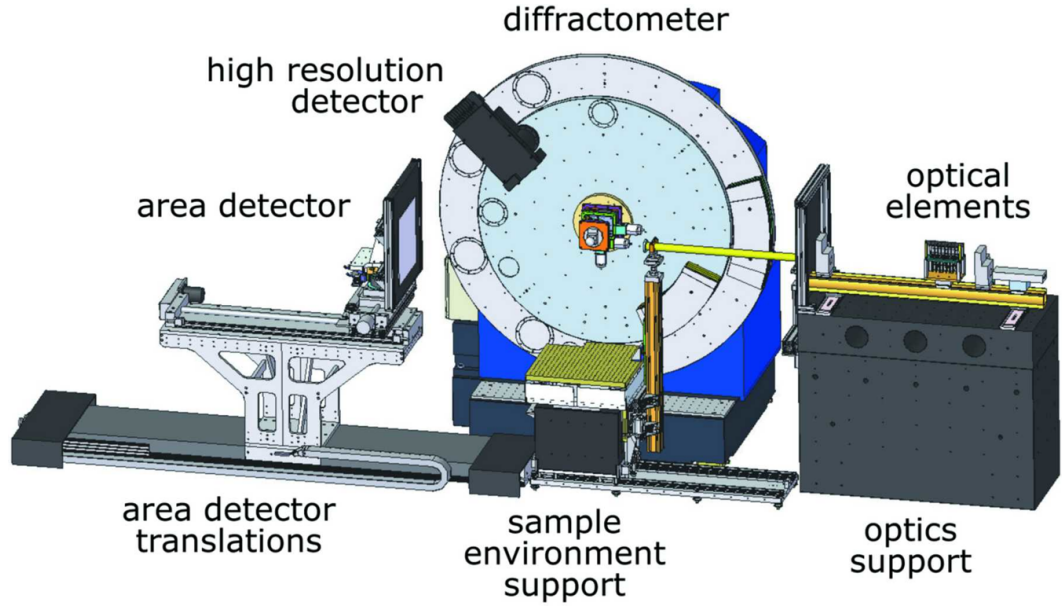
Figure 1.6: The standard experimental setup of the P02.1 beamline at PETRA III. The area detector is used to collect both total scattering and standard powder diffraction patterns, since it can be moved further from or closer to the sample. Diagram taken from [3]

beamlines, such as P02.1 at PETRA III, which need to collect both total scattering and powder diffraction data, can use a movable detector to switch between the two experiments (Fig 1.6) In addition, dedicated total scattering beamlines typically use shorter wavelength X-rays in order to access higher Q.

1.2.9 Neutron Sources

There are two methods to produce neutrons. The first employs the fission reaction of a nuclear reactor. In the fission reaction, a thermal neutron (5-10 meV) is absorbed by a ^{235}U nucleus which then becomes unstable. The unstable nucleus splits into a few lighter nuclei, releasing neutrons in the process (2.5 on average). Some of these emitted neutrons keep the chain reaction going, while the rest can be used for neutron diffraction. Neutron beams produced by a reactor source are usually monochromated.

The other method to produce neutrons is spallation. In this process, a high energy beam of protons, typically around 1 GeV, is shot into a heavy metal target such as mercury or tungsten. The impact causes many particles to spall off the target, including neutrons. The process produces between 20-30 neutrons per incident proton which are then channelled to the different instruments. The flux produced

by a spallation source is higher than a reactor source, but the signal is pulsed. Both reactor and neutron sources produce high energy neutrons which need to be slowed down for use in experiments. This is done by placing moderators formed of light elements, which can slow the neutrons down by inelastic scattering, around the source.

The neutron beam produced by a spallation source has a range of wavelengths and the instruments make use of this by taking advantage of the pulsed nature of the beam. The detector is placed at a fixed distance and angle from the sample and, since the de Broglie wavelength of the neutron is determined by its velocity, neutrons of different wavelengths will arrive at different times after the pulse. This is known as the time-of-flight method. After the neutrons are produced by the impact of the proton beam on the target, they are channelled to different instruments surrounding the target station.

Since spallation sources have a broad range of wavelengths compared to reactor sources, neutron diffraction patterns can be measured over a greater Q-range. The source can also be tailored further to give a greater Q-resolution, meaning that spallation sources such as ISIS in the UK are preferable for total scattering measurements. Instruments used for total scattering experiments typically have multiple detector banks at different angles, to capture as much of the diffracted beam as possible. For example, the two primary total scattering instruments at ISIS, GEM and POLARIS, have 8 and 5 detector banks, respectively.

1.2.10 Data Analysis

In modern crystallography, computer programs are used to determine a crystal structure from diffraction data. The following discussion of Bragg diffraction data will focus on X-ray powder diffraction data, since any neutron Bragg data that appears in this thesis has been refined by others, as stated in the declaration and analysis of single crystal data is beyond the scope of this work.

The main problem with analysing powder diffraction data is that the peaks from different hkls can overlap if they cause the beam to diffract at similar scattering angles. There are a few methods used to overcome this problem. To reduce the likelihood of this being an issue during data analysis, high resolution powder diffraction can be used. During data analysis, the Pawley [20] or Le Bail [21] methods can be used to determine the unit cell metric and trim down the number of potential space groups for the structure based on systematic absence analysis. These methods use some instrumental parameters and peak shape functions to determine the position of the Bragg peaks and then use a least-squares approach to refine the unit

cell parameters from an input guess. These methods don't determine the position of atoms within the unit cell, they just model the unit cell itself. The problem with these methods is that overlapping peaks from hkls that aren't symmetry equivalent can still be obscured. These methods are useful, however, since they can verify that a sample is single phase and accurately refine lattice parameters and peak shapes without a structural model.

The primary method for refining crystallographic models against powder diffraction data is the Rietveld method [22]. This method uses a structural model, consisting of lattice parameters, space-group symmetry and fractional coordinates, as an input to calculate a powder diffraction pattern. This model is then refined using a least-squares approach. The least-squares method minimises $\sum_i w_i(y_{i,o} - y_{i,c})^2$, where $y_{i,o}$ and $y_{i,c}$ are the observed and calculated intensities at some point, i, w_i is the weight given to that point and, typically, the weight $w_i = 1/\sigma^2(y_{i,o})$ is used, where $\sigma(y_{i,o})$ is the error in data point, $y_{i,o}$. In Rietveld refinement, the calculated intensities are convoluted with a peak shape function. This function is usually a pseudo-Voigt function, which is a combination of Gaussian and Lorentzian peak shapes. The quality of a fit is determined by its *weighted-profile R-factor* which is given by

$$R_{wp} = \sqrt{\sum_i w_i(y_{i,o} - y_{i,c})^2 / \sum_i w_i y_{i,o}^2} \qquad (1.27)$$

These methods require some instrument-dependent parameters to be determined by refinement of a standard sample, typically silicon. These include the wavelength or emission profile of the radiation, the peak shape parameters, the zero error of the instrument and an axial divergence parameter. A zero error will shift the scattering angle of the Bragg peaks, while an axial divergence to the beam can cause an asymmetric peak shape. In addition, a background, which arises from inelastic scattering of the diffracted X-rays as well as scattering from the air and sample environment, is modelled, usually with a polynomial function.

For refinements of crystallographic models using pair distribution function data, there are two commonly used methods. The first is similar to Rietveld refinement of Bragg peaks, where a unit cell is refined. In this technique however, it is not the structure factors that are calculated and refined, but the possible pairs within the structure. The quality of fit is still reported using the weighted R-factor as defined above. This type of technique is termed a "small box" technique, in contrast to the second common method of modelling PDF data. Small box analysis of PDF data is most commonly performed using the *PDFGui* [23] or *Topas Academic* software [24].

The other commonly used method of analysing PDF data is the Reverse Monte Carlo (RMC), or "big box", technique [25, 26] In this method, a large super-cell is built and atoms within it are allowed to move at random. If a move reduces some overall "energy" function, then the RMC algorithm accepts the move. There is also a small probability that the algorithm accepts a "bad" move. The "energy" used in RMC modelling includes a function similar to the R-factor for small box refinements, but constraints can also be included. For example, interatomic potentials can be used as a constraint to stop the atoms getting too close together. In addition, an R-factor for the Bragg data is also typically used, which ensures the resulting atomistic configurations obey the average structure.

Both small- and big-box methods have been used to try and evaluate lattice dynamics from PDF data. Small-box methods involve the pre-selection of a standard phonon model and the refinement of the PDFs associated with the model against experimental data. The process was found to be accurate for only simple models, and has a degree of user input bias[27, 28, 29]. Big-box methods of extracting dynamics from total scattering data involve using the reverse Monte Carlo method to generate a large number of atomistic configurations, all of which are consistent with the input. A phonon dispersion curve is then constructed from these, using methods developed for molecular dynamics[30, 31]. These methods have their limitations, which is the main motivation for the novel technique presented in this thesis.

The refinements of both Bragg and PDF data performed in this thesis use the Topas Academic software version 6.

1.3   Phonons and Symmetry

The classical view of temperature is the vibration of atoms about their equilibrium positions. These vibrations give rise to a number of important properties including thermal expansion, which will be discussed later, in section 1.4. Unlike in fluids or amorphous solids, we can get a good idea of the positions of atoms in crystals using diffraction techniques. If we can then determine the forces between atoms, we can gain an understanding of how the atoms oscillate within a crystal. The derivations for phonons in 1D crystals follow the typical arguments[32, 5, 33]. For the general case, I follow the arguments laid out by Dove[32]. We can also determine the atomic displacements associated with phonons from the space group of the crystal using representation theory. The arguments presented in section 1.3.4 follow the work of Stokes and Hatch[34]. A layman description of the terminology used in that section has been written by Senn[35].

1.3.1 Lattice Dynamics in one dimension
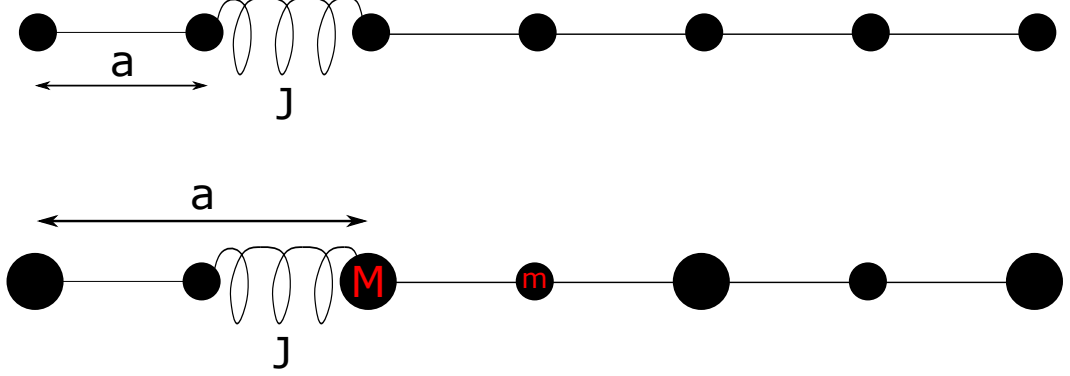
Figure 1.7: A diagram showing the one dimensional monoatomic (top) and diatomic chain (bottom) models, showing the repeat unit of length a in each case.

Imagine a chain of N atoms in one dimension, each separated by a distance a from its nearest neighbour in each direction with an energy, E, dependent only on a nearest neighbour interaction, $\phi(a)$ (Fig 1.7). At rest, the energy of this chain will be given by $E = N\phi(a)$. If each atom is displaced by some distance u_n, $n \in [1, N]$ from its equilibrium position, the total energy of the chain will be increased, since the unperturbed chain is the local ground state. We can calculate the increase in energy using a Taylor series:

$$\Delta E = \sum_{\alpha=1}^{\infty} \frac{1}{\alpha!} \frac{\partial^{\alpha}\phi}{\partial u^{\alpha}} \sum_{n=1}^{N} (u_n - u_{n+1})^{\alpha} \tag{1.28}$$

The nearest neighbour separation, a, represents a minimum in the energy since it is the equilibrium separation and, therefore, the first derivative in the above equation will be zero. We also ignore terms for $\alpha > 2$, which results in the energy being equivalent to a series of harmonic oscillators. This is known as the harmonic approximation. The main reason for doing it is that anharmonic equations do not have exact solutions, so simplifying it to only the harmonic contribution allows exact solutions to be calculated. This is justified in a physical sense since the displacements caused by lattice vibrations are, in general, small when compared to the distances between atoms, so higher order terms will have a vanishingly small contribution. Analogously to the simple harmonic oscillator, we can define an effective "spring constant", J, between the atoms with $J = \partial^2\phi/\partial u^2$ and $\Delta E = (J/2)\sum_{n=1}^{N}(u_n - u_{n+1})^2$. Using Newton's second law, we can write an equation of motion for the nth

atom:

$$m\frac{\partial^2 u_n}{\partial t^2} = -\frac{\partial E}{\partial x} = -\frac{\partial(\Delta E)}{\partial u_n} = -J(2u_n - u_{n+1} - u_{n-1}) \tag{1.29}$$

using periodic boundary conditions for $n = 1$ and $n = N$, $i.e.$, for $n = N$, $n+1 = 1$. The solution for a harmonic oscillator is a plane wave so we assume a solution corresponding to a superposition of plane waves:

$$u_n(t) = \sum_k A_k \exp[i(kx - \omega_k t)] \tag{1.30}$$

where $x = na$, k is a wave vector and A_k and ω_k are the amplitude and angular frequency of the wave with wave vector, k, respectively. We substitute this into the equation of motion, which results in:

$$m\omega_k^2 = 2J(1 - \cos ka) \tag{1.31}$$

This can be rearranged using trigonemtric identities to give a solution for ω_k in terms of k, known as the dispersion relation:

$$\omega_k = 2\sqrt{\frac{J}{m}}|\sin(ka/2)| \tag{1.32}$$

where we are taking positive roots only, hence the absolute value of $\sin(ka/2)$ appearing in the above equation. This equation (1.32) is periodic with a repeat unit of $2\pi/a$, $i.e.$, if we add a reciprocal lattice vector, $a^* = 2\pi/a$, to k, we retain the same frequency and hence all the information is given by waves with $|k| \leq \pi/a$. The edges of this region, $k = \pm\pi/a$, define the boundary of the first Brillouin zone (BZ). The Brillouin zone can be thought of as a reciprocal space unit cell[3] and points within it are usually described in terms of a reduced wave vector, obtained by dividing the wave vector by the reciprocal lattice vector. For example, in the above example, the boundaries of the BZ are given by reduced wave vectors $k^* = \pm 1/2$. The BZ is also symmetry dependent, and high-symmetry points of it are given labels, depending on the symmetry of the lattice. For all symmetries, the BZ centre, [0 0 0], is labelled Γ, and, for a primitive cubic lattice, the high symmetry points [1/2 0 0], [1/2 1/2 0] and [1/2 1/2 1/2] are labelled X, M and R respectively. The face-centred and body-centred cubic BZs will be different, since some reciprocal lattice points will be missing due to systematic absences. These systematic abscences can increase the

---

[3]In reality, the Brillouin Zone is a Wigner-Seitz cell of the reciprocal lattice. A Wigner-Seitz cell is the volume around a lattice point that encompasses all points in space closer to that lattice point than any other.
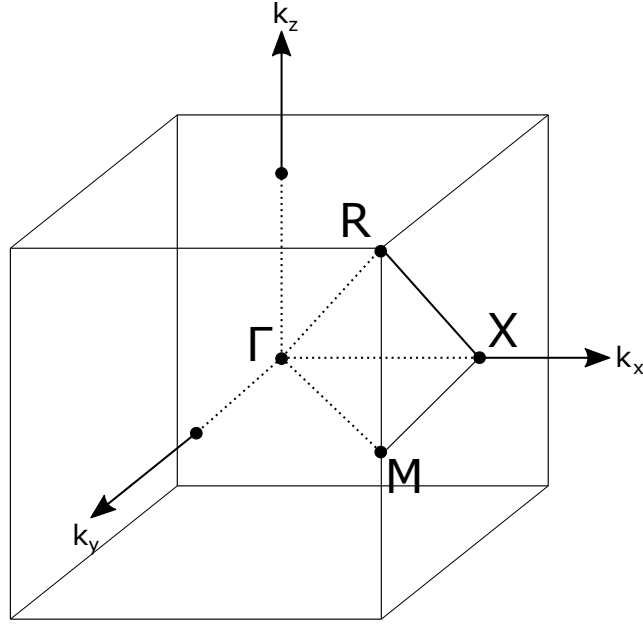
Figure 1.8: A diagram showing the high symmetry points of the primitive cubic Brillouin Zone.

size of the BZ in certain directions.

The number of possible wave vectors within one BZ is finite since we have a finite chain of atoms. The number can be determined using the periodic boundary conditions since atom N must behave in the same way as atom 0 and using the equation for $u_n(t = 0)$, we have $\exp(ikNa) = \exp(0) = 1$, giving

$$k = \frac{2\pi m}{Na} \tag{1.33}$$

where m is an integer.

In the dispersion relation for this simple system, if we consider the angular frequency, ω, in the long wavelength limit ($k \to 0$), the dispersion will approximately be linear:

$$\omega(k \to 0) = a\sqrt{J/m}|k| \tag{1.34}$$

giving a constant phase velocity, meaning long wavelength waves with different wavelengths can travel through a solid without breaking up. This is the reason that low frequency noises can travel through solids without distortion. The phase velocity of these modes give the speed of sound in the solid. Due to this connection with sound waves, these modes are termed acoustic modes. They are the only type of mode for the simple case of a chain of identical atoms, but more complex systems

have another type of mode.

Now, consider a chain of atoms alternating between two different types, one of mass m and another of mass M, as shown in Fig 1.7. Atoms of the same type are separated by a distance, a, and the atoms are equally spaced when at rest. As before, there is a force constant, J, between neighbouring atoms. For this case, we get a more complicated dispersion relation:

$$\omega_k^2 = J\left(\frac{1}{M} + \frac{1}{m}\right) \pm J\sqrt{\left(\frac{1}{M} + \frac{1}{m}\right)^2 - \frac{4\sin^2(ka/2)}{Mm}} \tag{1.35}$$

which has two solutions (or branches). These solutions are plotted in Fig 1.9. The first has the same behaviour as the acoustic modes, as described previously, while the second solution is non-zero at the zone centre and varies weakly with k. This branch is termed the optic mode.

In the three-dimensional picture, displacements can either be along the chain or perpendicular to it. Using this we can classify the modes further, as they can be either longitudinal or transverse and optic or acoustic. When this model of a diatomic chain is expanded to systems with n atoms in a unit cell, there will always be 3 acoustic branches, 2 of which will be transverse, and $3(n$-$1)$ optic branches.

1.3.2   General Description of Lattice Dynamics

It gets increasingly difficult to solve specific cases when the picture gets more complex than the one-dimensional diatomic chain. Therefore, we will continue by discussing how the phonon frequencies are calculated in a general case. Similarly to the simple case, we can use Newton's laws to determine an equation of motion and, therefore, we will need to define a lattice energy :

$$E = \frac{Z}{2} \sum_{\kappa,\kappa'} \phi\begin{pmatrix} \kappa \\ \kappa' \end{pmatrix} \tag{1.36}$$

where ϕ is the interaction energy between atoms κ and κ' in the unit cell and Z is the number of unit cells. As before, we determine the change in energy due to displacements of these atoms, although these are now vector quantities:

$$\mathbf{u}_{\kappa,\alpha} = \begin{pmatrix} u_{\kappa,x} \\ u_{\kappa,y} \\ u_{\kappa,z} \end{pmatrix} \tag{1.37}$$
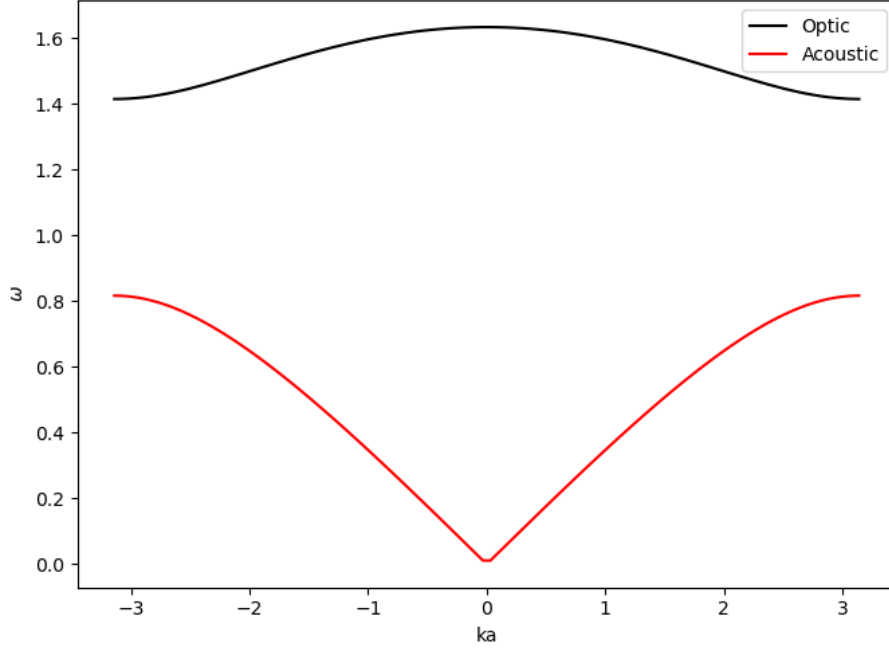
Figure 1.9: A plot of the frequencies of the diatomic chain model. For this solution, a coupling constant of $J = 1$ and atomic masses $M = 3$ and $m = 1$ were used.

The energy per unit cell is given by a Taylor expansion:

$$E = E_0 + \sum_{\kappa,\alpha} \frac{\partial E}{\partial \mathbf{u}_{\kappa,\alpha}} \cdot \mathbf{u}_{\kappa,\alpha} + \frac{1}{2} \sum_{\kappa,\alpha,\kappa',\alpha'} \mathbf{u}_{\kappa,\alpha} \cdot \frac{\partial^2 E}{\partial \mathbf{u}_{\kappa,\alpha} \partial \mathbf{u}_{\kappa',\alpha'}} \cdot \mathbf{u}_{\kappa',\alpha'} + O(\mathbf{u}_{\kappa,\alpha}^3) + ... \quad (1.38)$$

The first order term, $\sum_{\kappa,\alpha} \frac{\partial E}{\partial \mathbf{u}_{\kappa,\alpha}} \cdot \mathbf{u}_{\kappa,\alpha}$ is just the force on atom κ, which at equilibrium is zero so we can ignore it, as in the one-dimensional case. We also use the harmonic approximation, leaving us only the 2nd order term. This term can be simplified by defining a force constant matrix:

$$\Phi_{\alpha,\alpha'}^{\kappa,\kappa'} = \frac{\partial^2 E}{\partial \mathbf{u}_{\kappa,\alpha} \partial \mathbf{u}_{\kappa',\alpha'}} \quad (1.39)$$

This force constant matrix encapsulates the symmetry of the system, since if there are two or more symmetry equivalent directions then the force an atom feels from those directions will be equal. For example, consider the structure of rock salt, NaCl. Each Na atom has a neighbouring Cl atom at some distance a either side of it in both directions in each cartesian direction, with an equal magnitude force

27

coming from each Cl atom.

Using this force constant matrix, the equation of motion will be:

$$m_\kappa \frac{\partial^2 \mathbf{u}_{\kappa,\alpha}}{\partial t^2} = -\sum_{\kappa',\alpha'} \Phi_{\alpha,\alpha'}^{\kappa,\kappa'} \cdot \mathbf{u}_{\kappa',\alpha'} \qquad (1.40)$$

into which we can substitute a plane wave solution:

$$\mathbf{u}_{\kappa,\alpha} = \sum_{\mathbf{k},\nu} \mathbf{U}_{\nu,\kappa,\alpha,\mathbf{k}} \exp[i(\mathbf{k} \cdot \mathbf{r}_{\kappa,\alpha} - \omega(\mathbf{k},\nu)t)] \qquad (1.41)$$

This yields an eigenvalue equation for the frequencies:

$$\omega^2(\mathbf{k},\nu)\epsilon(\mathbf{k},\nu) = \mathbf{D}(\mathbf{k})\epsilon(\mathbf{k},\nu) \qquad (1.42)$$

where the polarisation vectors ϵ, which describe the direction of displacement of each atom for each mode, ν, are $3n$ dimensional (n being the number of atoms per unit cell) and given by:

$$\epsilon(\mathbf{k},\nu) = \begin{pmatrix} \sqrt{m_1}U_x(1,\mathbf{k},\nu) \\ \sqrt{m_1}U_y(1,\mathbf{k},\nu) \\ \sqrt{m_1}U_z(1,\mathbf{k},\nu) \\ \vdots \\ \sqrt{m_n}U_x(n,\mathbf{k},\nu) \\ \sqrt{m_n}U_y(n,\mathbf{k},\nu) \\ \sqrt{m_n}U_z(n,\mathbf{k},\nu) \end{pmatrix} \qquad (1.43)$$

and $\mathbf{D}(\mathbf{k})$ is a $3n \times 3n$ matrix called the Dynamical matrix. The dynamical matrix is obtained by a Fourier transform of the force constant matrix and hence will also be dependent on the symmetry of the lattice:

$$D_{\alpha,\alpha'}^{\kappa,\kappa'} = \frac{1}{\sqrt{m_\kappa m_{\kappa'}}} \sum_\alpha \Phi_{\alpha,\alpha'}^{\kappa,\kappa'} \exp[-i(\mathbf{k} \cdot \mathbf{r}_\alpha)] \qquad (1.44)$$

The basic principle behind *ab initio* methods to calculate phonon frequencies and eigenvectors is to determine the force constant matrix by calculating the change in forces when atoms in an input structure are physically displaced.

1.3.3 Anharmonic Effects

In the previous treatment of lattice dynamics, terms of a higher order than the second differential of energy were ignored. This is a useful approximation since it allows us to find exact solutions for the phonon frequencies, but the harmonic approximation fails to account for a number of important properties. One of them is thermal expansion, which will be discussed in more detail in the next section. In the harmonic approximation, each phonon acts independently but in the full anharmonic Hamiltonian, phonons can interact with each other. Due to the small displacements involved with lattice dynamics, typically only quartic terms are considered.

An important aspect of the field of crystallography that requires anharmonic effects are phase transitions. If we take a snapshot at some point along the propagation vector of a phonon, the displacements it causes will temporarily break some of the symmetry elements of the space group, whilst, on the time average, the crystal still obeys them. If at some point it becomes preferable in energy for these displacements to be permanently frozen in to the structure, then the symmetry elements that are broken by the phonon mode remain broken, and the structure will be described by a new, lower symmetry space group. Typically, the higher symmetry structure is referred to as the "parent" space group, whilst the structure it becomes after a phase transition is the "child". This is the basic idea of the "soft mode" theory of phase transitions, *i.e.*, a displacement of atoms along a phonon eigenvector of a material in a metastable state can cause a transition to a lower energy polymorph. If a phase of a material is unstable with respect to certain phonon eigenvectors, then the eigenvalues of those eigenvectors of the dynamical matrix will be negative when calculated for that phase, meaning that they are associated with phonons of imaginary frequency. A material which is stable has to become unstable somehow, which is where anharmonic effects come in. Consider a system with a Hamiltonian of the form:

$$H = \frac{1}{1}mv^2 + \frac{1}{2}k|x|^r \tag{1.45}$$

where m is the mass of the oscillator, k is the effective spring constant, v is the velocity and x is the displacement of the oscillating atom. The frequency of this oscillation is proportional to $x_{max}^{r/2-1}$, where x_{max} is the amplitude of the oscillation. For values of $r > 2$, *i.e*, anharmonic oscillations, the frequency is dependent on the amplitude of vibration[36]. Since the amplitude in turn is dependent on temperature, this means the frequencies are also temperature dependent. While the temperature variance of phonon frequencies occurs due to anharmonic effects, it is usually modelled with a pseudo-harmonic approximation. The frequencies are

renormalised from their harmonic values. When considering only harmonic and quartic terms, and in the simplest case where the phonon coupling constants are temperature independent, the renormalised frequencies, ω^2, are linearly dependent on temperature:

$$\omega^2(\mathbf{k}, j) = \omega_0^2(\mathbf{k}, j) + \frac{1}{2}k_B T \sum_{\mathbf{k}', j'} \frac{\alpha_4(\mathbf{k}, \mathbf{k}', j, j')}{\omega_0^2(\mathbf{k}', j')} \tag{1.46}$$

where ω_0^2 are the harmonic phonon frequencies and α_4 are the 4th order anharmonic coupling parameters[32, 37]. If the square of the phonon frequency is temperature dependent, then lowering the temperature could lower ω^2 below zero at some critical temperature, at which point the phase transition occurs.

Modes which are low frequency and hence likely to cause transitions are called soft modes. Often, the wave vector of a soft mode is a high-symmetry point, meaning it lies at the centre or on the boundary of the BZ. While the temperature variance of phonon frequencies occurs due to anharmonic effects, it is usually modelled with a pseudo-harmonic approximation.

Landau theory is often used to describe phase transitions, particularly continuous phase transitions. In Landau theory, the Helmholtz free energy is written as a functional of some parameter of interest, dubbed the order parameter. For example, the free energy of a ferromagnetic material can be written as a function of the magnetisation, m:

$$F(T, m) \approx F_0 + a_0(T - T_c)m + \frac{b_0}{2}m^4 \tag{1.47}$$

where F_0 is some ground state free energy, T_c is the critical temperature of the ferromagnetic transition and a_0 and b_0 are constants. The ground state of a system at any given temperature is the minimum of the free energy and the minimum of equation 1.47 with respect to the magnetisation is at $m = 0$ for $T > T_c$ and when $m_0^2 = -(a_0/b_0)(T - T_c)$ for $T < T_c$, meaning that below the critical temperature, the material has a permanent magnetisation of $\pm m_0$. The amplitude of a soft mode can be used as an order parameter for a phase transition in Landau theory. When discussing phonon modes in the language of group theory, the idea of an order parameter becomes more complex due to multi-dimensional irreducible representations. The Landau potential is written as a linear combination of sets of polynomials in the components of the order parameter. These polynomials must be invariant under all of the symmetry operations of the parent space group[38, 39].

In this thesis, order parameters will be classified according to the irreducible

representations that they transform as, and the irreducible representation label will be used interchangeably to refer directly to the order parameter.

1.3.4 Representation Theory

The collection of symmetry operations that act on a crystal, together with the operation of combining these symmetry elements, form a mathematical construct known as a group, hence the term space group in crystallography. A group, G, has a set of conditions which it must satisfy:

(a) If $a, b \in G$, then $c = a \circ b$ is also a member of G

(b) If $a, b, c \in G$, then $a \circ (b \circ c) = (a \circ b) \circ c$

(c) There is an identity element $E \in G$ that satisfies the condition $E \circ a = a \circ E = a$ for all $a \in G$

(d) For each $a \in G$, there is an inverse element a^{-1} that satisfies the condition $a \circ a^{-1} = a^{-1} \circ a = E$

This means that any combination of two symmetry elements is another symmetry element of the space group, and that the action of each symmetry element can be "undone" by another. If we form a vector space[4] to describe the positions of atoms in a unit cell, we can represent the action of the symmetry elements on the vectors in the vector space as matrices. This is the core idea of representation theory - we can convert a problem in group theory to one in linear algebra. The matrix that describes the action of a symmetry element is the *representation* of that symmetry element. The different representations must still obey the conditions that make them elements of a group. We can also consider the action of these matrices upon a *distortion space*: a vector space consisting of the atomic displacements of the atoms in a crystal. For an example of this, consider an arrangement of atoms in the $x - y$ plane, with positions $\mathbf{r}_1 = (a, 0)$, $\mathbf{r}_2 = (-a, 0)$, $\mathbf{r}_3 = (0, b)$ and $\mathbf{r}_4 = (0, -b)$ (Fig 1.10). We can define a point group ($2mm$) of symmetry elements which these objects obey consisting of:

(a) E, the identity operator

(b) C_{2z}, a rotation of 180° about the z-axis

---

[4]A vector space is a set of vectors over some field, usually a multi-dimensional real space in this section. Similarly to a group, there are a list of axioms the vectors must obey to be described as a vector space.

(c) m_x, a mirror plane along the x-axis

(d) m_y, a mirror plane along the y-axis

which obey the rules for a group since all four elements are their own inverse. If we define a vector which consists of the atomic displacements in the x and y plane

$$\mathbf{u} = (u_{1x}, u_{1y}, u_{2x}, u_{2y}, u_{3x}, u_{3y}, u_{4x}, u_{4y}) \tag{1.48}$$

we can then define matrix representations for the symmetry operations, since we know the result of applying the operations to the above vector. For example, if we apply the mirror in the x-axis to the general vector of displacements, we get the following:

$$m_x(\mathbf{u}) = (u_{1x}, u_{1y}, u_{2x}, u_{2y}, u_{4x}, -u_{4y}, u_{3x}, -u_{3y}) \tag{1.49}$$

meaning we can use the following representation:

$$m_x \rightarrow \begin{pmatrix} 1 & 0 & 0 & 0 & 0 & 0 & 0 & 0 \\ 0 & 1 & 0 & 0 & 0 & 0 & 0 & 0 \\ 0 & 0 & 1 & 0 & 0 & 0 & 0 & 0 \\ 0 & 0 & 0 & 1 & 0 & 0 & 0 & 0 \\ 0 & 0 & 0 & 0 & 0 & 0 & 1 & 0 \\ 0 & 0 & 0 & 0 & 0 & 0 & 0 & -1 \\ 0 & 0 & 0 & 0 & 1 & 0 & 0 & 0 \\ 0 & 0 & 0 & 0 & 0 & -1 & 0 & 0 \end{pmatrix} \tag{1.50}$$

If the matrix representation of a space group element can be converted by a similarity transformation[5] to a block diagonal matrix[6] then that representation is said to be reducible[7]. If the set of matrices forming the diagonal blocks cannot be reduced in any way, then the set of block matrices forms an irreducible representation. This effectively constitutes a change of basis[8] for the vector space, to a new set of basis

---

[5] Two matrices A and A' are similar if $A'B = BA$ for some invertible matrix B. The similarity transform from A to A' is then given by $BAB^{-1} = A'$, where B^{-1} is the inverse of B. Diagonalisation is a form of similarity transform.

[6] A block diagonal matrix is a type of square matrix, the diagonal elements of which are smaller square matrices and off-diagonal elements of which are zero.

[7] For a representation to be reducible, all the matrices that constitute the representation must be able to be converted to a block diagonal form. If this is not possible, then the irrep is multi-dimensional, meaning that the displacements associated with the irrep are not independent with respect to at least one of the symmetry elements of the space group.

[8] A basis for a vector space is a set of vectors that span the vector space, by which we mean every component of the vector space can be expressed as a sum of scalar products, or linear combination, of the basis vectors. In addition, the basis vectors must be linearly independent of each other. The dimension of a vector space is the number of basis vectors.
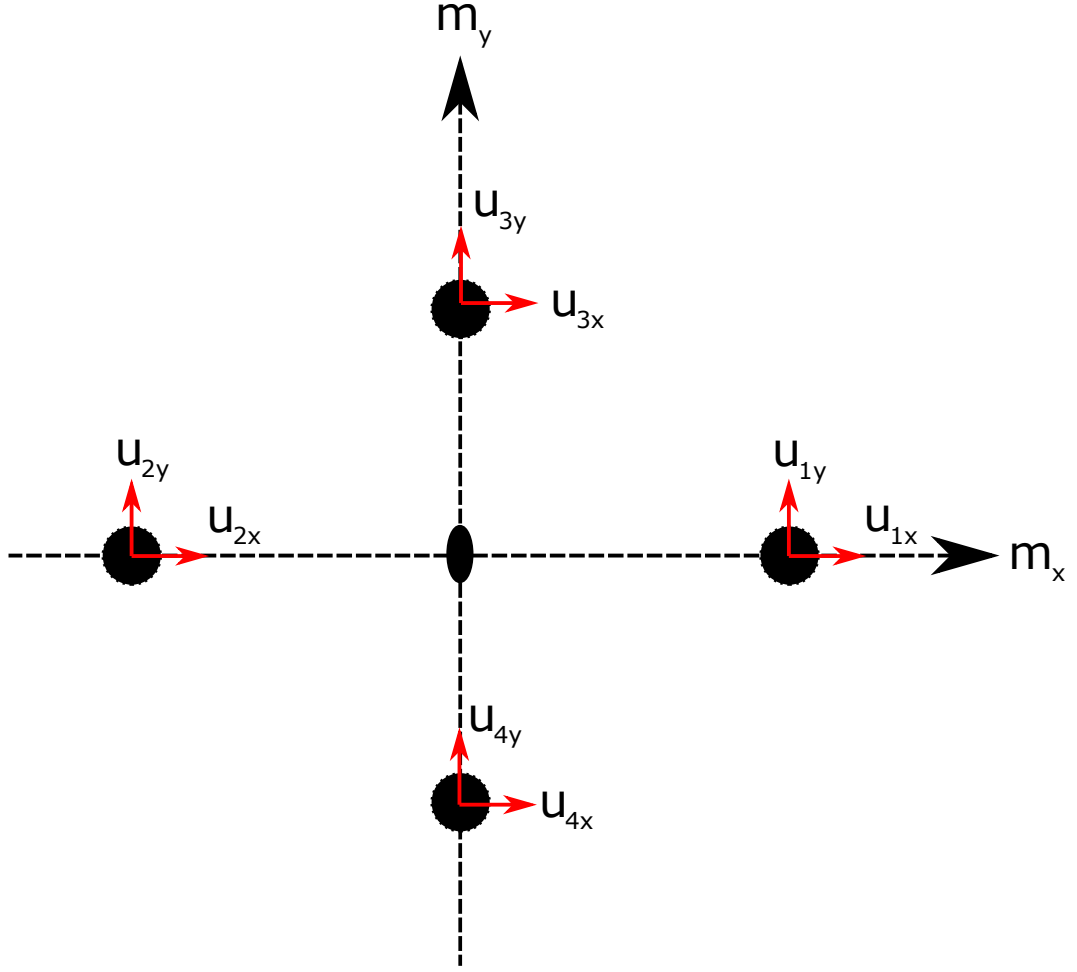
Figure 1.10: A diagram showing the arrangement of atoms used for examples in this section.

vectors that are collective displacements of the atoms, rather than displacements of one atom in one direction.

To demonstrate this generally, consider a particular vector $\mathbf{u}$ in the vector space of atomic displacements, S. We can form an n-dimensional subspace of S, S', by operating on $\mathbf{u}$ by every symmetry element g of the space group G. Using the previous example, the vector $\mathbf{u} = (u, 0, 0, 0, u, 0, 0, 0)$ produces the vectors $m_x(\mathbf{u}) = (0, 0, -u, 0, u, 0, 0, 0)$, $m_y(\mathbf{u}) = (u, 0, 0, 0, 0, 0, u, 0)$ and $C_{2z}(\mathbf{u}) = (0, 0, -u, 0, 0, -u, 0)$. The set of vectors $\{g\mathbf{u}\}$ span S', $i.e.$, all linear combinations of these vectors are also members of S'. If we define a basis of S', then the action of a symmetry operation, g, on one of these basis vectors can be expressed as a

linear combination of the basis vectors. The coefficients of this linear combination form an n-dimensional square matrix, with a different matrix for each symmetry element. These matrices relate to each other in the same way as the symmetry elements do, therefore they form a representation of G. For example, the subspace generated by $\mathbf{u} = (u, 0, 0, 0, u, 0, 0, 0)$ has basis vectors $u_1 = (1, 0, 0, 0, 0, 0, 0, 0)$, $u_2 = (0, 0, 1, 0, 0, 0, 0, 0)$, $u_3 = (0, 0, 0, 0, 1, 0, 0, 0)$ and $u_4 = (0, 0, 0, 0, 0, 0, 1, 0)$. This subspace contains all displacements in the x-direction. A general vector in this subspace is $\phi = au_1 + bu_2 + cu_3 + du_4$, which we can write as $\phi = (a, b, c, d)$. By considering the action of the symmetry elements on the basis vectors, we can build a representation in this subspace:

$$D(m_x) = \begin{pmatrix} 0 & -1 & 0 & 0 \\ -1 & 0 & 0 & 0 \\ 0 & 0 & 1 & 0 \\ 0 & 0 & 0 & 1 \end{pmatrix} \qquad D(m_y) = \begin{pmatrix} 1 & 0 & 0 & 0 \\ 0 & 1 & 0 & 0 \\ 0 & 0 & 0 & -1 \\ 0 & 0 & -1 & 0 \end{pmatrix} \qquad (1.51)$$

$$D(C_{2z}) = \begin{pmatrix} 0 & -1 & 0 & 0 \\ -1 & 0 & 0 & 0 \\ 0 & 0 & 0 & -1 \\ 0 & 0 & -1 & 0 \end{pmatrix} \qquad D(E) = \begin{pmatrix} 1 & 0 & 0 & 0 \\ 0 & 1 & 0 & 0 \\ 0 & 0 & 1 & 0 \\ 0 & 0 & 0 & 1 \end{pmatrix} \qquad (1.52)$$

These representations are all equal to their own inverse and follow the multiplication rules for the point group.

If we do the same process for a new vector $\mathbf{u}'$, orthogonal to every vector in S', we form a new subspace S'', which has no overlap with S'. All the vectors in each subspace are orthogonal to each other, including the basis vectors. We can repeat this process until the original vector space is fully decomposed. The sum of the dimension of these subspaces is the same as the dimension of the parent space, and each subspace has basis vectors that are orthogonal to the basis vectors of all the other subspaces. Therefore, the basis sets of each representation forms a basis set of the distortion space, S. For example, we can construct a subspace, orthogonal to the previous example, containing all the displacements in the y-direction. The two subspaces have no overlap, since x-displacements can not be transformed into y-displacements under the symmetry operations of the $2mm$ point group, and *vice-versa*. The new subspace will have 4 basis vectors, orthogonal to those of the x-subspace and has a dimension of 4. Adding this to the dimension of the previous subspace (also 4) gives the dimension of the parent space.

If, for some vector **u** and subspace S', we can find another vector **u**$'$ in S' such that the set of vectors $\{g\mathbf{u}'\}$ span a subspace with a dimension smaller than that of S', then the matrix representation of S' is reducible. We can repeat this process until we have a set of matrices which form an irreducible representation. As before, the basis vectors corresponding to the irreps of the fully decomposed vector space, S, form a basis set for S. Consider again the arrangement of atoms in the $x - y$ plane, with positions $\mathbf{r}_1 = (a, 0)$, $\mathbf{r}_2 = (-a, 0)$, $\mathbf{r}_3 = (0, b)$ and $\mathbf{r}_4 = (0, -b)$ and with point group $2mm$. We can choose a vector $\mathbf{u} = (u, 0, -u, 0, 0, 0, 0, 0)$ which is invariant under the elements of $2mm$ and forms a subspace on its own with irreducible representation matrices, $D(m_y) = D(m_x) = D(C_{2z}) = 1$. The vectors $\mathbf{u}' = (0, u, 0, u, 0, 0, 0, 0)$ and $\mathbf{u}'' = -\mathbf{u}'$ form a subspace since they are both invariant under the mirror planes but $D(C_{2z})\mathbf{u}' = \mathbf{u}''$ and *vice versa*. The subspace is one-dimensional, however, since both vectors can be described using a single basis vector. This brings up a key aspect of the basis vectors: if two basis vectors can be transformed onto each other using symmetry elements of the parent space group, then they transform as the same irrep.

In the above examples of irreducible subspaces, the irreducible representation matrices are one dimensional. There are, however, cases where representations cannot be reduced to a single dimension. Multi-dimensional irreps mean that the orthogonal displacement vectors associated with them are physically indistinguishable from each other once the symmetry elements of the parent space group have been applied[40]. For example, the representations in equation 1.51 can be broken down into two-dimensional block diagonal matrices, meaning that the x-displacements of the atoms at positions $\mathbf{r}_1$ and $\mathbf{r}_2$ are not independent. The same is also true of the x-displacements of the atoms at positions $\mathbf{r}_3$ and $\mathbf{r}_4$.

From this discussion of irreducible representations and atomic displacements we can see that they are important when discussing lattice dynamics. The reason we use them is that the eigenvectors of the dynamical matrix correspond to the modes associated with the irreducible representations, so we can determine phonon eigenvectors for high symmetry systems at high symmetry BZ points based only on the structure of a material, without needing to consider the forces between the constituent atoms. This is the basis of the method outlined in chapter 2: we can analyse the local structure of a material by determining how it deviates from the average along basis vectors associated with the irreducible representations of the parent space group. Another useful property of irreducible representations is that the number of them is dependent on the number of conjugacy classes[41][9] in the

---

[9] A conjugacy class of a symmetry element g_k in a space group G consists of the symmetry

space group, so different structures with the same space group symmetry will have the same set of irreps but different distortions associated with them. If two different structures are related, then the distortions associated with each irrep will also be related, provided a consistent setting is used for the structures. For example, the materials isostructural to ReO_3 can be thought of as A-site deficient perovskites and when I perform the mode parameterisation of these materials and compare it to that of a normal perovskite, the modes associated with an irrep in ReO_3 are a subset of the modes associated with the same irrep of the ABX_3 perovskite.

As discussed in a previous part of this section, collective distortions of atoms in a crystal are associated with symmetry-breaking phase transitions. If the distortion described by a vector, $\mathbf{u}$, gets frozen in to the structure, the new space group, G', is a subgroup of the parent space group, G, so it still obeys the definition of a group but with a smaller set of symmetry elements. The new space group will contain the symmetry elements that leave $\mathbf{u}$ invariant, $i.e.$, $g\mathbf{u} = \mathbf{u}$. This means that for elements that are in G but not G', the relation $g\mathbf{u} = \mathbf{u}$ no longer holds. Now let us suppose that $\mathbf{u}$ can be written as a linear combination of basis vectors u_1, u_2 and u_3 of a 3-dimensional irreducible subspace, $i.e.$, $\mathbf{u} = \sum_{i=1}^{3} c_i u_i$. In this subspace, each symmetry element g has an irreducible matrix representation $D(g)$, so we can write the action of a symmetry element on $\mathbf{u}$ as

$$g\mathbf{u} = \sum_{j=1}^{3} \left(\sum_{i=1}^{3} D_{ji}(g) c_i \right) u_j \tag{1.53}$$

From this equation, it can be seen that the relation $g\mathbf{u} = \mathbf{u}$ holds if the relation $g\mathbf{c} = D(g)\mathbf{c}$ is true, where $\mathbf{c}$ is a vector containing the coefficients c_i. Therefore, the vector of coefficients determines which symmetry elements are broken. Since the amplitude of a distortion can be used in Landau theory as an order parameter, the vector of coefficients is termed an order parameter direction.

When applying representation theory, tools such as ISODISTORT[42] are used since they automate a rather complex procedure. ISODISTORT takes an input structure file and uses the known irreps of the space group to generate a full set of basis vectors for the distortion space classified by their associated irrep and a matrix to change from the generated distortion mode basis to a simple cartesian basis. This matrix allows us to implement this basis in refinement programs such as TOPAS since we can determine how varying the amplitude of a particular distortion

---

elements $g_j = g_n^{-1} g_k g_n$, with g_n running through G.

mode changes the positions of the atoms in the unit cell.

The work presented in this thesis uses the Miller and Love notation for the irreducible representations[43]. In this notation, the irrep label takes the form $A_n^{\pm}$, where A denotes the propagation vector of the distortion using its BZ label, the subscript n is a number that differentiates the irrep from others at the same point in the BZ and the superscript indicates whether the distortion breaks or conserves inversion symmetry at the origin (represented by - and + respectively). The irrep labels can change for different unit cell settings and the setting used for a given case is stated. In addition to specifying the irrep we are considering, we often need to specify the relationship between different components of a multi-dimensional irrep and the different arms of a wave vector. The possible arms of the wave vector are determined by the space group symmetry. For example, in cubic structures the k-points [1/2 0 0], [0 1/2 0] and [0 0 1/2] are equivalent so are all arms of the "star" of the propagation vector. To do this, we split up the different arms of the propagation vector with semi-colons and then if the arms are multi-dimensional then the components are split up with commas. For example, a general order parameter direction for a 3-dimensional irrep at a k-point with only one arm (for example the R-point) would be denoted (a, b, c). A 2-dimensional irrep with 3 arms to its propagation vector (e.g. an X or M point irrep) would have a general OPD denoted by $(a, b; c, d; e, f)$.

1.4 Negative Thermal Expansion

1.4.1 Thermal Expansion

The thermal expansion of materials upon heating is so commonplace that any material that doesn't display this property is worthy of study. Accounting for the volume changes of different materials with temperature is a key aspect that must be considered when designing something expected to undergo significant temperature changes such as devices intended for use in space, or in heaters. If a material showed a volume contraction upon heating, termed negative thermal expansion (NTE), this could be used to compensate for the positive thermal expansion (PTE) of other materials. Research into NTE materials was kickstarted[44] in 1996 with the rediscovery of large, isotropic NTE in ZrW_2O_8 (Fig 1.11) by Evans *et al*[45]. This work also took the key step of linking the observed NTE to the crystal structure. Before this work, reports of NTE were scarce and were often dismissed. Since then, however, research into the area has increased significantly and several new families of NTE materials have been discovered.
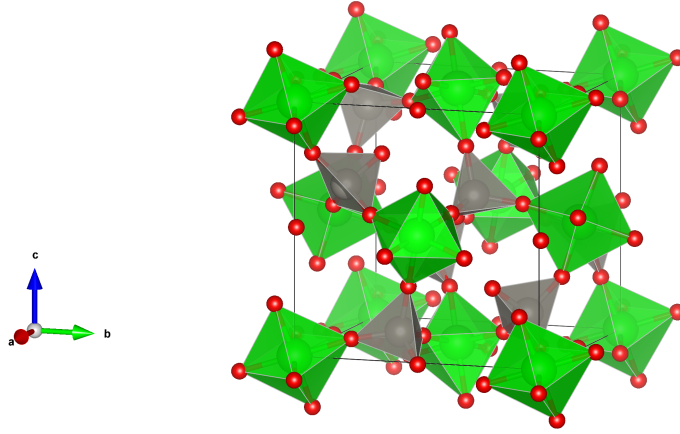
Figure 1.11: The structure of ZrW_2O_8, showing the ZrO_6 octahedra (green) and WO_4 tetrahedra (grey).

There are a variety of different origins of NTE and it can manifest in materials in a number of different ways. In this thesis, I focus on materials which show negative thermal expansion with a purely structural origin. Before introducing the theories behind the vibrational origin of thermal expansion and any departures from it, I will give a brief overview of the range of negative thermal expansion materials. Framework materials, such as the AM_2O_8 (A = Zr, Hf and M = W, Mo) and the Prussian blue analogues, are the most well-known class of NTE materials and have a vibrational origin to their anomalous thermal expansion behaviour. There are a wide range of possible origins to NTE, however.

Common non-vibrational mechanisms for NTE include the magneto-volume effect, as exhibited by the anti-perovskite manganese nitrides[46, 47, 48], which have a large volume contraction on transition from a low-temperature antiferromagnetic phase to a high-temperature paramagnetic phase. Competing magnetic phases of different volumes can also lead to NTE, as seen in the compound $Hf_{0.6}Ti_{0.4}Fe_2$[49]. The magnitude of spontaneous polarisation in a ferroelectric material with a displacive origin is inherently linked to the lattice parameter in the direction of polarisation. This spontaneous volume ferroelectrostriction is evident in the perovskite $PbTiO_3$, which exhibits NTE behaviour along the c-axis in its tetragonal phase[50]. Charge transfer is another possible mechanism for NTE. The ionic radius of an ion is dependent on its oxidation state, with ions of different elements changing with different amounts. The transfer of an electron between two neighbouring ions can then result in a reduction in the combined ionic radii of the two ions. This process is seen in $BiNiO_3$, which has coexisting phases with different oxidation states at
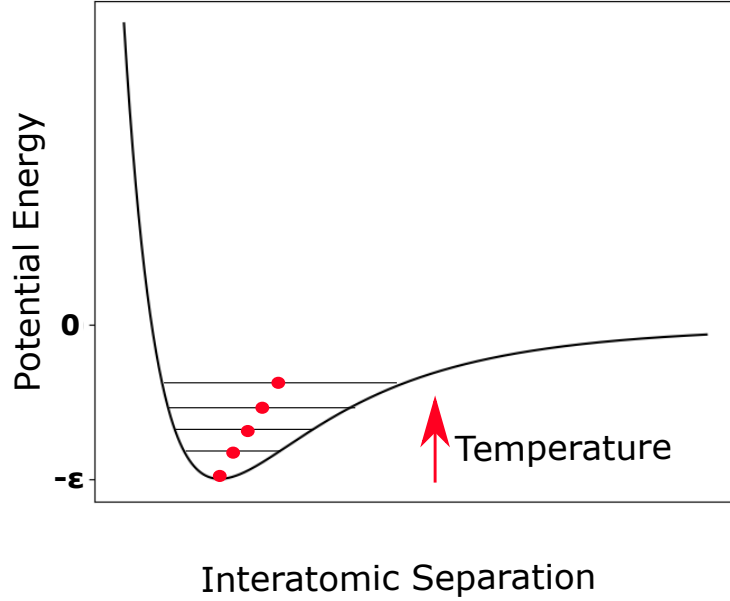
Figure 1.12: A plot of the interatomic potential against interatomic separation, as defined by the Lennard-Jones potential. The position of the energy minimum is $2^{1/6}\sigma$. Lines are drawn to show the effect of increasing temperature on the equilibrium separation of the two atoms, which are shown in red.

pressure above 1.5 GPa. This charge transfer transition can be brought closer to ambient pressure *via* doping with La[51]. Before getting deeper into theories of why materials might exhibit NTE, however, it is first necessary to discuss the more usual case: why the majority of materials show positive thermal expansion.

The basic origin for the thermal expansion of a material lies in the potential energy of two nearby atoms[52]. The simplest interaction model is given by the Lennard-Jones potential:

$$V(r) = 4\epsilon[\left(\frac{\sigma}{r}\right)^{12} - \left(\frac{\sigma}{r}\right)^{6}] \tag{1.54}$$

where r is the interatomic separation, ϵ is the depth of the potential well and σ is the point at which the function crosses zero. The shape of this function, displayed in Fig 1.12, is asymmetric with respect to the energy minimum which reflects the fact that as the atoms get closer together it will become harder and harder to decrease their separation further and that as you increase their separation, the potential energy tends to zero. At 0 K, the atoms will have no kinetic energy and their separation will be at the point with the lowest potential energy. As temperature is raised, the atoms start to vibrate due to their increased kinetic energy. The asymmetric

nature of the interatomic potential means the equilibrium point changes when the atoms gain energy. The width of the potential well is larger on the side of increased atomic separation, and so the equilibrium separation of the two atoms increases with increasing temperature. This picture of thermal expansion gets more complex when expanding it to higher dimensions and periodic solids: the impact of phonons upon the thermal expansion of solids will be discussed later.

1.4.2 Quantifying Thermal Expansion

We can quantify thermal expansion in solids by determining the relative change in volume for a given change in temperature at a constant pressure[36]. This coefficient of thermal expansion is defined as:

$$\alpha_V = \frac{1}{V}\left(\frac{\partial V}{\partial T}\right)_P \tag{1.55}$$

It is also useful when discussing materials which show anisotropic thermal expansion to define a coefficient of linear thermal expansion $\alpha_L = \frac{1}{L}\left(\frac{\partial V}{\partial T}\right)$, but this is beyond the scope of this thesis.

We can use standard thermodynamic relations to express α_V in terms of other thermodynamic properties. The most useful of these is to use a triple rule relation:

$$\left(\frac{\partial T}{\partial V}\right)_P \left(\frac{\partial V}{\partial P}\right)_T \left(\frac{\partial P}{\partial T}\right)_V = -1 \tag{1.56}$$

to express $(\partial V/\partial T)_P = -(\partial P/\partial T)_V(\partial V/\partial P)_T$, and use the Maxwell relation $(\partial P/\partial T)_V = (\partial S/\partial V)_T$ to obtain:

$$\alpha_V = -\frac{1}{V}\left(\frac{\partial V}{\partial P}\right)_T \left(\frac{\partial S}{\partial V}\right)_T \tag{1.57}$$

Using the definition of the isothermal bulk modulus, $B = -V(\partial P/\partial V)_T$, this becomes:

$$\alpha_V = \frac{1}{B}\left(\frac{\partial S}{\partial V}\right)_T = \frac{1}{B}\left(\frac{\partial P}{\partial T}\right)_V \tag{1.58}$$

Again using a triple rule relation:

$$\left(\frac{\partial S}{\partial V}\right)_T \left(\frac{\partial V}{\partial T}\right)_S \left(\frac{\partial T}{\partial S}\right)_V = -1 \tag{1.59}$$

we can introduce the heat capacity, $C_V = T(\partial S/\partial T)_V$, into the expression for the

coefficient of thermal expansion:

$$\alpha_v = -\frac{C_V}{BT}\left(\frac{\partial T}{\partial V}\right)_S \tag{1.60}$$

This can be simplified by defining a quantity $\gamma = -(\partial lnT/\partial lnV)_S$ known as the macroscopic Grüneisen parameter[53], leaving the expression for the volume coefficient of thermal expansion as

$$\alpha_V = \frac{C_V \gamma}{BV} \tag{1.61}$$

1.4.3 Thermal Expansion and Phonons

It was mentioned in section 1.4.1 that the thermal expansion of a bond between two atoms is a result of the vibration of these atoms. Vibrations in crystals can be broken down into quantised normal modes known as phonons, as discussed in section 1.3. We can relate the frequencies of these phonons, $\omega(k)$, to thermodynamic quantities by constructing a partition function, Z[32]. The general form for the partition function is defined as $Z = \sum_{j=1}^{\infty} \exp(-E_j/k_B T)$ where E_j is the energy of the jth excited state. Using the properties of phonons and some series identities, this gives us $Z = \prod_k n(\omega_k, T)$ where

$$n(\omega_k, T) = \frac{1}{\exp(\hbar\omega_k/k_B T) - 1} \tag{1.62}$$

is the Bose-Einstein distribution. When accounting for the potential energy of the crystal while the atoms are at rest and the zero-point motion, the partition function becomes:

$$Z = \exp(-E_N/k_B T)\prod_k \frac{\exp(-\hbar\omega_k/2k_B T)}{1 - \exp(-\hbar\omega/k_B T)} \tag{1.63}$$

where E_N is the potential energy of the crystal. From this, we can determine the Helmholtz free energy,

$$F = -k_B T lnZ = E_N + k_B T\sum_k ln[2\sinh(\hbar\omega_k/2k_B T)] \tag{1.64}$$

and the pressure,

$$P = -\left(\frac{\partial F}{\partial V}\right)_T = -\frac{\partial E_N}{V} - \frac{\hbar}{2}\sum_k \frac{\partial \omega_k}{\partial V} - \hbar\sum_k n(\omega_k, T)\frac{\partial \omega_k}{\partial V} \tag{1.65}$$

We can use this expression for pressure to calculate the coefficient of thermal expansion, but first we must make some approximations for the phonon frequencies. We

cannot directly use the harmonic approximation, since the harmonic nature of the vibrations means they don't have an intrinsic volume dependence. To account for this without considering anharmonic terms in the Hamiltonian, the quasi-harmonic approximation is used[54]. In this expansion of the harmonic approximation, it is assumed that the atomic forces change with the volume as a result of anharmonic components of the potential energy. Since the force constants change, so do the phonon frequencies, which can then be recalculated using the harmonic approximation. Using this, the phonon frequencies retain their lack of explicit dependence on temperature but gain an intrinsic volume dependence. Consequently, when differentiating the expression for pressure in equation 1.58 to obtain the coefficient of thermal expansion, we can ignore all but the last term, which is the only one with an explicit dependence on temperature[32]. This gives us

$$\alpha_V = -\frac{1}{B}\hbar \sum_k \frac{\partial n(\omega_k, T)}{\partial T} \frac{\partial \omega_k}{\partial V} \tag{1.66}$$

as an expression of the coefficient of thermal expansion in terms of phonon frequencies. Since the total heat capacity $C_V = \sum_k \hbar\omega_k(\partial n(\omega_k, T)/\partial T)$, we can define a heat capacity for each mode

$$c_k = \hbar\omega_k \frac{\partial n(\omega_k, T)}{\partial T}, C_V = \sum_k c_k \tag{1.67}$$

Similarly, a mode Grüneisen parameter can be defined as

$$\gamma_k = -\frac{V}{\omega_k}\frac{\partial \omega_k}{\partial V} = -\frac{V}{2\omega_k^2}\frac{\partial \omega_k^2}{\partial V} \tag{1.68}$$

It is useful to express the mode Grüneisen parameter in terms of ω_k^2 since these are the quantities calculated directly from the force constants by diagonalisation of the dynamical matrix. The overall thermal expansion coefficient is given by

$$\alpha_V = \frac{C_V \bar{\gamma}}{BV} \tag{1.69}$$

where the mean Grüneisen parameter $\bar{\gamma} = \frac{1}{C_V}\sum_k c_k\gamma_k$ is equivalent to the macroscopic Grüneisen parameter defined in equation 1.61. Since C_V, B and V are positive, the sign of the thermal expansion is determined by the sign of the mean Grüneisen parameter. This is determined by the contributions of the individal mode Grüneisen parameters and, as can be seen in equation 1.68, modes with a lower frequency, and consequently a lower energy, will have a larger Grüneisen parameter
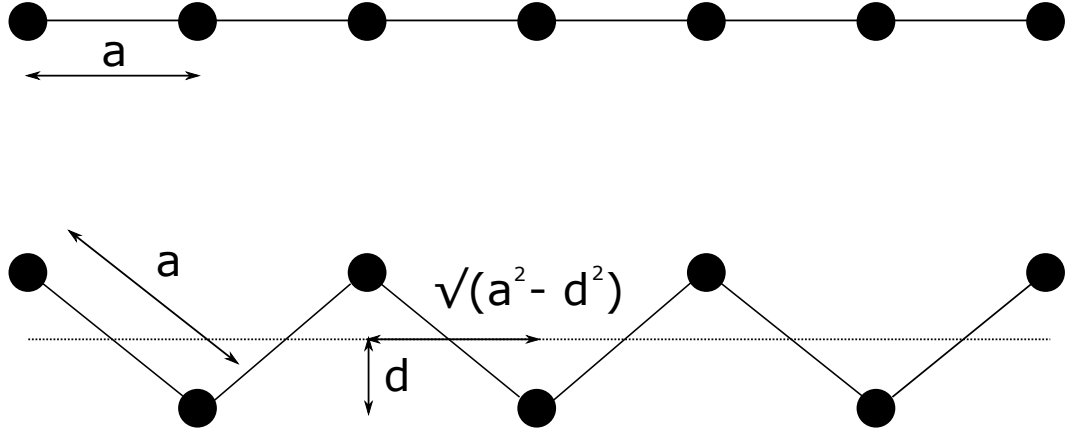
Figure 1.13: A schematic diagram showing the effect of transverse vibrations on a chain of atoms. The bond length is fixed at a value, a, and under a transverse displacement of magnitude d, the distance between atoms in the direction of the original bonds is shortened to a distance $x = \sqrt{a^2 - d^2}$, which is strictly shorter than a.

and, therefore, a bigger contribution to overall thermal expansion.

1.4.4 Phonons and Negative Thermal Expansion

In the previous section, it was discussed that if phonon modes which caused a volume shrinkage had a large enough contribution to the mean Grüneisen parameter then the system as a whole would show negative thermal expansion. This begs the question of which types of distortion can produce NTE. If we imagine a chain of atoms in one dimension, there are two types of vibrational motion they could undergo. They can vibrate in directions along the chain or perpendicular to it. These types of vibrations are known as longitudinal and transverse, respectively. Given a fixed bond length between atoms in this chain, transverse vibrations will shorten the gap between atoms along the chain (Fig 1.13). This phenomenon is known as the tension effect. Theoretically, all systems should exhibit this type of distortion, however, the vast majority of materials show positive thermal expansion. This indicates that either these modes are too high in energy to provide an overall negative thermal expansion or there are too few of them present in the system, therefore, to find NTE materials, we must find materials with low energy transverse displacive modes. A large number of materials which exhibit phonon-driven negative thermal expansion are network materials. These materials consist of a 3-dimensional network of linked polyhedra[55]. The archetypal NTE material ZrW_2O_8 is an example of this, consisting of corner-sharing ZrO_6 octahedra and WO_4 tetrahedra[45]. Other
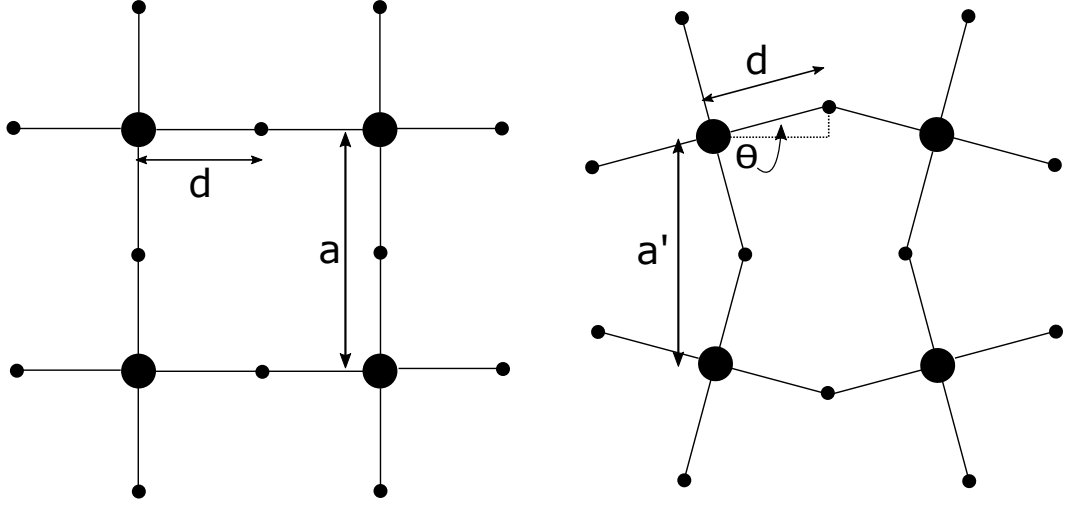
Figure 1.14: A diagram showing how rigid unit modes can lead to lattice contraction.

examples include SiO_2[56], ZrV_2O_7[57, 58], M_2O (M = Cu, Ag)[59, 60, 61] and $AlPO_4$[62]. These network materials often undergo symmetry-lowering phase transitions *via* collective rotations of their constituent polyhedral units. For example, metal trifluorides, such as AlF_3, consist of corner sharing MF_6 octahedra (M = Al, Cr, Ga, V, Fe, In and more) and typically adopt a rhombohedral phase at room temperature[63]. This structure is distorted from the cubic (un-tilted) phase *via* the triply degenerate R-point octahedral tilt mode. These types of distortions are typically termed rigid unit modes (RUMs). Since these modes cause phase transitions, above the phase transition they must be low in energy. These modes also consist of transverse displacements of the lighter elements in the polyhedra and consequently also commonly have a negative Grüneisen parameter[64]. Figure 1.14 depicts how RUMs can lead to negative thermal expansion: for a material with an average structure made of corner-sharing octahedra with rigid bonds of length d, the untilted average structure would have a lattice parameter $a = 2d$ and a volume $V = a^3 = 8d^3$. If the material undergoes a tilt of angle θ along one of the <1 0 0> directions, then the new lattice parameters perpendicular to this direction will be $a' = 2d \cos \theta$ and the volume $V' = 8d^3 \cos^2 \theta < V$. The average crystallographic structure is not sensitive to dynamic tilt modes, but the pairwise interactions, as probed by a pair distribution function, will change.

Since not all network materials exhibit NTE, there must be other factors that determine its presence within a material. This is one of the key reasons we chose to demonstrate our symmetry-adapted PDF analysis technique on negative thermal expansion materials.
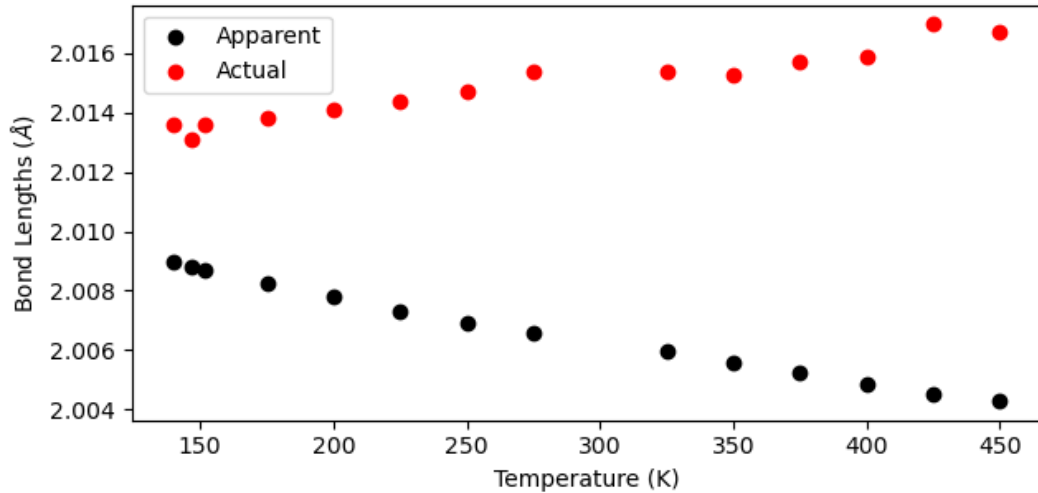
Figure 1.15: A plot of the apparent and actual bond lengths of the nearest neighbour Sc-F bond in ScF_3 determined by X-ray Bragg diffraction and pair distribution functions, respectively. Total scattering data were collected on the P02.1 beamline of the PETRA III synchrotron at DESY. The same data were used for the Rietveld refinments of the average structure and to generate the PDFs.

1.4.5 Structural Studies of Negative Thermal Expansion Materials

A key aspect of the study of materials which exhibit negative thermal expansion due to their structure is determining said structure. The advancements in neutron and X-ray generation facilities, serving to allow faster collection of data and, therefore, improved ability to study the changes in structure with temperature, is a key factor in why the field took off after the work of Evans *et al* in 1996. Before this seminal work in the field, reports of materials exhibiting NTE were often dismissed as inaccurate[65]. However, while the refinement of Bragg peaks obtained by neutron and X-ray powder diffraction is very useful in determining the thermal expansion behaviour of a material, the average structure view it obtains can obfuscate the origin of NTE[36]. For example, in a lot of NTE materials, the apparent nearest-neighbour bond lengths obtained from the average structure shrink upon heating, which goes against the basic physics of the interatomic potentials discussed earlier in this section. An example of this is displayed in Fig 1.15. This picture can be cleared up by looking at the local structure of the material, which can be studied using pair distribution functions obtained by the total scattering method. The peaks in the PDF give actual rather than apparent bond lengths and are also sensitive to the vibrations that give rise to NTE. The peak positions can be analysed by hand to show deviation from the average structure. For example, this method has been used

45
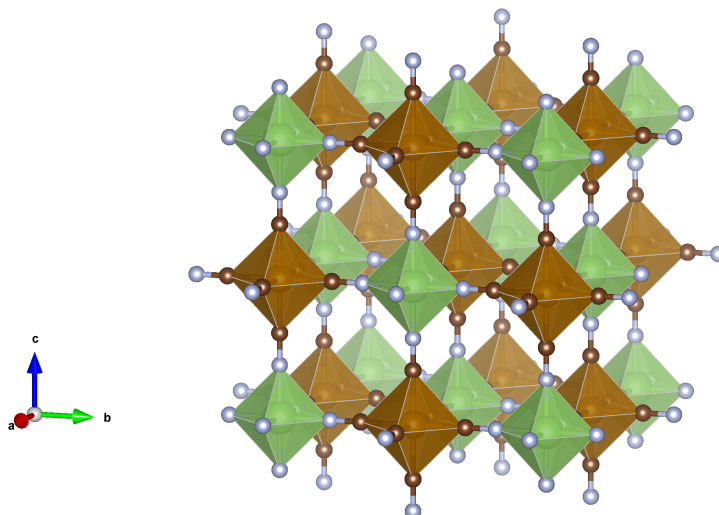
Figure 1.16: The structure of the negative thermal expansion material $GaFe(CN)_6$, showing GaN_6 (green) and FeC_6 (brown) octahedra, connected by cyanide bonds.

to analyse $GaFe(CN)_6$, a material showing isotropic NTE. It is formed of alternating GaN_6 and FeC_6 octahedra, linked by their corners with cyanide bonds (Fig 1.16). In the average structure, the -Ga-N≡C-Fe- linkages are straight, but the bond lengths from the PDF are too long to fit in the average structure picture meaning that the C and N atoms must be displaced from their position in the average structure in a direction perpendicular to the linkage[66]. Another example of this type of analysis was used to examine the NTE material β-cristobalite. This structure is formed of corner-sharing SiO_4 tetrahedra, with the silicon atoms arranged in the same way as the carbons in the crystal structure of diamond. The ideal value for the Si-O bond length in this structure is $\sqrt{3}a/8$, where a is the cubic lattice parameter. The actual bond lengths, as determined by PDF analysis, are slightly larger than this, meaning that the Si-O-Si bonds are bent rather than straight[67]. A significant proportion of PDF analysis of NTE materials is of this nature, using trends in peak positions with changing temperature to determine a mechanism for NTE[68, 69, 70, 71, 72]. Studies of this type have led to a disagreement in the origin of NTE in ZrW_2O_8. Models using reverse Monte Carlo analysis of the PDFs suggest the RUM theory of NTE is accurate[73, 74], whilst others conclude that the Zr-W linkage is too stiff to allow for bending of the W-O-Zr link which would be necessary for whole-body rotations of the linked ZrO_6 and WO_4 polyhedra and that instead, the NTE arises from translations of the WO_4 tetrahedra along the <1 1 1> axes[75]. Subsequent molecular dynamics simulations have concluded that neither picture is fully adequate in explaining the NTE[76]. The origin of NTE in more simple structures like

ScF$_3$ is also disputed, with some still subscribing to the RUM model[36] while some conclude that the transverse vibration of the F atoms is entirely uncorrelated[77]. Therefore, it is clear that the field is ripe for a different technique for analysing the PDF data of NTE materials.

1.5 Hybrid Perovskites

1.5.1 Perovskites

The term perovskite refers to a class of materials with the same structure as the mineral perovskite (CaTiO$_3$), discovered in Russia in 1839 and named after mineralogist Lev Perovski[78]. Its structure is also commonly found in other materials with the general formula ABX_3, with the X atoms typically being oxygen or a halide and the A and B atoms being inorganic cations, including bridgmanite ((Mg,Fe)SiO$_3$), the most common phase in the Earth's mantle[79]. The ideal perovskite, displayed in Fig 1.17, is formed of a network of corner-sharing BX$_6$ octahedra with A ions sitting in the centre of the gaps in this network, within a cubic $Pm\bar{3}m$ lattice. There are a large number of different elements that have been put on the A and B sites in various perovskite materials, and as such this class of compounds can have a wide array of interesting properties, such as ferroelectricity, ferromagnetism, superconductivity, piezoelectricity and recently photovoltaic behaviour[80]. Another consequence of the variety of elements that can sit on the A or B site is that the structure of perovskite materials can often be distorted away from the ideal cubic structure[81, 40] and, in fact, the eponymous perovskite, CaTiO$_3$, is one of these (Fig 1.19)[4, 82]. These distortions arise due to the strict size requirements of the ionic radii in the cubic structure. In the hard sphere model, the cubic lattice parameter $a = 2r_B + 2r_X$ and the diagonal of one "face" of the cubic unit cell $d = 2r_A + 2r_X$, where r_A, r_B and r_X are the ionic radii of the A, B and X atoms respectively. From Pythagoras' theorem, this gives $r_A + r_X = \sqrt{2}(r_B + r_X)$. Deviations from this ideal picture are likely to result in a distorted structure. This idea was first proposed by Victor Goldschmidt[83], which he captured using the idea of his eponymous tolerance factor

$$t = \frac{r_A + r_X}{\sqrt{2}(r_B + r_X)} \tag{1.70}$$

Values of t between 0.9-1 are most likely to result in the cubic perovskite structure, and values of t $<\approx$ 0.71 are likely to result in unrelated structures. Whilst this tolerance factor is often accurate for oxide- and fluoride-based perovskites (able to predict between perovskite and non-perovskite phases for ABX_3 materials approximately
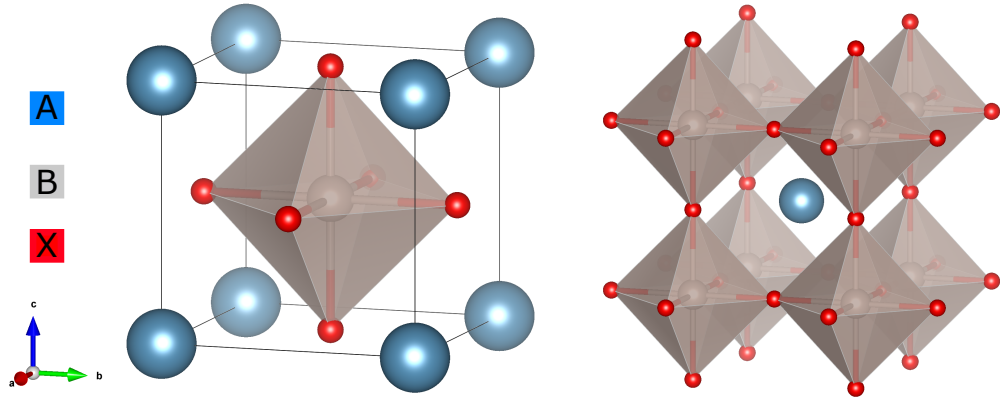
Figure 1.17: A diagram of the archetypal perovskite structure in both the standard setting (left) and alternate setting (right).

83% of the time), it is considerably less accurate for other halide perovskites. As a result of this, a new tolerance factor, τ, was recently proposed using a data-analytics approach:

$$\tau = \frac{r_X}{r_B} - n_A \left(n_A - \frac{r_A/r_B}{ln(r_A/r_B)} \right) \tag{1.71}$$

where n_A is the oxidation state of A. Using this definition, a value of $\tau < 4.18$ indicates a perovskite with an accuracy of 92%[84].

In addition to materials with the ABX_3 general formula, there are other types of structure that generally fall under the perovskite umbrella but aren't true perovskites. These include anti-perovskites, where the X-site is now a cation and the A and B sites anions[85, 48, 46]; double perovskites ($A_2BB'O_6$), where half of the B cations are replaced by a different cation, B', resulting in a rock salt ordering of the octahedra[86, 87] and Ruddlesden-Popper phases ($A_{n+1}B_nX_{3n+1}$), which consist of layers of the perovskite structure separated by layers of the rock salt structure[88, 89]. Each perovskite layer is a number of archetypal perovskite unit cells thick, which is governed by n in the general formula (Fig 1.18). There is also the class of hexagonal perovskites. The archetypal perovskite structure ican be described as a cubic-close-packed lattice of AO_3 layers, with the B cations occupying the octahedral cavities to balance the charge. For hexagonal perovskites, the layering instead follows the hexagonal-close-packed stacking sequence. This allows for chains of face-sharing octahedra, rather than the more usual corner-sharing octahedra of cubic perovskites[90].

There are two possible settings for the parent $Pm\bar{3}m$ perovskite structure. Unless otherwise stated, the setting A $1a$ $(0,0,0)$; B $1b$ $(\frac{1}{2},\frac{1}{2},\frac{1}{2})$; X $3c$ $(0,\frac{1}{2},\frac{1}{2})$ is
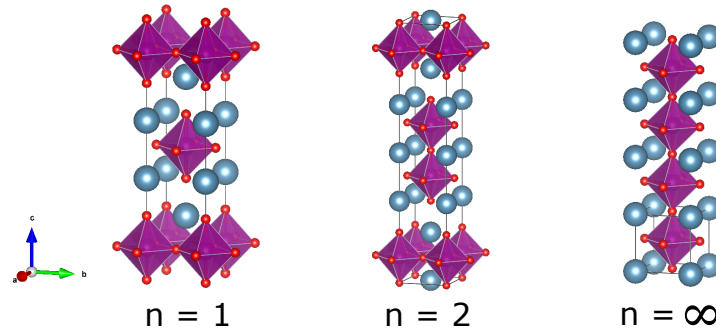
Figure 1.18: Ruddlesden-Popper phases with $n = 1, 2$ and ∞. The latter corresponds to the archetypal perovskite structure.

used. The alternate setting, with the B site at the origin, results in many of the irreducible representation labels changing[91].

1.5.2 Distortions in Perovskites

As discussed earlier in this section, due to the strict size requirements on the ions in the ideal cubic perovskite structure, perovskite materials are often distorted away from this. There are a few mechanisms for these distortions, which are octahedral tilting (or RUMs, as discussed in section 1.4.4), octahedral distortions *via* bond-bending or bond-stretching (typically termed scissoring and Jahn-Teller modes, respectively) and polar (and anti-polar) displacements. In addition, there are displacements that can arise as a result of ion-ordering[40]. Sometimes, these distortions can cause the material to show interesting properties. A prime example of this is $BaTiO_3$, which is ferroelectric in its low temperature phases due to an ordered displacement of the Ti cation off the centre of the octahedra[92].

Octahedral tilts in perovskites were classified by Glazer in 1972 who formed a standard notation to describe them[93, 94]. He considered all tilts as a combination of component tilts about the three pseudo-cubic axes, with the magnitude of the tilts in each direction, in the order [1 0 0], [0 1 0], [0 0 1] being denoted by a letter. For example, 3 unequal tilts would be denoted *abc* and tilts of equal magnitude represented by repetition of the appropriate letter, *e.g.*, *aac*. In addition, subsequent tilts along the tilt axis can either be rotated in the same sense or the opposite sense to the first tilt, which are usually described as "in-phase" and "out-of-phase" tilts, respectively. This is represented by a superscript to the letter describing the tilt, with a + denoting an in-phase tilt and a - an out-of-phase tilt. A superscript 0 denotes there is no tilt in that direction. Putting this all together, if we have an out-of-phase tilt along the *c*-axis, which would result in lowering the symmetry to

49
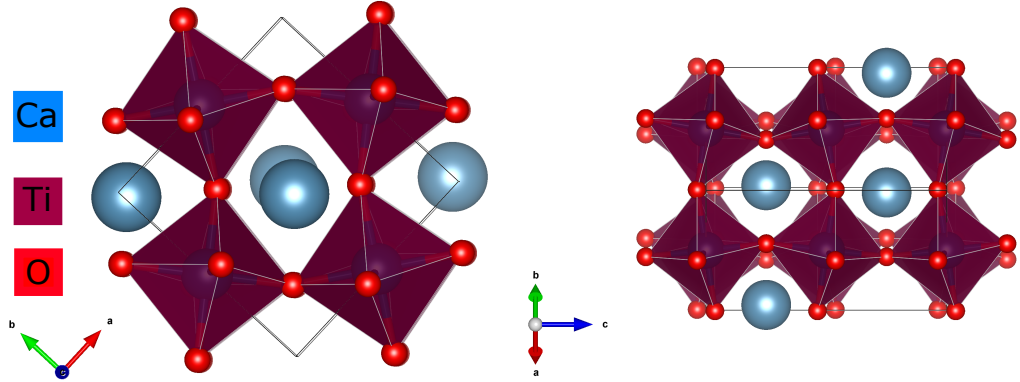
Figure 1.19: A depiction of the unit cell of $CaTiO_3$, showing the distorted *Pbnm* structure which exhibits an $a^-a^-c^+$ tilt system. The lattice parameters of this unit cell, a, b and c, are related to the pseudo-cubic lattice parameter *via* the relations $a \approx b \approx \sqrt{2a_p}$ and $c \approx 2a_p$. The structure depicted here is as published in [4].

$I4/mcm$, the tilt system is denoted by $a^0a^0c^-$ in Glazer notation. This work was expanded upon by Howard and Stokes using a group-theoretical analysis[95]. It reduced the 23 possible distortions suggested by Glazer to 15 and also clarified the group-subgroup relationships between the different distortions.

1.5.3 Hybrid Perovskites

Typically, perovskites are completely inorganic materials, *i.e.*, A, B and X are all inorganic. The family of materials known as hybrid or molecular perovskites are a departure from this norm, with A, X or both being molecular ions. They are typically classified by the type of molecular ion used. Replacing the X site with a molecular ion has the effect of introducing new types of distortion into the perovskite family: unconventional tilts, where neighbouring octahedra perpendicular to the tilt axis can be rotated in the same manner, and columnar shifts, where planes of octahedra can shift relative to each other. Replacing the A site with a molecular ion can result in dipolar or higher-order moments being present[96].

The most famous of this class of materials are the methylammonium ($CH_3NH_3^+$, commonly abbreviated to MA) lead halides, which have the general formula $MAPbX_3$, $X = $ I, Br, Cl[97]. They are a fast-growing research area due to their promise as low cost and highly efficienct solar cell materials. Since $MAPbI_3$ was first studied for use as a photovoltaic in 2009, the efficiency of devices made using it has increased rapidly from an initial 3.9% [98] to greater than 20% today [99], which can rival, or even out-perform, the best single cell silicon devices. These materials

Table 1.2: A table showing the different types of distortion in perovskites and which irreducible representation they are associated with for the setting with the A atom at the origin of the unit cell. The atoms the distortion is acting on, either A, B or X, is indicated by the brackets after the distortion type.

Distortion / K-point	Γ	X	M	R
Strain	Γ_3^+ ; Γ_5^+			
Cation order (A)		X_1^+	M_1^+	R_1^+
Cation order (B)		X_3^-	M_4^+	R_2^-
(Anti-)Polar order (A)	Γ_4^-	X_3^- ; X_5^-	M_3^- ; M_5^-	R_4^-
(Anti-)Polar order (B)	Γ_4^-	X_1^+ ; X_5^+	M_2^- ; M_5^-	R_5^+
Anion Order (X)		X_1^+	M_4^+	R_5^+
Jahn-Teller (X)	Γ_3^+	X_3^-	M_3^+	R_3^-
RUM (X)			M_2^+	R_5^-
Semi-RUM (X)	Γ_5^-	X_2^+ ; X_5^+ ; X_5^-	M_5^+ ; M_5^-	R_4^-

offer a number of advantages over Si [100], such as the aforementioned increased efficiency, a higher absorption cross-section[101], low charge-carrier recombination rates[102] and a long charge-carrier diffusion length[103]. They also have some significant drawbacks, however, the most significant of which is the instability of the best-performing material, MAPbI$_3$ [104, 105, 106, 107]. It degrades when exposed to heat, light and humidity, which is compounded by the fact that one of its degradation products, PbI$_2$, is toxic and water-soluble. Improving the stability of devices made using MAPbI$_3$ is a significant research area [108], with improvements made by incorporating different anions and cations into the structure such as small amounts of the other halides (Br and Cl) [109, 110] or replacing some of the organic cations with inorganic alternatives such as Cs [111, 112]. Other strategies include device engineering such as adding a hydrophobic passivation layer on top of the perovskite absorber[113]. In addition to improving the stability of these devices, efforts are being made to replace the lead, chiefly by substitution with tin [114, 115], due to the aforementioned toxicity concerns.

All three of the methylammonium lead halides attain the archetypal cubic perovskite structure at high temperatures[97]. A key difference between these perovskites and all-inorganic perovskites is that the A-site is disordered over many different directions in the higher-symmetry phases. In the cubic phase of all three methylammonium lead halides, the MA cation is fully disordered and recent NMR and quasi-elastic neutron scattering measurements show that these cations are close to having the orientational freedom of a free MA cation[116, 117, 118]. All three compounds undergo symmetry-lowering phase transitions to tetragonal and orthorhom-
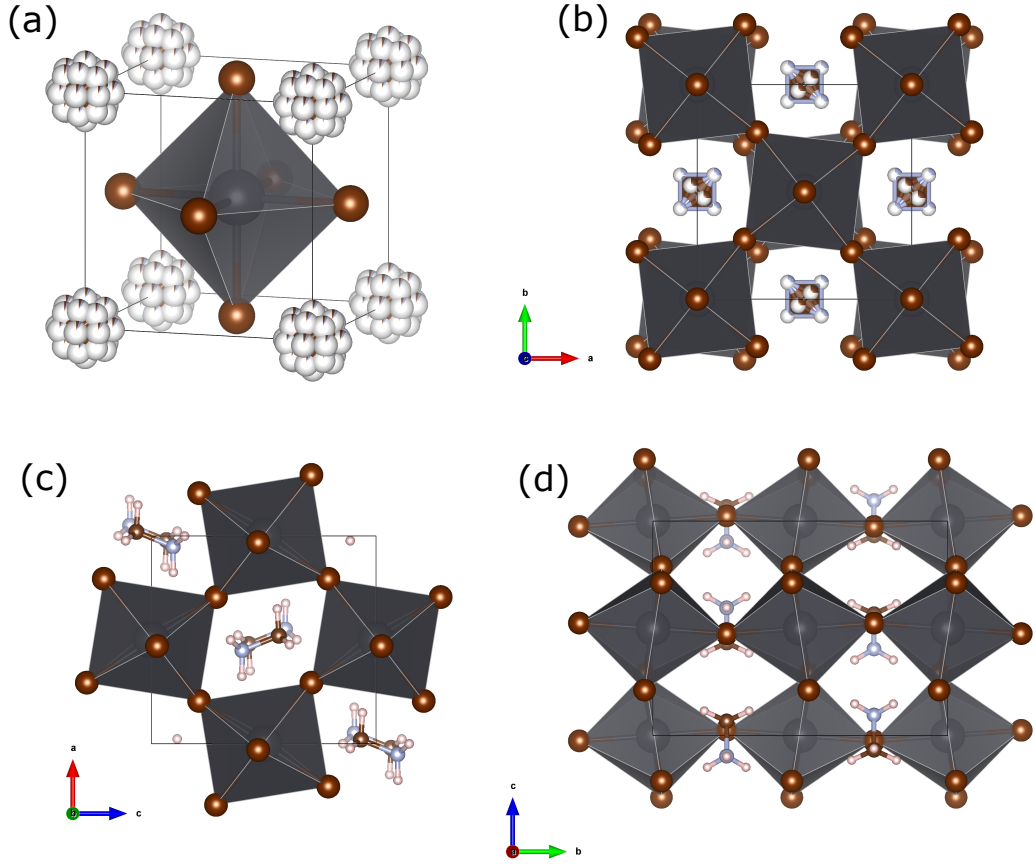
Figure 1.20: Diagrams of the structures of MAPbBr$_3$. (a) shows the cubic structure with the fully disordered A-site orientation. (b) shows the $I4/mcm$ tetragonal structure and (c) and (d) show the orthorhombic structure. For clarity, the hydrogens are not shown in (a) and (b).

bic structures as temperature is lowered. An increase of the ordering of the MA cations accompanies these phase transitions[119, 120, 121, 122, 123]. The transition to the tetragonal phase (at $\approx$ 327, 237 and 179 K for X = I, Br and Cl respectively) occurs *via* an $a^0a^0c^-$ tilt for X = I and Br and *via* an $a^0a^0c^+$ tilt for X = Cl. The MA cations are less disordered in these phases, but the exact nature of this disorder is still up for debate. The exact space group of the phase is also disputed, with most reporting an $I4/mcm$ space group for X = I and Br [124, 125], but some studies suggesting that $I4cm$ is the true symmetry, which is the polar maximal subgroup of $I4/mcm$ and so implicitly allows for ferroelectricity [126, 127]. The lowest temperature phase (below $\approx$ 162, 145 and 173 K for X = I, Br and Cl respectively) of each compound is in the orthorhombic space group, $Pnma$[128, 129]. In this phase, the MA cations are fully ordered in an anti-parallel arrangement and the octahedra

Table 1.3: A table showing the different structures of the methylammonium lead halides and their transition temperatures.

Phase	Temperature (K)	Space Group
MAPbCl$_3$	> 178.8	$Pm\bar{3}m$
	172.9 - 178.8	$P4/mmm$
	< 172.9	$Pnma$
MAPbBr$_3$	> 236.9	$Pm\bar{3}m$
	155.1 - 236.9	$I4/mcm$
	149.5 - 155.1	Incommensurate
	< 144.5	$Pnma$
MAPbI$_3$	> 327.4	$Pm\bar{3}m$
	162.2-327.4	$I4/mcm$ or $I4cm$
	< 162.2	$Pnma$

are tilted in an $a^+b^-b^-$ arrangement. $Pnma$ is a centro-symmetric space group and so does not allow for ferroelectricity. MAPbBr$_3$, unlike the other two compounds, has an additional phase between the orthorhombic and tetragonal phases. It was originally indexed by Poglitsch and Weber as an additional tetragonal phase with the $P4/mmm$ space group, but the consensus now is that it is an incommensurate phase [130], with recent work assigning it an $Imma$ space group derived by an $a^-b^0a^-$ tilt system, with an additional incommensurate tilt distortion[131]. Recently, total scattering studies of these compounds using neutron and X-ray total scattering have shown a persistence of the low-symmetry phases in the local structure of the cubic phase, suggesting that the PbX$_6$ octahedra are locally distorted, possibly due to interactions with the methylammonium cation [132, 133, 134, 135]. This is reflected in the short-range local structure of the inorganic backbone of the hybrid perovskites remaining very similar across the different structural phases (Fig 1.21). Studies using other methods, such as molecular dynamics and electron scattering, support this picture. Other studies have suggested that the Pb cations undergo a local polar distortion due to their lone pair of electrons[136, 137].

Despite their promising potential for use in photovoltaic devices, the origin of the desirable photovoltaic properties in these hybrid perovskites is not fully understood[138]. All-inorganic halide perovskites can show similar properties, such as low effective masses and low density of states at the valence band maximum[139, 140]. The presence of the MA cation is likely to have at most a subtle effect on these properties of the electronic band structure since the inorganic backbone of the structure providing the frontier states of the electronic band structure, but interaction with the MA cation could still have an indirect effect by modifying bond
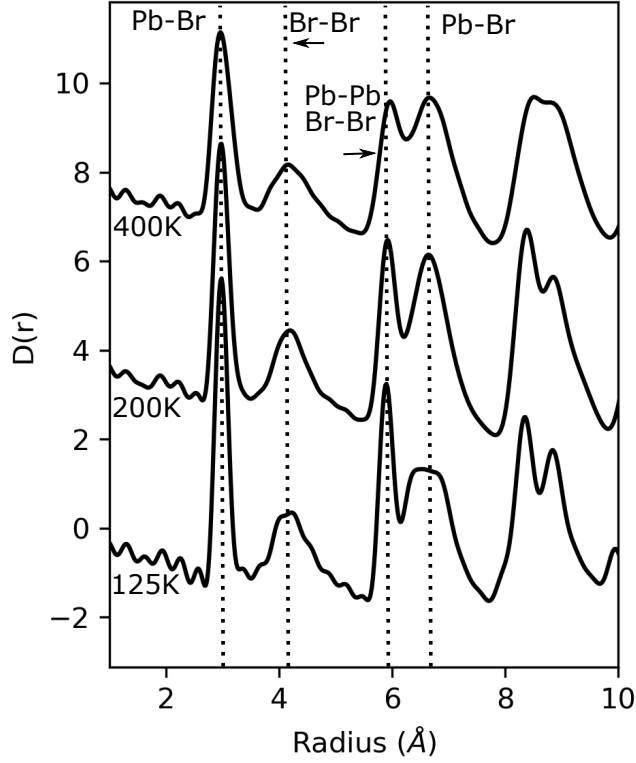
Figure 1.21: A figure showing the similarity between the first four peaks of the pair distribution functions of MAPbBr$_3$ in the $Pnma$, $I4/mcm$ and $Pm\bar{3}m$ phases. The PDFs were generated from data collected at DESY, as described in chapter 5.

lengths and angles *via* hydrogen bonding interactions[141].

The role of the MA cation could be reflected in the improved performance in the tetragonal phase of MAPbI$_3$ compared to the orthorhombic phase[142]. A lot of studies have suggested that the tetragonal phase is actually in the non-centrosymmetric space group, $I4cm$, rather than the $I4/mcm$ space group it was originally assigned. This revision has two main implications - the first is that it would allow for ferroelectricity, as has been observed experimentally[143, 144, 145, 146]. Theoretical studies of another hybrid perovskite, (benzylammonium)$_2$PbCl$_4$, have also shown that ferroelectric alignment of the polar groups inhibits non-radiative charge recombination, possibly by suppressing higher frequency phonon contributions to electron-phonon coupling[147]. The presence of ferroelectric domains has also been shown to create internal junctions in hybrid perovskites[148]. Molecular ferroelectricity could also explain other observed properties in hybrid perovskites, such as anomalous hysteresis[149]. The second effect is that the selection rules of the $I4cm$ space group allow the Rashba effect, otherwise forbidden in $I4/mcm$.

This has been hypothesised to also slow down the recombination of charge carriers since it has been shown to change the band gap in cubic $MAPbI_3$ from direct to indirect[150, 151, 152, 153, 154]. The origin of this low recombination rate is still an open question, since it is also lowered by the addition of Cl ions into $MAPbI_3$. Polaronic effects are expected to contribute to this. Polarons are a quasi-particle and are effectively charge carriers coupled with a local polar lattice deformation. This screens the charge carrier from the electric field within the lattice, and polaron formation is often energetically favourable compared to the formation of a bare charge carrier. The structure of $MAPbX_3$ is highly dynamic and so polaron formation could be expected to play a greater role in these materials compared to photovoltaics with harder lattices[155, 156, 157]. The dynamic structure of these materials has also been linked to band gap fluctuations, which could assist in the initial stages of charge separation[158, 159].

1.6   Outline of the Thesis

As previously stated, the main aim of this thesis is to introduce a symmetry-adapted technique for analysing pair distribution function data. The primary goal for this technique is to determine how the local structure of a material deviates from the average and use this information to gain insight into how the lattice dynamics are associated with the properties of a material.

Chapter 1 introduced the methods of total scattering and representational analysis and also lays out background information for the types of materials studied in later chapters. In the second chapter, a paper demonstrating the use of symmetry-adapted PDF analysis (SAPA) is presented, covering the basics of analysing PDFs in the Topas Academic software and how to implement SAPA in said software. The later chapters cover applications of this technique.

In chapters 3 and 4, the technique is applied to the negative thermal expansion materials ScF_3, $CaZrF_6$ and ReO_3. The materials ScF_3 and ReO_3 are iso-structural and are directly comparable, whilst $CaZrF_6$ is a "double perovskite" equivalent. By using the SAPA technique on these 3 compounds, we gain useful insight into the mechanism that drives the negative thermal expansion they exhibit.

In chapter 5, the SAPA technique is used to analyse the cubic phases of the hybrid perovskites $MAPbX_3$, X = I, Br, Cl. Benefiting from the comparitively low scattering power that organic elements have for X-rays we were able to focus on the inorganic dynamics and then use density functional theory calculations to determine how the local distortions effect material properties like the electronic band structure.

Lastly, chapter 6 gives the conclusion of the work presented.

Chapter 2

Symmetry Adapted Pair Distribution Function Analysis (SAPA): A Novel Approach to Evaluating Lattice Dynamics and Local Distortions from Total Scattering Data

Symmetry-adapted pair distribution function analysis (SAPA): a novel approach to evaluating lattice dynamics and local distortions from total scattering data

**Tobias A. Bird,[a] Anna Herlihy[a,b] and Mark S. Senn[a]***

[a]Department of Chemistry, University of Warwick, Gibbet Hill, Coventry CV4 7AL, United Kingdom, and [b]ISIS, Rutherford Appleton Laboratory, Chilton, Didcot, Oxfordshire OX11 0QX, United Kingdom. *Correspondence e-mail: m.senn@warwick.ac.uk

A novel symmetry-adapted pair distribution function analysis (SAPA) method for extracting information on local distortions from pair distribution function data is introduced. The implementation of SAPA is demonstrated in the *TOPAS-Academic* software using the freely available online software *ISODISTORT*, and scripts for converting the output from *ISODISTORT* to a SAPA input file for *TOPAS* are provided. Finally, two examples are provided to show how SAPA can evaluate the nature of both dynamic distortions in ScF_3 and the distortions which act as an order parameter for the phase transitions in $BaTiO_3$.

1. Introduction

The technique of total scattering, by which one obtains a pair distribution function (PDF), is an increasingly powerful tool used to analyse the local structure of a variety of materials (Keen, 2020). The first quantitative measurements using this technique were made in the 1930s, when experiments were performed on liquid mercury (Debye & Menke, 1930) and sodium (Tarasov & Warren, 1936). Since this early work, the technique has seen a wide range of uses, such as comparing crystalline and amorphous structures of the same materials (Biscoe & Warren, 1938; Hultgren *et al.*, 1935; Warren *et al.*, 1936; Peterson *et al.*, 2013), modelling crystalline disorder (Keen *et al.*, 2005; Senn *et al.*, 2016), and studying the dynamics of more ordered materials (Bird *et al.*, 2020; Conterio *et al.*, 2008; Goodwin *et al.*, 2009). The focus of this work is to present a novel approach for the latter. Whilst there are more established methods of investigating phonons in crystalline materials, chiefly inelastic neutron scattering, these methods require single crystals and are often quite time consuming. In comparison, total scattering experiments are relatively easy to perform, only require a powder sample and are more time efficient. There are now even laboratory-based instruments that can collect X-ray total scattering data, making it a more readily available technique (Confalonieri *et al.*, 2015; Thomae *et al.*, 2019; Irving *et al.*, 2021).

The PDF of a material is obtained via a Fourier transform of the observed scattering function $S(Q)$ (Keen, 2020). The scattering function contains structural and lattice dynamics information, and therefore this information should also be present in the PDF. Indeed, it has been shown that experimental PDF peak widths correlate well with mean-square displacements obtained from lattice vibration models (Jeong *et al.*, 1999, 2003).
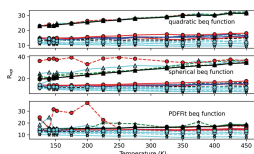
Various methods have been used to try and retrieve the dynamic information from the PDF. The first method used standard phonon models of the studied materials. By comparing their associated PDFs with those observed experimentally, reasonably accurate dispersion curves could be reproduced for some fairly simple systems such as face-centred cubic rhodium (Dimitrov *et al.*, 1999), but the process became increasingly inaccurate when more parameters were required in the phonon model (Reichardt & Pintschovius, 2001; Graf *et al.*, 2003). The second method used the reverse Monte Carlo (RMC) method to produce a large number of atomistic configurations, which can be thought of as snapshots of the material at different times since they are all consistent with the input PDF (Goodwin *et al.*, 2004, 2005, 2009; Conterio *et al.*, 2008). These configurations can then be used to construct a phonon dispersion curve *via* methods developed for molecular dynamics simulations. The same authors have used a similar technique to construct spin-wave dispersion curves (Goodwin *et al.*, 2007). This method has been shown to produce reliable information for low-frequency modes but fails to reproduce higher-frequency features, such as longitudinal-optical/transverse-optical mode splitting. This is to be expected, since the Bose factor in the phonon cross section, which approaches $1/\omega^2$ at higher temperatures, means that the PDF is much more sensitive to low-frequency information. A later paper used a similar method to look at disorder in $BaTiO_3$ and $Bi_2Ti_2O_7$, but employed representational analysis rather than molecular dynamics methods to quantify the dynamics (Neilson & McQueen, 2015). Whilst these methods have their uses, they both have some downsides. They are both computationally intensive and require a lot of modelling to produce any results. In addition, the RMC method requires a more intensive setup process than the method presented here. The first method also requires preselection of a phonon model and hence an assumption of the nature of the local distortions, introducing bias into the analysis. As a result of this, there have been relatively few papers using either method.

The method presented here, symmetry-adapted PDF analysis (SAPA), involves expanding the possible degrees of freedom of the crystallographic unit cell up to a given super-cell size in terms of symmetry-adapted displacements of the zone centre and zone boundary irreducible representations (irreps) of the structure being studied, or a higher-symmetry parent structure. The collection of symmetry-breaking displacements transforming as the same irrep may be further decomposed into symmetry-adapted distortion modes by choosing a sensible basis that reflects the chemistry and crystallographic axes of the structure. The distortion modes have a 1:1 correspondence with phonon eigenvectors in the limit that only one set of atomic displacements transforms as the corresponding irrep. It is hence justifiable (in the harmonic approximation) to test distortions belonging to a given irrep against the data in turn. In cases where distortions from different Wyckoff sites transform as the same irrep, the character of the low-lying excitations can still be ascertained through refining the relative amplitudes of the individual

distortion modes simultaneously. This method does not aim to produce a dispersion curve from diffraction data; the goal is to determine which of the symmetry-adapted distortion modes are most responsible for local deviations from a parent or average structure. The method has been used successfully to study order–disorder-type phase transitions in $BaTiO_3$ (Senn *et al.*, 2016) and the dynamic distortions responsible for the large magnitude of negative thermal expansion in ScF_3 and $CaZrF_6$ (Bird *et al.*, 2020). The process itself is similar to one presented by Kerman *et al.* (2012) to determine the average structure of a distorted material, although the primary aim of the SAPA method is to determine how the local structure deviates from the average.

2. Method

The primary tool presented in this paper is a script to convert mode parameterizations generated by the *ISODISTORT* software (Campbell *et al.*, 2006) into pair distribution function refinement input files for the *TOPAS-Academic* software (Coelho *et al.*, 2015). This script groups the symmetry modes in the input file with respect to the irreducible representation they transform as, and allows these groups of modes to be turned on in refinements from the command line.

2.1. Software

This method uses the *TOPAS-Academic* software v6 (Coelho, 2018) with an additional set of macros and functions for use with pair distribution function refinements. These macros and functions are obtained by downloading the `pdf.inc` file from the GitHub repository of Chater (2017). A strength of the *TOPAS* software is that it is written in its own scripting language. This has allowed users from the scientific community to implement new methods, including symmetry-mode refinements (Lewis *et al.*, 2016). Additionally, the method it uses to refine PDF data is significantly faster than alternative programs (Coelho *et al.*, 2015), including the *PDFfit2* program (Farrow *et al.*, 2007), in which this symmetry-adapted PDF analysis method was initially implemented (Senn *et al.*, 2016). The online tool *ISODISTORT* (version 6.9.0, June 2021) was used to generate the mode parameterizations.

2.2. Generating mode parameterizations

An overview of the steps required to perform a symmetry-adapted PDF analysis is shown in Fig. 1. The first step in the process of performing this symmetry mode analysis is to identify the parent structure to be used. When analysing the dynamic distortions of a material that stays in the same phase over the temperature or pressure range of interest, that phase can be chosen as the parent structure. For example, when performing this analysis on the negative thermal expansion material ScF_3, which retains its cubic $Pm\bar{3}m$ structure down to very low temperatures, the $Pm\bar{3}m$ phase was chosen to perform the analysis. If however the material undergoes phase transitions, or stays in one phase but is a distorted version of a higher-symmetry parent structure, the undistorted parent
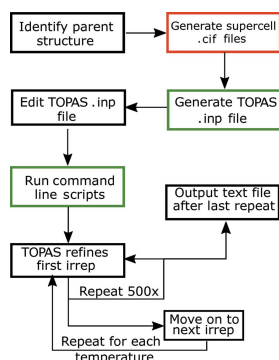
Figure 1
A diagram showing the processes to go through to use the expanded small box method. Steps in a red box use the online tool *ISODISTORT* and steps with a green box use the Python programming language.

structure would be a sensible choice. For example, to study a distorted perovskite, or a perovskite which undergoes a phase transition in the temperature range of interest, the aristotype perovskite structure could be used.

The next step is to decide the supercell size to expand up to. The modes that will be included and excluded when choosing the supercell must be considered; for example, a $3 \times 3 \times 3$ supercell would not include distortions with propagation vectors of [1/2 0 0], [1/2 1/2 0] or [1/2 1/2 1/2]. Another element of the analysis to keep in mind is that expanding the structure further increases the number of modes and therefore increases the time it takes to get results. For example, the $2 \times 2 \times 2$ supercell of ScF_3 contains 32 atoms and therefore has 96 distortion modes. Increasing the supercell to $3 \times 3 \times 3$ increases the number of atoms to 108 and the number of modes to 324. Furthermore, distortion modes corresponding to very low symmetry points of the Brillouin zone will not benefit from any symmetry constraints on their characters. In addition, their long-wavelength nature will mean that low-r regions of the PDF will not contain sufficient information to constrain them.

Once the previous two steps have been completed, the mode listing can be generated using the *ISODISTORT* program. Firstly, a .cif file of the chosen parent structure must be imported, taking careful note of the setting and positions of the atoms used in this structure since they can have an effect on the assignment of irrep labels in the analysis. The *ISODISTORT* option 'Method 3: Search over arbitrary k points for specified space group and lattice' is then used. In order to include all possible distortion modes, the user should select $P1$ space-group symmetry and then

input the supercell size by changing the diagonal elements in the representative basis: *e.g* if choosing a $2 \times 2 \times 2$ supercell, $a' = 2a + 0b + 0c$, $b' = 0a + 2b + 0c$ and $c' = 0a + 0b + 2c$. Clicking 'OK' here opens a new window prompting the user to finish selecting the distortion mode. There should only be one option here, so the user should just click 'OK'. The next page will have a list of all the distortion modes grouped by irrep and a few options at the top. On choosing the 'CIF file' option and again clicking 'OK', the user will be prompted to save a .cif file – it is recommended not to include spaces or special characters in the file name, as this could cause later steps to not work.

The majority of the *TOPAS* input file can be written using information from the CIF produced with *ISODISTORT* in the previous step. To make this easier, we have written a script (available on an online repository; Bird & Senn, 2021) in the Python programming language which can read a CIF and convert it to a Python class. The data names defined in the CIF are accessible as class variables in Python. A method of this class, write_inp, uses this to output a *TOPAS* .inp file. A snippet of code demonstrating how to use this is shown in Fig. 2(a). In this section, we will go through the contents of the .inp file and detail any information that the user has to input. Another method of this class, irrep_list, can be used to produce a list of irreps in the .cif file, which is useful when running the .inp file. Note that this script will not work without the string #End at the end of the CIF. Files generated using *ISODISTORT* should have this already included, but those generated from other sources may not. In addition, the user should ensure that there is no white space at the start of each line.

The first thing the user must decide is the number of cycles that *TOPAS* will perform for each irrep. At the start of each cycle, the mode amplitudes for the defined irrep are randomized within a set range *via* the continue_after_convergence and val_on_continue commands. For irreps that have a higher dimensionality, more cycles are needed to ensure that the global minimum is found for that irrep, but this has the trade-off of increasing the time needed for a full set of refinements. A good starting point is to choose

```
(a)
import read_isodisplace_cif as r

structure = iso_cif_file("iso_cif_name.cif")
structure.write_inp()
(b)
import os

irreps = [...]
temps = [...]

for temp in temps:
  for i in irreps:
    os.system(" tc batch_modes.inp \" macro IRREP {%s} macro VAR {%s} #define %s \" "%(i,temp,i))
```

Figure 2
A snippet of Python code showing (*a*) how to use the write_inp method of the read_isodisplace_cif script to generate a *TOPAS* input file and (*b*) how to use the Python os library to run the generated file on the command line. Here, irreps and temps are user-defined lists.

500 cycles. We found that, on a standard single-core laptop computer, 500 repeat refinements of a single irrep tended to take about 20 min. The command to specify a fixed number of cycles is shown in the seventh line of Fig. 3. The second part of Fig. 3 is the file input macro. This can be used when the data files are in a consistent format. The macro itself should reflect the user's directory structure. The macro is called in the `xdd` line of the input file, and the `VAR` keyword is updated with a user-defined variable in the command line, which is explained in more detail in the next section. To make things easier, it is recommended to rename the data files to reflect the variable(s) that are changing with each PDF. For example, the files for the ScF_3 example below reflect the temperature that the data were collected at.

Following this, the user must input some functions to take care of any instrumental and processing factors in the PDF. All of these functions, and others necessary for this method, can be found at the cited GitHub repository (Chater, 2017). The first instrumental function is to model the damping effect of the reciprocal-space peak width, dQ. If the Bragg peaks can be modelled well with a Gaussian peak shape, then the function `dQ_damping` should be used. If the Bragg peaks have a significant Lorentzian component, then this can be modelled using the `dQ_lor_damping` function. If the Bragg peak width increases as a function of Q, which results in r-dependent broadening in the PDF, the `convolute_alpha` function can be used. This does significantly slow down refinements however, and including it typically does not affect the qualitative output for this method. All three of these parameters (dQ, the Lorentzian contribution to the Bragg peak shape and the linear peak width scaling) can be refined from the Bragg data of a standard using the peak shape function `pkshape_dQ_alpha`. The termination ripples in the PDF originating from a finite Q_{max} can be accounted for using the `convolute_Qmax_Sinc` function. This function fails at low radii, so it is recommended to limit the refinement range to above 1 Å. If a Lorch or Soper–Lorch function has been used to mitigate against termination ripples prior to the

```
r_wp 0.0 r_exp 0.0 r_p 0.0
r_wp_dash 0.0 r_exp_dash 0.0
weighted_Durbin_Watson 0.0 gof 0.0
iters 10000000
chi2_convergence_criteria 0.001
continue_after_convergence
prm dummy 0.00000 val_on_continue = If(Cycle == xxx, Get(iters) = 0, 0);

macro file_in_(n)
{
C:\Documents\Files\##n##K_pdf.xye
}

xdd file_in_(VAR)
```

Figure 3
The start of a *TOPAS* input file for analysing a PDF via symmetry-mode analysis. `xxx` should be replaced with the desired number of repeat refinements for each irrep. In the present work, `xxx` = 500 has been employed to ensure that the global minimum has been reached. In addition, the directory here is taken to be the directory in which the data are stored. The string `##n##` is replaced by the command line macro according to the naming convention of the variable-temperature data sets.

Fourier transform of $S(Q)$, then the `convolute_Lorch` or `convolute_SoperLorch` function should be used instead. The usage of these functions is detailed fully in the `pdf.inc` file. All of the values set at this stage of the input file should be fixed when running the file.

The major choice the user has to make when creating the input file is the PDF peak shape function. In Bragg scattering, the thermal motion is assumed to be completely uncorrelated, so a Gaussian function that ignores any correlated displacements is a reasonable approximation, and a constant value B_{iso} can be used to account for the thermal motion of an atom. In PDFs, this is not a good approximation, since atoms which are closer together will tend to have highly correlated motion, resulting in a narrower peak width at low radii. This kind of correlated motion is precisely what we aim to extract with this symmetry-motivated approach for analysing PDFs. To account for this, the single value B_{iso} (`beq` in *TOPAS*) is replaced with a radius-dependent function. There are a variety of options to choose from for this function, all of which are defined in the `pdf.inc` file. The simplest is the `beq_rcut` function, which is a step function between two constant values, increasing from the smaller to the larger at some defined cut-off radius. Another simple function, `beq_spherical`, uses the PDF of a sphere to scale between a value at low radius and another at a higher radius. The `beq_rcut_rlo_spherical`, `beq_rlo_spherical` and `beq_rcut_spherical` functions use a combination of cut-offs and spherical scaling. The function that is included by default by the `write_inp` method is `beq_r_r2`, which is a quadratic function of the radius, r. We find that the coefficient of r^2 refines to negligible values, so typically fix it at zero. It is advisable to choose a simple peak width function – the symmetry-adapted displacements being refined will account for some of the peak width, and introducing more parameters can lead to undesirable correlations. The *PDFfit* peak shape function is also implemented. However, we have found that refinements are often unstable when using it and, in particular, refinements with a constrained order parameter direction often fail to find the global minimum.

The last thing in the input file is the file output macro. Similarly to the file input macro, the `VAR` and `IRREP` keywords are replaced in the command line. This function, used in conjunction with the `out_prm_vals_on_convergence` command, produces an output file for each irrep and each temperature or pressure which has a record of the final values for each cycle for all refined variables in the input file.

2.3. Running the input file

The input file is intended for use with the *TOPAS* command line executable, which requires that the working directory is the directory where *TOPAS* is installed. The input file uses `#ifdef` and `#ifndef` directives in conjunction with the `#define` directive, the last of which can be passed on the command line, to refine each irrep in sequence. While all the symmetry modes belonging to the irreps are defined in the input file, the user can choose which modes, grouped by irrep,

to activate. The *TOPAS* command line executable also has the ability to replace user-defined keywords in the input file with values passed on the command line. For example, writing `macro VAR {X}` on the command line will replace the keyword `VAR` with the value *X* wherever it is found in the input file. To use the input file, the user must define a list of temperatures or pressures to sequentially replace the `VAR` keyword with and a list of irreps to cycle through. Example scripts to execute the generated input file are included in the online repository (Bird & Senn, 2021) and a demonstration of how to run the input file is given in Fig. 2(*b*).

A successful execution of the input file will produce a series of output files. A separate output file is produced for each irrep and each temperature, containing the R_{wp} and the value of every refined parameter for each cycle in the order they were performed. These files are delimited by white space and can be analysed by standard data analysis software packages such as *R* (https://www.r-project.org/) or the *pandas* library for Python (https://pandas.pydata.org/).

3. Examples

The files for both examples, including example input files and Python scripts to execute the analysis, are included in the online repository (Bird & Senn, 2021).

3.1. Scandium trifluoride

Scandium trifluoride (ScF_3) is a material that exhibits isotropic negative thermal expansion (NTE) over a wide temperature range and is typically used to demonstrate the rigid unit mode (RUM) model of NTE. It is formed of corner-sharing ScF_6 octahedra and remains in a $Pm\bar{3}m$ cubic structure as the temperature is lowered to 0 K. Owing to its high-symmetry structure, lack of phase transitions and interesting dynamics, it makes a good test case on which to apply this symmetry-adapted PDF analysis. Since ScF_3 remains in the same space group, the choice of the $Pm\bar{3}m$ phase as the parent structure for the analysis is trivial – the only choice to make is the structure setting, which determines the irrep labels. For this work, the setting with Sc at 1*b* (1/2, 1/2, 1/2) and F at 3*c* (0, 1/2, 1/2) was used. A $2 \times 2 \times 2$ supercell was chosen for the unit-cell expansion, since this allows phonon modes with propagation vectors **k** = [0 0 0], [1/2 0 0], [1/2 1/2 0] and [1/2 1/2 1/2] to be modelled and distortions with these **k** vectors are very common in perovskite and perovskite-adjacent compounds like ScF_3. This study uses X-ray PDF data generated from total scattering data collected at the P02.1 beamline at PETRA III, DESY, Germany. $Q_{max} = 21$ Å^{-1} was used with d$Q = 0.08$ Å^{-1}. Complete experimental details can be found in our previously published work (Bird *et al.*, 2020). An example input file is included in the online repository (Bird & Senn, 2021). The input file contains definitions for modes belonging to all the high-symmetry irreps of the $2 \times 2 \times 2$ supercell. However, use of the `#ifdef` and `#ifndef` directives in conjunction with the `#define` directive

allows the modes belonging to a single irrep to be refined with all the others 'turned off'.

As mentioned in Section 2, an important aspect of applying this symmetry-adapted PDF analysis is the choice of PDF peak width function. We compare results from three of these functions in Fig. 4 [`beq_r_r2`, `beq_spherical` and `beq_PDFfit2`, the *TOPAS* implementation of the *PDFgui* (Farrow *et al.*, 2007) peak shape function]. The three functions produce quite similar results – the 'ranking' of the irreps at each temperature is reasonably consistent. The function that performs the best for this compound is `beq_r_r2` – the trend for each irrep is quite smooth and there are none of the erratic jumps in R_w that can be seen in both of the other functions. Since in this case the coefficient of r^2 was fixed at zero, this function also has only two parameters per site, which is the same as the *PDFfit* function used and the spherical function. We now go on to analyse the results of this method.

The distortions used in this analysis can be sorted into three general types: rigid unit modes, which consist of coherent rotations of the octahedra; semi-rigid 'scissoring' modes, where there is a scissoring of some of the Sc−F bond angles within the octahedra; and bond-stretching modes, where some M−F bond lengths change. Most irreps only have one of these types of distortion associated with them, although some have two. In Fig. 4, the irreps are clearly separated into two 'bands', one fitting well and one fitting poorly. The band of poorly fitting irreps all have distortions with a bond-stretching character, which are typically the highest-energy modes, meaning they have little influence on the local structure. The irreps in the other band all have at least one distortion associated with them that is of either rigid or semi-rigid unit mode character. There are four zone-boundary irreps that consistently have the lowest weighted *R* factors and have the greatest ampli-tudes: X_5^+, X_5^-, M_5^+ and M_5^-. All four of these have one
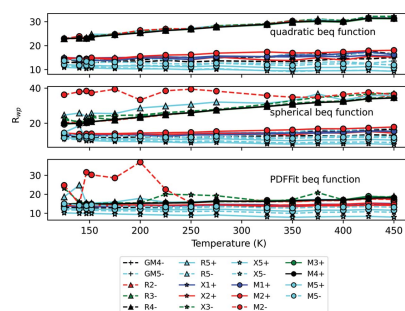

Figure 4
A plot of the best R_{wp} of all irreps against temperature for three different PDF peak shape functions used during refinement against ScF_3 X-ray PDF data. The data points are made to differentiate between irrep labels: the marker designates the *k* point (a circle for M, a triangle for R, a star for X and a plus for Γ); the colour designates the number in the subscript (blue for 1, red for 2, green for 3, black for 4 and cyan for 5); and the linestyle designates the sign of the superscript (solid for +, dashed for −).

distortion associated with them that is of scissoring-mode character. All four modes have an amplitude (normalized to the supercell) between 0.9 and 1.0 Å and vary linearly with temperature to values between 1.30 and 1.45 Å at 450 K. There are a few possible conclusions one could make from this information, which would need further analysis to explore.

By performing competitive two-phase refinements between scissoring modes and RUMs, we found that scissoring modes dominate the motion of the fluorine ions (Bird *et al.*, 2020). This could mean that the negative thermal expansion in ScF_3 arises purely from these kind of motions, and Wendt *et al.* (2019) have even argued that the fluorine ion motions are predominately uncorrelated. Alternatively, it could mean that these scissoring modes act in conjunction with the RUMs to produce the observed NTE. A low energy cost for scissoring-type deformations of the octahedra would increase the proportion of quasi-RUMs, modes of mixed RUM and octahedral deformation character, with negative Grüneisen parameters. Both of these possibilities are analysed further in our (Bird *et al.*, 2020) and others' recent work (Dove, 2019; Dove *et al.*, 2020).

3.2. Barium titanate

Barium titanate ($BaTiO_3$) is one of the most well known ferroelectric materials. The Curie temperature (T_C) for $BaTiO_3$ is 393 K, above which the material has the archetypal cubic perovskite structure. Below T_C, the structure is distorted into a $P4mm$ tetragonal phase and, because of this, the cubic-to-tetragonal distortion was initially discussed in terms of displacive phase transitions (Cochran, 1959). Two lower-temperature phases, an orthorhombic $Amm2$ phase and a rhombohedral $R3m$ phase, were discovered, with transition temperatures of 278 and 183 K, respectively (Kay & Vousden, 1949; Rhodes, 1949). The existence of these phases is inconsistent with the picture of second-order displacive phase transitions. This anomaly, in conjunction with the observation of diffuse scattering in all but the rhombohedral phase (Comes *et al.*, 1968), led to the development of an order–disorder model for $BaTiO_3$ (Comès *et al.*, 1970). In this example, we aim to show that this method is sensitive to the nature of the local displacements in $BaTiO_3$.

We generate the distortion modes using the high-symmetry $Pm\bar{3}m$ structure for $BaTiO_3$, with the setting Ba 1*a* (0, 0, 0); Ti 1*b* (1/2, 1/2, 1/2); O 3*c* (0, 1/2, 1/2). The `beq_r_r2` function is used to account for correlation of displacements. The PDFs used for this study were generated from total scattering data collected on the GEM instrument at the ISIS neutron and muon source. $Q_{max} = 40$ Å^{-1} was used with d$Q = 0.033$ Å^{-1}. Further experimental details can be found in our previous publication on the subject (Senn *et al.*, 2016). An example input file is included in the online repository (Bird & Senn, 2021). Since the structure undergoes phase transitions, we give different constraints for the lattice parameters and angles depending on the average structure. For example, when the structure is cubic, we restrict all three lattice parameters to be equal, whereas they are allowed to be different in the orthorhombic structure. We use a different method to view the

initial results than for ScF_3, where we simply viewed the best fit for each irrep at each temperature. For $BaTiO_3$ we are more interested in the primary order parameter. Therefore, we calculate the mode amplitude for each refinement and weight it according to a Boltzmann distribution $\exp[(R_{w\,global} - R_w)/\sigma]$, where R_w is the weighted phase R factor for that refinement, $R_{w\,global}$ is the lowest value for R_w across all irreps for each temperature and σ is the value of a meaningful difference in R_w, taken to be 0.8%. We then sum this value for each irrep and obtain what we term a Boltzmann weighted mode amplitude (BWMA). These BWMAs are plotted in Fig. 5. The mode amplitudes themselves are calculated for each refinement by first dividing the amplitude of each mode that enters into the irrep by the normalization factor (given in the *ISODISTORT* CIF), putting it on an absolute, rather than fractional, scale. Subsequently, the square root of the sum of squares of the individual normalized mode amplitudes is taken as the overall mode amplitude for the irrep.

We can classify the behaviour of the BWMAs into three different groups: the first has low values in the cubic phase with larger values at lower temperatures; the second has small values in the cubic phase which drop down to near zero at lower temperatures; and the third has near-zero values for all temperatures. We can disregard all those in the third group, as they clearly do not have a significant contribution to the local symmetry-breaking distortions in $BaTiO_3$. There is only one irrep in the first group, the Γ_4^- irrep. The modes belonging to this irrep are displacements of the Ti and O atoms (note that *ISODISTORT* additionally includes displacements of the Ba atoms in this irrep, but we fix these at zero to avoid a floating origin of the unit cell) and are clearly the order parameters relevant for the ferroelectric phase transitions. The second group of irreps have modes which are soft in the cubic phase, since they have similar BWMAs to the primary order
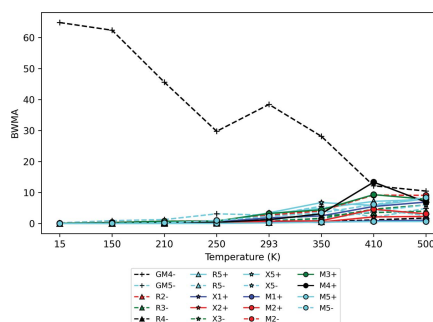

Figure 5
A plot showing the BWMAs for $BaTiO_3$. The data points are made to differentiate between irrep labels: the marker designates the *k* point (a circle for M, a triangle for R, a star for X and a plus for Γ); the colour designates the number in the subscript (blue for 1, red for 2, green for 3, black for 4 and cyan for 5); and the linestyle designates the sign of the superscript (solid for +, dashed for −).

parameter in that phase. The two irreps with the greatest BWMAs in the cubic phase are X_5^+ and M_2^-, which are known to be soft eigenvectors of the system and are on the same line in the phonon dispersion curves as Γ_4^-. An interesting comparison between the results for $BaTiO_3$ and ScF_3 can be made here – both analyses pull out X_5^+ as a mode of interest, but the overall character of the distortion is different in each case. For ScF_3, the distortion is mostly of the scissoring-mode character, with insignificant contributions from the other modes. In $BaTiO_3$, the main distortion is the anti-ferroelectric displacements.

We now move on to analyse the underlying symmetry of the order parameter Γ_4^-. Each mode belonging to Γ_4^- has three branches, and hence has a general order parameter direction (OPD) (a, b, c). This general distortion would reduce the symmetry of the structure to $P1$. A more constrained OPD would break fewer symmetry operations. The relevant order parameters for Γ_4^- are $(a, 0, 0)$, resulting in a $P4mm$ space group, $(a, a, 0)$ ($Amm2$), (a, a, a) ($R3m$), $(a, b, 0)$ (Pm) and (a, a, b) (Cm). In the tetragonal and orthorhombic phases, the atoms tend to have an (a, a, b) OPD. This initially seems to reveal an underlying monoclinic symmetry in the displacements. However, this may also be viewed as a local rhombohedral distortion split by the global lattice distortion. This is consistent with the order–disorder model of the phase transitions in $BaTiO_3$.

4. Summary

In conclusion, we have demonstrated in detail how to perform the symmetry-adapted pair distribution function analysis technique with the *TOPAS-Academic* software v6. We have also provided two applications of this technique, with example input files so the reader can reproduce the above results as an introduction the technique. It has been demonstrated to be a useful technique to gain insight into both dynamic and static distortions in perovskite and perovskite-related materials. It is envisaged that use of this approach in conjunction with the freely available scripts (provided via GitHub) will enable other researchers to robustly and routinely evaluate lattice dynamics and local distortions of other solid-state materials.

References

Bird, T. A. & Senn, M. S. (2021). *SAPA*, https://github.com/tabmapi/sapa.
Bird, T. A., Woodland-Scott, J., Hu, L., Wharmby, M. T., Chen, J., Goodwin, A. L. & Senn, M. S. (2020). *Phys. Rev. B*, **101**, 064306.
Biscoe, J. & Warren, B. E. (1938). *J. Am. Ceram. Soc.* **21**, 287–293.
Campbell, B. J., Stokes, H. T., Tanner, D. E. & Hatch, D. M. (2006). *J. Appl. Cryst.* **39**, 607–614.
Chater, P. A. (2017). *Macros and Menus for Use With TOPAS*, https://github.com/pachater/topas.
Cochran, W. (1959). *Phys. Rev. Lett.* **3**, 412–414.
Coelho, A. A. (2018). *J. Appl. Cryst.* **51**, 210–218.
Coelho, A. A., Chater, P. A. & Kern, A. (2015). *J. Appl. Cryst.* **48**, 869–875.
Comes, R., Lambert, M. & Guinier, A. (1968). *Solid State Commun.* **6**, 715–719.
Comès, R., Lambert, M. & Guinier, A. (1970). *Acta Cryst.* A**26**, 244–254.
Confalonieri, G., Dapiaggi, M., Sommariva, M., Gateshki, M., Fitch, A. N. & Bernasconi, A. (2015). *Powder Diffr.* **30**, S65–S69.
Conterio, M. J., Goodwin, A. L., Tucker, M. G., Keen, D. A., Dove, M. T., Peters, L. & Evans, J. S. (2008). *J. Phys. Condens. Matter*, **20**, 255225.
Debye, P. & Menke, H. (1930). *Phys. Z.* **31**, 797–798.
Dimitrov, D. A., Louca, D. & Röder, H. (1999). *Phys. Rev. B*, **60**, 6204–6207.
Dove, M. T. (2019). *Phil. Trans. R. Soc. A*. **377**, 20180222.
Dove, M. T., Du, J., Wei, Z., Keen, D. A., Tucker, M. G. & Phillips, A. E. (2020). *Phys. Rev. B*, **102**, 094105.
Farrow, C. L., Juhas, P., Liu, J. W., Bryndin, D., Božin, E. S., Bloch, J., Proffen, T. & Billinge, S. J. L. (2007). *J. Phys. Condens. Matter*, **19**, 335219.
Goodwin, A. L., Dove, M. T., Chippindale, A. M., Hibble, S. J., Pohl, A. H. & Hannon, A. C. (2009). *Phys. Rev. B*, **80**, 054101.
Goodwin, A. L., Dove, M. T., Tucker, M. G. & Keen, D. A. (2007). *Phys. Rev. B*, **75**, 075423.
Goodwin, A. L., Tucker, M. G., Cope, E. R., Dove, M. T. & Keen, D. A. (2005). *Phys. Rev. B*, **72**, 214304.
Goodwin, A., Tucker, M., Dove, M. & Keen, D. (2004). *Phys. Rev. Lett.* **93**, 075502.
Graf, M., Jeong, I. K., Starr, D. & Heffner, H. (2003). *Phys. Rev. B*, **68**, 064305.
Hultgren, R., Gingrich, N. S. & Warren, B. E. (1935). *J. Chem. Phys.* **3**, 351–355.
Irving, D. J., Keen, D. A. & Light, M. E. (2021). *Rev. Sci. Instrum.* **92**, 043107.
Jeong, I. K., Heffner, R. H., Graf, M. J. & Billinge, S. J. (2003). *Phys. Rev. B*, **67**, 104301.
Jeong, I. K., Proffen, T., Mohiuddin-Jacobs, F. & Billinge, S. J. (1999). *J. Phys. Chem. A*, **103**, 921–924.
Kay, H. & Vousden, P. (1949). *London Edinb. Dubl. Philos. Mag. J. Sci.* **40**, 1019–1040.
Keen, D. A. (2020). *Crystallogr. Rev.* **26**(3), 141–199.
Keen, D. A., Tucker, M. G. & Dove, M. T. (2005). *J. Phys. Condens. Matter*, **17**, S15–S22.
Kerman, S., Campbell, B. J., Satyavarapu, K. K., Stokes, H. T., Perselli, F. & Evans, J. S. O. (2012). *Acta Cryst.* A**68**, 222–234.
Lewis, J. W., Payne, J. L., Evans, I. R., Stokes, H. T., Campbell, B. J. & Evans, J. S. (2016). *J. Am. Chem. Soc.* **138**, 8031–8042.
Neilson, J. R. & McQueen, T. M. (2015). *J. Appl. Cryst.* **48**, 1560–1572.
Peterson, J., TenCate, J., Proffen, Th., Darling, T., Nakotte, H. & Page, K. (2013). *J. Appl. Cryst.* **46**, 332–336.
Reichardt, W. & Pintschovius, L. (2001). *Phys. Rev. B*, **63**, 174302.
Rhodes, R. G. (1949). *Acta Cryst.* **2**, 417–419.
Senn, M. S., Keen, D. A., Lucas, T. C., Hriljac, J. A. & Goodwin, A. L. (2016). *Phys. Rev. Lett.* **116**, 207602.
Tarasov, L. P. & Warren, B. E. (1936). *J. Chem. Phys.* **4**, 236–238.
Thomae, S. L., Prinz, N., Hartmann, T., Teck, M., Correll, S. & Zobel, M. (2019). *Rev. Sci. Instrum.* **90**, 043905.
Warren, B. E., Krutter, H. & Morningstar, O. (1936). *J. Am. Ceram. Soc.* **19**, 202–206.
Wendt, D., Bozin, E., Neuefeind, J., Page, K., Ku, W., Wang, L., Fultz, B., Tkachenko, A. V. & Zaliznyak, I. A. (2019). *Sci. Adv.* **5**, eaay2748.

Chapter 3

Anharmonicity and Scissoring Modes in the Negative Thermal Expansion Materials ScF_3 and $CaZrF_6$

Anharmonicity and scissoring modes in the negative thermal expansion materials ScF$_3$ and CaZrF$_6$

T. A. Bird,[1] J. Woodland-Scott,[2] L. Hu,[3] M. T. Wharmby ⦿,[4] J. Chen,[3] A. L. Goodwin,[2] and M. S. Senn ⦿[1,*]

[1]*Department of Chemistry, University of Warwick, Gibbet Hill, Coventry CV4 7AL, United Kingdom*
[2]*Department of Chemistry, University of Oxford, Inorganic Chemistry Laboratory, South Parks Road, Oxford OX1 3QR, United Kingdom*
[3]*Department of Physical Chemistry, University of Science and Technology Beijing, Beijing 100083, China*
[4]*Deutsches Elektronen-Synchrotron (DESY), Notkestrasse 85, 22607 Hamburg, Germany*

We use a symmetry-motivated approach to analyzing x-ray pair distribution functions to study the mechanism of negative thermal expansion in two ReO$_3$-like compounds: ScF$_3$ and CaZrF$_6$. Both average and local structures suggest that it is the flexibility of M-F-M linkages (M = Ca, Zr, Sc) due to dynamic rigid and semirigid "scissoring" modes that facilitates the observed negative thermal expansion (NTE) behavior. The amplitudes of these dynamic distortions are greater for CaZrF$_6$ than for ScF$_3$, which corresponds well with the larger magnitude of the thermal expansion reported in the literature for the former. We show that this flexibility is enhanced in CaZrF$_6$ due to the rocksalt ordering mixing the characters of two of these scissoring modes. Additionally, we show that in ScF$_3$ anharmonic coupling between the modes responsible for the structural flexibility and the rigid unit modes contributes to the unusually high NTE behavior in this material.

I. INTRODUCTION

Research into materials that contract upon heating, termed negative thermal expansion (NTE) materials, has been steadily increasing over the past 30 years. The significance of the phenomenon was first underlined by Evans *et al.* in 1996 [1] by linking the large, isotropic NTE of ZrW$_2$O$_8$ to the crystal structure of the material, opening up the field to synthesis of new compounds. Since then, this field has been expanded to a wider range of materials, including simple oxides (such as Cu$_2$O [2] and ReO$_3$ [3,4]) and metal-organic frameworks [5,6].

The rigid unit mode (RUM) model is a common way to explain the origin of NTE [7]. Materials made from rigid polyhedra have a significant energy barrier to distortions of the polyhedra, but a low barrier to collective dynamics such as rotations. These modes are often low in energy and so make a significant contribution to the coefficient of thermal expansion, and they can lead to NTE via the tension effect: if two linked bonds are straight or nearly straight and stretching the bonds would take a large amount of energy, a transverse displacement of the central atom would pull the two other atoms closer together, resulting in a local decrease in volume, the magnitude of which would increase when the temperature is raised [8]. ReO$_3$, a material made from corner-sharing ReO$_6$ octahedra (and hence can be thought of as an A-site-deficient perovskite), is commonly used to illustrate this model due

to the complexity of the motion in more typical NTE materials such as ZrW$_2$O$_8$. The octahedra in this material are expected to dynamically rotate in an out-of-phase manner with respect to their neighboring units about their average positions, resulting in a contraction of the structure while the material remains, on average, cubic [3]. Two compounds similar to ReO$_3$ are studied herein: the isostructural ScF$_3$ and the A-site-deficient double perovskite CaZrF$_6$. Metal trifluorides adopting the ReO$_3$ structure typically undergo a transition from the $Pm\bar{3}m$ cubic structure to a rhombohedral phase ($R\bar{3}c$) upon cooling, via long-range ordering of the MF$_6$ octahedra (a$^-$a$^-$a$^-$ in Glazer notation). The dynamic motion of these tilts was expected to be the mechanism for NTE in ScF$_3$ [9] supported by the fact that a phase transition to the rhombohedral tilt phase is observed under hydrostatic pressure of 0.7 GPa at ambient temperature [9,10] and in the related material CoZrF$_6$, whose high-temperature phase is isostructural to CaZrF$_6$ [11]. NTE is observed at a range of temperatures above the phase transition, but below it, once the phonon mode associated with the RUM has been "frozen in," strong positive thermal expansion is observed. Previous studies of these materials have shown large displacements of the fluoride ions perpendicular to the M-F-M bonds (M = Sc, Ca, Zr) [12,13], consistent with a polyhedral rocking mechanism for NTE. Other studies have challenged the RUM model, concluding that only certain bonds were rigid [14,15], rather than entire polyhedra, and that bond bending could be a contributor to NTE [16,17].

Several studies were performed recently to try and ascertain the origin of NTE in these materials. X-ray pair distribution function (PDF) analysis of two materials in the cubic MZrF$_6$ (M = Ca, Ni) series has shown that differing degrees of flexibility in M-F linkages results in isostructural materials having very different thermal expansion properties [18]. Lattice dynamics calculations of ScF$_3$ performed by Li *et al.*

---

*m.senn@warwick.ac.uk

[19] showed mostly soft lattice modes that distorted the ScF$_6$ octahedra; however, a $3 \times 3 \times 3$ grid of unit cells was chosen, which excludes the zone-boundary wave vectors which the RUMs are confined to. Molecular dynamics simulations on the general ReO$_3$ structure [20], with variable interaction strengths, suggest a degree of flexibility in the octahedra enhances NTE. Another conclusion from these simulations was that a weaker anion-anion nearest-neighbor interaction enhances NTE, which is supported experimentally by the greater magnitude of NTE in ScF$_3$ compared to ReO$_3$. There is experimental evidence from Raman spectra and inelastic neutron scattering that the large NTE in these materials cannot be accurately predicted with the quasiharmonic approximation [15,19], so subsequently lattice dynamics calculations were done to elucidate the connection between NTE and phonon anharmonicity since the relatively simple structure compared to other NTE materials allows for a more detailed analysis. These calculations show that cubic [21] and quartic [13,19] anharmonicity contribute significantly to the temperature dependence of the thermal expansion coefficient. Other simulations have shown that modes with quartic potential can have an enhanced NTE compared to a single-well potential [22].

ABO$_3$ perovskites exhibit a wide range of octahedral tilt phase transitions, as classified by Glazer [23], yet do not generally display phonon-driven NTE. However, we have recently demonstrated how, by using a symmetry-motivated approach to analyzing PDF data, we can gain extra information on disorder and dynamics [24]. Our study on BaTiO$_3$ showed that this method is very sensitive to soft phonon modes of RUM-like character. Here, we use this method to probe the character of the low-lying thermal excitations in the title compounds, where the amplitudes of such vibrations are believed to be very large.

II. EXPERIMENTAL DETAILS AND DATA ANALYSIS

Scandium trifluoride was used as supplied by Strem Chemicals. Synchrotron radiation x-ray total scattering experiments were conducted at the synchrotron facility PETRA III (beamline P02.1 [25]) at DESY, Hamburg. A wavelength $\lambda = 0.2070$ Å was used to collect data. Data were collected at temperatures of 125, 140, 147, and 152 K and at intervals of 25 K from 175 to 450 K. The obtained two-dimensional images were masked and radially integrated using the DAWN [26] software. $G(r)$ and $D(r)$ functions were computed using GUDRUNX [27] using $Q_{\max} = 21$ Å^{-1}. GUDRUNX was also used to perform background subtraction and sample absorption corrections.

CaZrF$_6$ was that prepared via a standard solid-state synthesis methods in Ref. [18]. The total scattering data were collected at 11-1D-C APS, Argonne National Laboratory, using a wavelength $\lambda = 0.11798$ Å between 25 and 400 K. The PDFs were computed using PDFGETX2 [28], which was also used for background subtraction and sample absorption corrections. $Q_{\max} = 28$ Å^{-1} was used for the analysis presented below.

A. Pair distribution function analysis

Some form of modeling is usually required to extract information of interest, such as local distortions of atoms away

from their high-symmetry positions, from pair distribution functions. The method presented here involves expanding the possible degrees of freedom in terms of symmetry-adapted displacements of the zone center and zone boundary irreducible representations (irreps) of the $Pm\bar{3}m$ A-site-deficient perovskite structure. For this analysis we use a parent $Pm\bar{3}m$ perovskite with the A site at the origin. Symmetry-breaking displacements transforming as the same irrep can be further decomposed into symmetry-adapted distortion modes by choosing a sensible basis that reflects the chemistry and crystallographic axes of the structure. The distortion modes have a 1:1 correspondence with phonon eigenvectors in the limit that only one set of atomic displacements transforms as the corresponding irrep. In cases where distortions from different Wyckoff sites transform as the same irrep, the character of the low-lying excitations can still be ascertained through refining the relative amplitudes of the individual distortion modes. An overview of the displacements that enter into each irrep was tabulated in a recent paper by Popuri *et al.* [29]. For both compounds, ISODISTORT [30] was used to generate a model parameterized in terms of symmetry-adapted displacements. A $2 \times 2 \times 2$ P1 supercell was used for ScF$_3$ since this allows phonon modes with propagation vectors $k = [0\ 0\ 0]$, $[1/2\ 0\ 0]$, $[1/2\ 1/2\ 0]$, and $[1/2\ 1/2\ 1/2]$ to be modeled. While this is only a small fraction of possible wave vectors, these are both the ones that PDF data have the greatest sensitivity to and for which our symmetry-motivated approach provides the greatest number of constraints. Furthermore, even if the exact wave vectors of the NTE-driving phonons are of a longer wavelength, we still expect the character of those phonons to be reflected in our results, which probe a shorter wavelength. To generate the parametrization of CaZrF$_6$, a $2 \times 2 \times 2$ supercell of disordered Ca$_{0.5}$Zr$_{0.5}$F$_3$ was used. The cations were then set to be fully ordered to generate the rocksalt ordered structure. In all refinements, the breathing mode about Ca/Zr (transforming as R_2^-) was refined, making this description equivalent to the published $Fm\bar{3}m$ structure [11]. The generated mode listings were output from ISODISTORT in CIF format and then converted to the INP format of the TOPAS ACADEMIC software, version 6 [31]. Modes transforming as the same irrep were tested simultaneously. An example of the best single-irrep refinement for each compound using this method is shown in Fig. 1. The results shown below (Fig. 2) were performed with a fitting range of 1 (ScF$_3$) or 1.7 (CaZrF$_6$) to 10 Å. The refinements were also done out to a higher radius; however, the results were broadly similar for these larger fitting ranges. A comparison between the results for 10 and 30 Å can be seen in the Supplemental Material (Fig. S3) [32].

The thermal parameters for each site were modeled with a simple quadratic, i.e., $b_i = b_{i,\text{low}} + ur + vr^2$, where u and v are constant across all sites for each refinement and $b_{i,\text{low}}$ is element dependent. While this does not capture the true physical behavior of the system, it was found to produce more robust fits to the data (stabler and fewer false minima) than other functional forms of b_i, with the results still being consistent with our analysis performed using different functional forms of b_i (see Fig. S2 in the Supplemental Material).

To get an unbiased view of how each irrep influences the local structure, the refinement for each irrep was initiated from
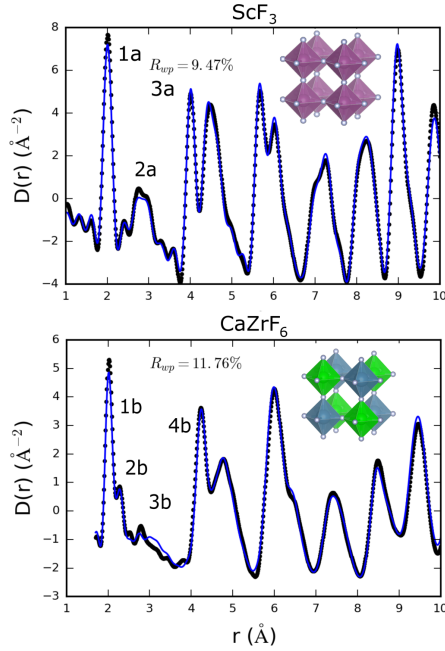
FIG. 1. Pair distribution functions for ScF_3 (top) and $CaZrF_6$ (bottom) at 400 K (black circles). A small box fit with the modes belonging to X_5^+ refined is shown for both compounds (blue lines), with the R_5^- mode additionally refined for $CaZrF_6$. Labeled peaks correspond to Sc-F (1a), F-F (2a, 3b), Sc-Sc (3a), Zr-F (1b), Ca-F (2b), and Ca-Zr (4b).

randomized starting values of the relevant mode amplitudes. When a minimum was reached, the refined parameters were stored, rerandomized, and a new cycle was initiated. This process was repeated until 25 000 iterations were reached (between 300 and 4000 refinements); this process was used to ensure a global minimum was reached for each mode. For refinements of atomic displacements transforming as the Γ_4^- irrep, corresponding to ferroelectric type distortions, the amplitudes of modes affecting the metal cations were used to fix the origin; otherwise, the mode amplitudes of this irrep would appear artificially high due to the floating origin of the unit cell. Finally, we note that if the refined mode amplitudes are treated as the mean absolute value of displacement of an harmonic oscillator, then the amplitude of the harmonic motion will be a factor of $\sqrt{2}$ larger than the refined values.

B. Constrained order parameter directions

Some order parameters can have many degrees of freedom associated with them. The exact number is a function of the degeneracy of the propagation vectors, the dimensionality of

the irrep, and the number of distortions transforming as the irrep. All of these degrees of freedom are described by the collection of symmetry-adapted displacements or "distortion modes" that can be labeled accordingly. For example, in the parent structure ($Pm\bar{3}m$) of ScF_3 there are three types of distortion that transform as X_5^+, which is two-dimensional and associated with the triply degenerate k vector [1/2 0 0], which results in a total of 18 parameters, compared to just 3 for M_2^+ (a triply degenerate single-dimensional k vector) and R_5^- (a nondegenerate k vector with three dimensions). In our refinements, to facilitate a fairer comparison between irreps, the order parameter direction (OPD) associated with the three wave vectors for each distortion have been set to the same values, i.e., the general OPD $(a, b; c, d; e, f)$ has been set to $(a, b; a, b; a, b)$. Different distortion modes of the same type associated with the a and b branches of the OPD are allowed to have different values. However, to further reduce the degrees of freedom that ratio between a and b across all distortion types that transform as a single irrep is fixed to be constant across different temperature ranges. This reduces the number of parameters for X_5^+ from 18 to 4. Physically, these approximations correspond to a harmonic approximation in which the order parameter directions with respect to the propagation vectors and irrep dimensionality are strictly degenerate in energy. An example of this implementation is given in the Supplemental Material.

III. RESULTS AND DISCUSSION

Rietveld refinement of ScF_3 and $CaZrF_6$ powder patterns can be used to gain some insight into the NTE behavior but can also be misleading; the average structure of both compounds remains cubic over the temperature ranges used; however, this structure fits the pair distribution function quite poorly, with PDFGUI [34] refinements of both structures from 1 to 10 Å having $R_{wp} \approx 18\%$ and 20% for ScF_3 and $CaZrF_6$, respectively (see Fig. S1 in the Supplemental Material). The average linear coefficient of thermal expansion (CTE) ≈ -7.5 ppm K^{-1} for ScF_3 matches the literature reports well [9]. The measured $CaZrF_6$ linear CTE, as reported by Hu *et al.* from the same data [18], is -6.69 ppm K^{-1}. In the literature, $CaZrF_6$ is reported to have a magnitude of NTE approximately two to three times that of ScF_3 [9,11] for the temperature range 25–400 K, whereas in these measurements they have quite similar values. The differences from literature reports are in part due to the differing temperature ranges over which CTEs are reported but may also be due to different strains, morphologies and thermal histories of samples [35,36]. The refined atomic displacement parameters (Fig. 2, top) reveal that most thermal motion of the F ions is perpendicular to the M-F-M linkages ($M =$ Sc, Ca, Zr), indicating that a tensioning of these linkages could be responsible for the observed NTE.

Some information can be gained from the PDFs without any modeling. First, the effect of the rocksalt ordering of Ca^{2+} and Zr^{4+} in $CaZrF_6$ can be seen in the presence of two peaks at $r \approx 2$ Å, compared to just one in ScF_3; the greater positive charge of Zr^{4+} compared to Ca^{2+} means the F$^-$ ions do not sit at the midpoint of Ca-F-Zr bonds (Fig. 1). Second, the relative magnitudes of the shorter interatomic separations (Sc-F, Sc-Sc; Ca-F, Zr-F, and Ca-Zr) means that the magnitude
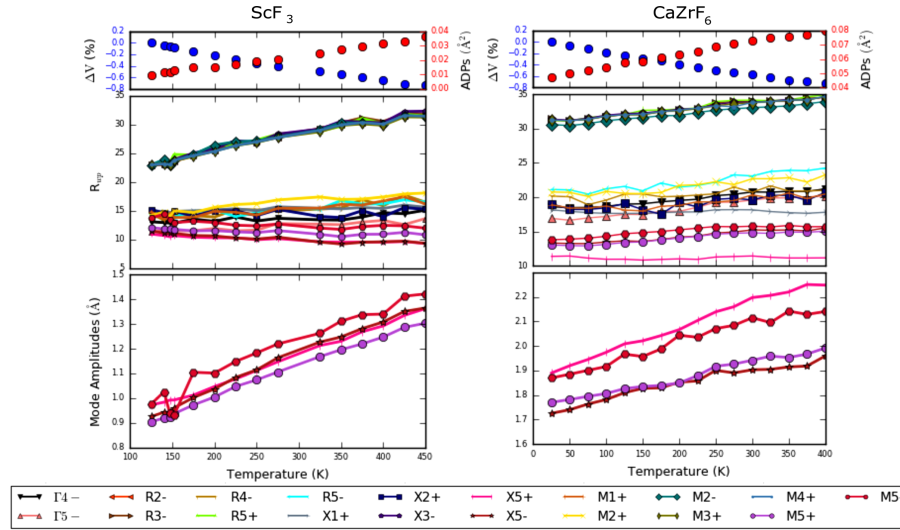
FIG. 2. Transverse atomic displacement parameters from Rietveld refinement (top), the best weighted-phase R factor for each irrep at each temperature (middle), and the Boltzmann weighted mode amplitude (bottom). Results for ScF$_3$ are displayed on the left; those for CaZrF$_6$ are on the right.

of the mean M-F-M angle (M = Sc, Ca, Zr) must deviate from 180°. The magnitude of this deviation is larger for CaZrF$_6$ than for ScF$_3$ (see Fig. S3). The first peak for ScF$_3$ and the first two for CaZrF$_6$ are noticeably less broad than the other peaks, indicating that the M-F bonds are relatively stiff. In contrast, the broadness of the F-F peaks at ~3 Å indicate a propensity for bending of the bond angles within the MF$_6$ octahedra. Little further information can be gained from a simple inspection of the PDFs; hence, analysis of the structures has been performed in terms of symmetry-adapted displacements, as described in Sec. II A.

The results for the symmetry-adapted analysis are shown in Fig. 2 (middle and bottom). The distortions can be classed into three general types: rigid unit modes, consisting of coherent rotations of the octahedra; semirigid "scissoring" modes, where there is a scissoring of some of the M-F bonds within the octahedra; and bond-stretching modes, where some M-F bond lengths change. Most irreps in this analysis have only one distortion associated with them, although there are a few with more. There is a good degree of consistency between the two compounds; both have two "bands" of modes, one that fits well and one that fits poorly. The band with a greater weighted R factor in both compounds consist of the same irreps [R_3^-, R_5^+, X_3^-, M_2^-, M_3^+, M_4^+ (and R_2^- in ScF$_3$)], all of which have distortions with a bond-stretching character. The rest of the irreps, in the band that fits the data well, have at least one distortion associated with them that has a rigid unit (M_2^+ and R_5^-) or scissoring mode character. There are four zone boundary irreps that consistently have the lowest weighted R factor

for both compounds for the majority of temperatures: X_5^+, X_5^-, M_5^+, and M_5^-. All of these irreps have one distortion associated with them that is of scissoring mode character. A depiction of the effect of these modes on the structure of CaZrF$_6$ is shown in Fig. 3. The Γ_5^- irrep also fits well, especially in the refinements that go out to 30 Å. The displacements associated with this irrep are also of a scissoring mode character. However, despite the low R_{wp}, the mode amplitudes are consistently small; hence, most of the analysis is focused on X_5^+, X_5^-, M_5^+, and M_5^-. The weighted mean amplitudes over all refinements at each temperature for these irreps have been calculated and are shown in Fig. 2 (bottom), the weighting being given by a Boltzmann distribution, $w = \exp[(R_{\text{global}} - R_{wp})/\sigma]$, where R_{global} is the minimum weighted R factor achieved across all refinements and all temperatures for the relevant compound and σ is the value of a meaningful difference in the weighted R factor, taken to be 0.1%. R_{global} is taken to be 9% for both compounds. The amplitudes of these modes (X_5^+, X_5^-, M_5^+, and M_5^-) are consistently higher for CaZrF$_6$ than for ScF$_3$; this coincides well with the more significant distortion away from the average structure for CaZrF$_6$, as seen in the mean M-F-M bond angles and the greater magnitude of NTE reported in the literature. These modes also fit significantly better than the RUMs (M_2^+ and R_5^-). These best-fitting irreps (X_5^+, X_5^-, M_5^+, and M_5^-) are all two-dimensional and all have three k vectors; therefore, the OPDs have been constrained as described in Sec. II B to allow for a fairer comparison with the RUMs, which have fewer degrees of freedom associated with them. For the ScF$_3$, the unconstrained R_5^- (which is associated with
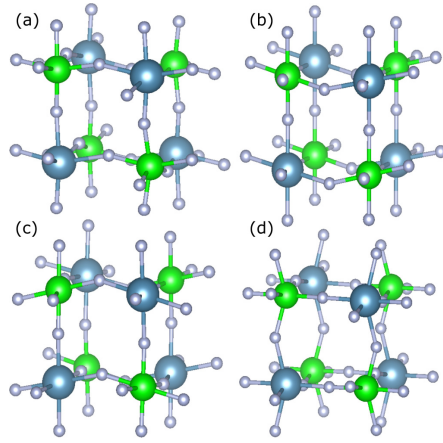
FIG. 3. Representations showing the effect of (a) X_5^+, (b) X_5^-, (c) M_5^+, and (d) M_5^- on the crystal structure of CaZrF6. The distortions are taken from the refinements at 400 K with the lowest R_{wp} and plotted using the VESTA software [33].

the out-of-phase octahedral tilts observed in other metal trifluorides) has a quality of fit similar to that of the constrained X_5^+, X_5^-, and M_5^+ at lower temperatures and consistently performs better than M_5^- (Fig. 4). This suggests that a combination of both the rigid unit and scissoring modes is responsible for NTE, which agrees with a previous molecular dynamics study of these materials [20]. In that study the authors argued that correlated dynamics of flexible polyhedra result in a greater degree of NTE than purely rigid unit dynamics. However, for CaZrF$_6$, we find the constrained scissoring modes, with the exception of M_5^-, consistently perform better than the RUMs. The RUMs also start to perform increasingly poorly as the temperature is raised above 100 K, suggesting that the thermal expansion in CaZrF$_6$ at higher temperatures may well be dominated by contributions from these scissoring modes. The increasing R_{wp} of the RUMs as temperature is increased and the contrasting decrease in R_{wp} seen for the scissoring modes tally well with the phonon dispersion curves of both compounds [13,19]. These show that the scissoring modes are slightly higher in energy than the RUMs, so the scissoring modes will become more active at higher temperatures.

As discussed earlier, the different charges on the two cations in CaZrF$_6$ result in a need to refine the octahedral breathing mode, transforming as the R_2^- irrep, alongside the other distortion modes in order to facilitate a more direct comparison to ScF$_3$. In the average structure of CaZrF$_6$, this breathing mode is frozen in, lowering the symmetry from $Pm\bar{3}m$ to $Fm\bar{3}m$. This also has the effect of mixing the characters of some of the irreps such that the associated atomic displacements now transform as the same irrep. For example, the X_5^+ and M_5^- irreps of $Pm\bar{3}m$ correspond to the X_5^- irrep of $Fm\bar{3}m$, and X_5^- and M_5^+ correspond to X_5^+. To de-
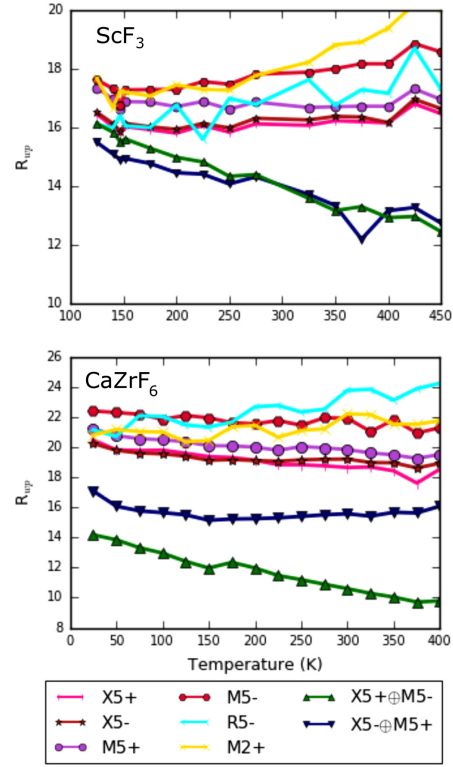

FIG. 4. Comparison of weighted R factors for restricted irreps X_5^+, X_5^-, M_5^+, and M_5^-, unrestricted irreps M_2^+ and R_5^-, and coupled $X_5^+ \oplus M_5^-$ and $X_5^- \oplus M_5^+$.

termine whether this mixing of characters has any effect on the observed local structure of CaZrF$_6$, the constrained OPD X_5^+ and M_5^- modes were refined together (hereafter referred to as $X_5^+ \oplus M_5^-$). This gave a significant improvement to the quality of the fit (Figs. 4 and 5). To determine whether this coupling is a significant effect, results are compared to a two-phase model, in which modes transforming as different irreps are refined in separate phases (Fig. 6). Hereafter these two models will be referred to as the "coupled" model (denoted with $\oplus$) and the "two-phase" model (denoted with &). The coupled modes have a significantly better R factor above 100 K but fit worse than the two-phase refinement below this temperature. The same comparisons are also done for ScF$_3$, where any coupling between phonons of these characters should arise from only anharmonic interactions. In contrast to CaZrF$_6$, which shows a clear preference for coupling between X_5^+ and M_5^-, no evidence of such coupling and hence an anharmonic
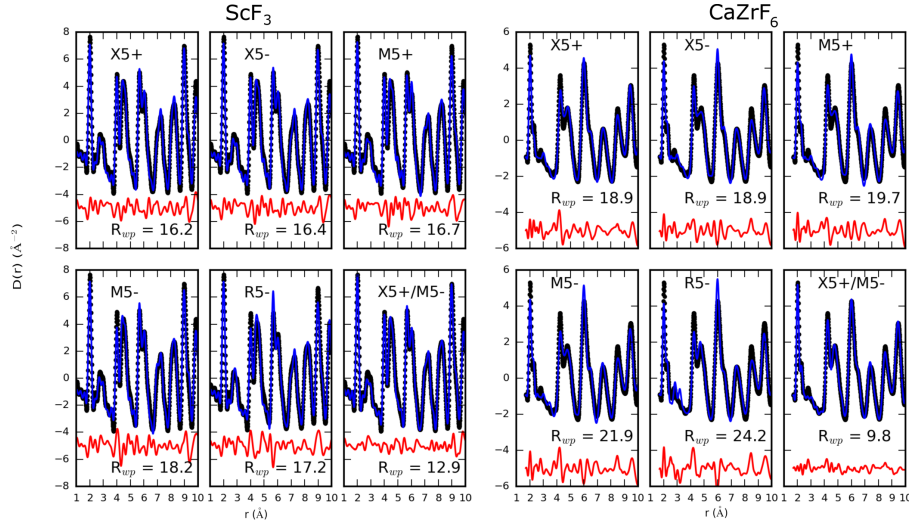
FIG. 5. Comparison of fits to ScF_3 (left) and $CaZrF_6$ (right) PDF data at 400 K using restricted X_5^+, X_5^-, M_5^+, and M_5^-; unrestricted R_5^-; and restricted $X_5^+ \oplus M_5^-$.

interaction is seen here for ScF_3. This suggests that while these scissoring modes are important in determining the local structure of ScF_3, any anharmonic coupling between them has little influence on the lattice dynamics that drive NTE. A similar comparison is made for X_5^-/M_5^+; however, the two-phase refinements consistently fit better than the coupled model for both compounds. This may be due to both distortions locally having the same character (Eu of point group $m\bar{3}m$) with respect to the MF_6 octahedra, making coupling unfavorable.

Next, we investigate if the similar quality of fits of the scissoring modes X_5^+, X_5^-, and M_5^+ and the rigid unit mode R_5^- could be indicative that the two types of distortion are cooperatively coupled to produce the observed NTE. To test this hypothesis, we explore two scenarios: whether this observation is simply due to the dynamic distortions occurring in different sample volumes or at different times from each other or a coupled model which implies that significant anharmonic coupling between these modes is occurring. For both materials, the X_5^+/R_5^- refinements show a sort of behavior similar to the $X_5^+ \oplus M_5^-$ refinements in $CaZrF_6$, in that the refinements of the coupled modes perform worse than the two-phase refinements at lower temperatures but soon cross over to show an improved fit, although the results for $CaZrF_6$ are not robust. Since by the symmetry lowering of the rocksalt ordering in $CaZrF_6$ X_5^+ and M_5^- are allowed to couple and we have shown our analysis to be sensitive to this coupling, the results in Fig. 7 are indicative that there is coupling between the X_5^+ and R_5^- modes. However, as, by symmetry, coupling in $X_5^+ \oplus R_5^-$ is not permitted on its own, we construct a coupled distortion that forms an invariant in the free-energy expansion by inclusion of the M_5^- irrep. The X_5^+ and M_5^-

OPDs in this refinement are still restricted, resulting in three more parameters than the $X_5^+ \oplus M_5^-$ refinements but much improved fits (Figs. 4 and 7). This model results in a very good agreement with the data (Fig. 7).

A very recent analysis of ScF_3 neutron PDF data using the reverse Monte Carlo (RMC) method by Dove *et al.* [37] similarly concluded that it is a combination of structural flexibility and RUMs that causes the NTE in the compound. Dove *et al.* argued that the flexibility of the structure allows RUMs and RUM-like modes to occupy a larger volume in reciprocal space, meaning they give a greater contribution to the overall thermal expansion behavior, compared to entirely rigid structures. Our results here echo this conclusion and underline the dominant contribution of scissoring modes in describing the fluctuations from the average symmetry. Additionally, in the work of Dove *et al.*, geometric algebra was used to quantify the proportion of the motion of the atoms in ScF_3 originating from correlated whole-body octahedral motion, deformations of the F-Sc-F right angles, and changes in the Sc-F bond length. This analysis resulted in a ratio of approximately 7:2:1 of bends:rotations:stretches. The $X_5^+ \& R_5^-$ and $X_5^- \& R_5^-$ two-phase refinements described previously give a similar ratio of bends:rotations, approximately 8:2, although the contribution from stretches is negligible (<1% of the total motion). The $X_5^+ \& R_5^-$ refinements for $CaZrF_6$ give an approximately 7:3 ratio of bends:rotations, again with a negligible contribution from stretches. There is hence a high degree of consistency between results derived via big-box RMC methods and those of our symmetry-motivated approach here. A different analysis of neutron PDF data of ScF_3, performed by Wendt *et al.* [38], models the F atoms as being randomly positioned on a
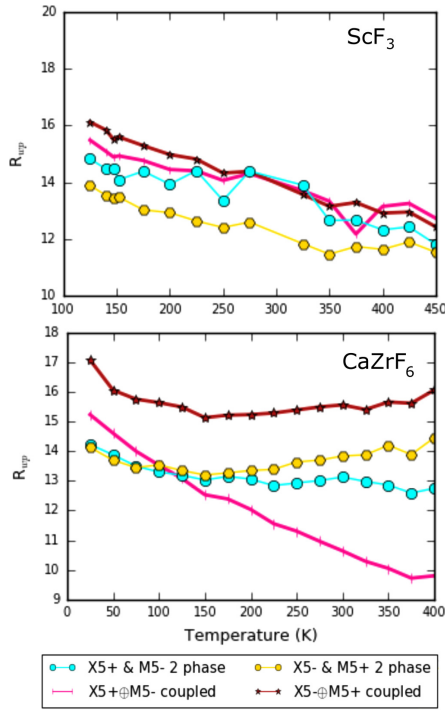
FIG. 6. Comparison of coupled and two-phase fits to PDF data as a function of temperature for ScF_3 (top) and $CaZrF_6$ (bottom), as described in the text.
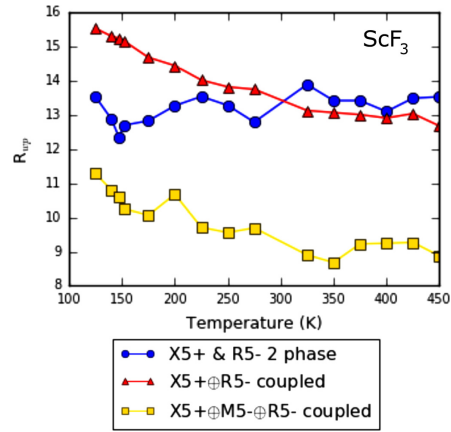

FIG. 7. Comparison of fits for $X_5^+ \oplus R_5^-$ using a two-phase model (blue) and a coupled model (red) and $X_5^+(a, b; 0, 0; 0, 0) \oplus M_5^-(0, 0; c, d; 0, 0) \oplus R_5^-(e, f, g)$ (yellow) for ScF_3.

torus-shaped Gaussian distribution around the F sites in the average structure, with no correlation between neighboring F atoms, in a fashion similar to entropic elasticity in polymers. The model reproduces the observed NTE behavior and F-F distribution up to ≈ 700 K. It shows how important the flexibility of Sc-F-Sc linkages is in this material, a fact consistent with our findings here; however, it fails to account for the full range of NTE in the material. The previously discussed RMC model shows that at least a small fraction of the motion of F atoms in the material can be accounted for by correlated rigid-unit-type distortions, results which are compatible with our symmetry-based analysis of the x-ray PDF data.

In summary, we have shown via a symmetry-motivated real-space analysis of PDF data that the most significant distortions in these ReO_3-like NTE materials are scissoring modes, which involve scissoring of the MF_6 octahedral bond

angles. These modes have a greater amplitude in $CaZrF_6$ than ScF_3, which corresponds well to the greater magnitude of NTE reported in the literature for the former. Coupling between these modes and the rigid unit modes has been shown to be active and the likely origin of unusually high NTE in these structures.

The ScF_3 data for this study are available as a supporting data set [39].

[1] J. S. Evans, T. A. Mary, T. Vogt, M. A. Subramanian, and A. W. Sleight, Chem. Mater. **8**, 2809 (1996).

[2] M. Dapiaggi, W. Tiano, G. Artioli, A. Sanson, and P. Fornasini, Nucl. Instrum. Methods Phys. Res., Sect. B **200**, 231 (2003).

[3] T. Chatterji, P. F. Henry, R. Mittal, and S. L. Chaplot, Phys. Rev. B **78**, 134105 (2008).

[4] T. Chatterji, T. C. Hansen, M. Brunelli, and P. F. Henry, Appl. Phys. Lett. **94**, 241902 (2009).

[5] I. Grobler, V. J. Smith, P. M. Bhatt, S. A. Herbert, and L. J. Barbour, J. Am. Chem. Soc. **135**, 6411 (2013).

[6] N. Lock, Y. Wu, M. Christensen, L. J. Cameron, V. K. Peterson, A. J. Bridgeman, C. J. Kepert, and B. B. Iversen, J. Phys. Chem. C **114**, 16181 (2010).

[7] M. T. Dove and H. Fang, Rep. Prog. Phys. **79**, 066503 (2016).

[8] G. D. Barrera, J. A. O. Bruno, T. H. K. Barron, and N. L. Allan, J. Phys.: Condens. Matter **17**, R217 (2005).

[9] B. K. Greve, K. L. Martin, P. L. Lee, P. J. Chupas, K. W. Chapman, and A. P. Wilkinson, J. Am. Chem. Soc. **132**, 15496 (2010).

[10] S. U. Handunkanda, E. B. Curry, V. Voronov, A. H. Said, G. G. Guzmán-Verri, R. T. Brierley, P. B. Littlewood, and J. N. Hancock, Phys. Rev. B **92**, 134101 (2015).

[11] J. C. Hancock, K. W. Chapman, G. J. Halder, C. R. Morelock, B. S. Kaplan, L. C. Gallington, A. Bongiorno, C. Han, S. Zhou, and A. P. Wilkinson, Chem. Mater. **27**, 3912 (2015).

[12] L. Hu, J. Chen, A. Sanson, H. Wu, C. Guglieri Rodriguez, L. Olivi, Y. Ren, L. Fan, J. Deng, and X. Xing, J. Am. Chem. Soc. **138**, 8320 (2016).

[13] M. K. Gupta, B. Singh, R. Mittal, and S. L. Chaplot, Phys. Rev. B **98**, 014301 (2018).

[14] M. G. Tucker, A. L. Goodwin, M. T. Dove, D. A. Keen, S. A. Wells, and J. S. O. Evans, Phys. Rev. Lett. **95**, 255501 (2005).

[15] A. Sanson, M. Giarola, G. Mariotto, L. Hu, J. Chen, and X. Xing, Mater. Chem. Phys. **180**, 213 (2016).

[16] N. Sennova, R. Bubnova, J. Shepelev, S. Filatov, and O. Yakovleva, J. Alloys Compd. **428**, 290 (2007).

[17] A. Senyshyn, B. Schwarz, T. Lorenz, V. T. Adamiv, Y. V. Burak, J. Banys, R. Grigalaitis, L. Vasylechko, H. Ehrenberg, and H. Fuess, J. Appl. Phys. **108**, 093524 (2010).

[18] L. Hu, J. Chen, J. Xu, N. Wang, F. Han, Y. Ren, Z. Pan, Y. Rong, R. Huang, J. Deng, L. Li, and X. Xing, J. Am. Chem. Soc. **138**, 14530 (2016).

[19] C. W. Li, X. Tang, J. A. Muñoz, J. B. Keith, S. J. Tracy, D. L. Abernathy, and B. Fultz, Phys. Rev. Lett. **107**, 195504 (2011).

[20] J. T. Schick and A. M. Rappe, Phys. Rev. B **93**, 214304 (2016).

[21] Y. Oba, T. Tadano, R. Akashi, and S. Tsuneyuki, Phys. Rev. Mater. **3**, 033601 (2019).

[22] A. Sanson, Mater. Res. Lett. **7**, 412 (2018).

[23] A. M. Glazer, Acta Crystallogr., Sect. B **28**, 3384 (1972).

[24] M. S. Senn, D. A. Keen, T. C. A. Lucas, J. A. Hriljac, and A. L. Goodwin, Phys. Rev. Lett. **116**, 207602 (2016).

[25] A.-C. Dippel, H.-P. Liermann, J. T. Delitz, P. Walter, H. Schulte-Schrepping, O. H. Seeck, and H. Franz, J. Synchrotron Radiat. **22**, 675 (2015).

[26] M. Basham, J. Filik, M. T. Wharmby, P. C. Chang, B. El Kassaby, M. Gerring, J. Aishima, K. Levik, B. C. Pulford, I. Sikharulidze, D. Sneddon, M. Webber, S. S. Dhesi, F. Maccherozzi, O. Svensson, S. Brockhauser, G. Náray, and A. W. Ashton, J. Synchrotron Radiat. **22**, 853 (2015).

[27] S. E. McLain, D. T. Bowron, A. C. Hannon, and A. K. Soper, GUDRUN, a computer program developed for analysis of neutron diffraction data, Chilton, ISIS Facility, Rutherford Appleton Laboratory, 2012.

[28] X. Qiu, J. W. Thompson, and S. J. Billinge, J. Appl. Crystallogr. **37**, 678 (2004).

[29] S. R. Popuri, R. Decourt, J. A. McNulty, M. Pollet, A. D. Fortes, F. D. Morrison, M. S. Senn, and J. W. Bos, J. Phys. Chem. C **123**, 5198 (2019).

[30] B. J. Campbell, H. T. Stokes, D. E. Tanner, and D. M. Hatch, J. Appl. Crystallogr. **39**, 607 (2006).

[31] A. A. Coelho, P. A. Chater, and A. Kern, J. Appl. Crystallogr. **48**, 869 (2015).

[32] See Supplemental Material at http://link.aps.org/supplemental/10.1103/PhysRevB.101.064306 for Rietveld refinements, average structure refinements of PDF data and comparisons of different peak width functions.

[33] K. Momma and F. Izumi, J. Appl. Crystallogr. **44**, 1272 (2011).

[34] C. L. Farrow, P. Juhas, J. W. Liu, D. Bryndin, E. S. Boin, J. Bloch, T. Proffen, and S. J. Billinge, J. Phys.: Condens. Matter **19**, 335219 (2007).

[35] C. Yang, P. Tong, J. C. Lin, X. G. Guo, K. Zhang, M. Wang, Y. Wu, S. Lin, P. C. Huang, W. Xu, W. H. Song, and Y. P. Sun, Appl. Phys. Lett. **109**, 023110 (2016).

[36] L. P. Prisco, C. P. Romao, F. Rizzo, M. A. White, and B. A. Marinkovic, J. Mater. Sci. **48**, 2986 (2013).

[37] M. T. Dove, J. Du, Z. Wei, D. A. Keen, M. G. Tucker, and A. E. Phillips, arXiv:1905.09250.

[38] D. Wendt, E. Bozin, J. Neuefeind, K. Page, W. Ku, L. Wang, B. Fultz, A. Tkachenko, and I. Zaliznyak, Sci. Adv. **5**, eaay2748 (2019).

[39] https://doi.org/10.6084/m9.figshare.11605278.v1.

Chapter 4

Soft mode anisotropy in negative thermal expansion material ReO$_3$

Soft mode anisotropy in negative thermal expansion material ReO_3

Tobias A. Bird,[1] Mark G. L. Wilkinson,[2] David A. Keen,[3] Ronald I. Smith,[3] Nicholas
C. Bristowe,[4] Martin T. Dove,[5, 6, 2] Anthony E. Phillips,[2, *] and Mark S. Senn[1, †]

[1]*Department of Chemistry, University of Warwick,*
Gibbet Hill, Coventry, CV4 7AL,United Kingdom
[2]*School of Physics and Astronomy, Queen Mary University of London, London, E1 4NS, United Kingdom*
[3]*ISIS, Rutherford Appleton Laboratory, Harwell Campus,*
Didcot, Oxfordshire OX11 0QX, United Kingdom
[4]*Centre for Materials Physics, Durham University,*
South Road, Durham DH1 3LE, United Kingdom
[5]*Schools of Computer Science and Physical Science & Technology,*
Sichuan University, Chengdu 610065, People's Republic of China
[6]*Department of Physics, School of Sciences, Wuhan University of Technology,*
205 Luoshi Road, Homgshan district, Wuhan, Hubei 430070, People's Republic of China
(Dated: August 6, 2021)

We use a symmetry-motivated approach to analyse neutron pair distribution function data to investigate the mechanism of negative thermal expansion (NTE) in ReO_3. This analysis shows that the local structure of ReO_3 is dominated by an in-phase octahedral tilting mode and that the octahedral units are far less flexible to scissoring type deformations than the octahedra in the related compound ScF_3. These results support the idea that structural flexibility is an important factor in NTE materials, allowing the phonon modes that drive a volume contraction of the lattice to occupy a greater volume in reciprocal space. The lack of flexibility in ReO_3 restricts the NTE-driving phonons to a smaller region of reciprocal space, limiting the magnitude and temperature range of NTE. In addition, we investigate the thermal expansion properties of the material at high temperature and do not find the reported second NTE region. Finally, we show that the local fluctuations, even at elevated temperatures, respect the symmetry and order parameter direction of the observed $P4/mbm$ high pressure phase of ReO_3. The result indicates that the motions associated with rigid unit modes are highly anisotropic in these systems.

I. INTRODUCTION

The phenomenon of negative thermal expansion (NTE) is an intriguing and unusual property for a material to exhibit. Broadly speaking, there are two families of NTE materials: those in which the anomalous thermal expansion behaviour arises solely from vibrational effects, and those in which it has an electronic origin[1–4]. In a typical material, we expect to observe positive thermal expansion (PTE) since the anharmonic shape of the interatomic potential leads to an increase in the equilibrium distance between two atoms as they gain more energy from an increase in temperature. The typical explanation for how vibrational effects can lead to a deviation from this behaviour is the "tension effect"[1,4]. A lot of structural NTE materials consist of a network of cation-anion linkages, often with an anion linked to two cations in a straight line[5–8]. If the energy cost to expand these bonds is quite high, then the central ion can displace perpendicularly to the bonds, which has the effect of pulling the two outer ions towards each other. The bonds connecting the linked ions still show PTE, but the linkage as a whole shrinks. This hypothesis is supported by neutron and X-ray powder diffraction experiments showing significant transverse atomic displacement parameters[4]. The tension effect is often realised in NTE materials *via* rigid unit modes (RUMs)[4,9] – materials made from a network of rigid polyhedra often have a high energy cost to

distort the polyhedral units but a low energy cost for co-operative rotations of the polyhedra. These distortions typically cause a contraction of the volume of the material and since they are low in energy will have a large contribution to the overall thermal expansion behaviour. Many of these cation-anion linked NTE materials give rise to a network of connected polyhedra, such as the archetypal NTE material ZrW_2O_8[10], SiO_2[11] and layered materials showing uniaxial NTE such as $Ca_3Mn_2O_7$[12].

Two materials that are often used to illustrate the RUM model are ReO_3 and ScF_3, due to their relatively simple structure when compared to more complex materials like ZrW_2O_8. Both compounds consist of corner-sharing octahedra and both exhibit NTE, up to around 220 K in ReO_3[13,14] and 1100 K in ScF_3[15], although the exact range of NTE in the former is dependent on sample preparation[16]. There has also been an observation of a reappearance of NTE in ReO_3 between 600–700 K[14]. This overlaps with the temperature at which ReO_3 is known to decompose to Re_2O_7 and ReO_2[17]. Both ReO_3 and ScF_3 undergo a phase transition *via* octahedral tilts with applied pressure. In ReO_3, the octahedral tilts in successive planes along the tilt axis are in-phase tilts[18–21], whereas for ScF_3, the tilts are out of phase[15,22].

Compared to typical ABX_3 perovskites, which also exhibit rigid rotations of the octahedral units, ReO_3 and ScF_3 both have a vacant A-site, allowing larger tilt angles[19]. Recent analysis of the local structure of ScF_3[23,24] demonstrated that flexibility of the octahedra

themselves, *i.e.*, distortions of the intraoctrahedral F–Sc–F bond angles away from 90°, is a key contributor to the NTE. In perovskites, pure RUMs are restricted to the line M-R in reciprocal space, which in principle gives their mode Grüneisen parameters a vanishingly small contribution towards the mean Grüneisen parameter. On moving away from this line, the modes have an increasing component of octahedral distortion. These modes, termed quasi-RUMs, can still contribute to NTE if they have negative Grüneisen parameters. Simplistically, structures with greater flexibility will have a greater volume of reciprocal space occupied by quasi-RUMs with a negative Grüneisen parameter than those of lesser flexibility. In addition, these modes will have a greater contribution to the mean Grüneisen parameter, since their component of octahedral deformation will have a lower energy cost[25]. The oxygen anions in ReO_3 have an increased charge compared to the fluoride anions in ScF_3 and therefore an increased coulomb repulsion force between them, which one might expect to decrease the flexibility of the octahedra. Molecular dynamics simulations of an ReO_3-like structural model have also shown a decreasing magnitude of NTE for increasing anion interaction strengths[26]. In particular, the sign of the coefficient of thermal expansion in ScF_3 has been shown to be highly sensitive to changes in the force constant governing flexing of the F−Sc−F right angle[24].

We investigate this hypothesis by using a symmetry-motivated approach to analyze neutron pair distribution function (PDF) data collected on ReO_3 across its entire temperature range of stability. Our study enables us to identify the characters of the dominant dynamic deviations away from the average structure as a function of temperature.

II.   EXPERIMENTAL DETAILS

Rhenium trioxide was purchased from Sigma-Aldrich and used as received. A 4.63965 g sample was loaded into a vanadium can of 6 mm diameter and mounted onto the Polaris instrument at ISIS Neutron and Muon Source (Rutherford Appleton Laboratory, U.K.)[27]. Data were collected in "short" 13 μA hr runs for Rietveld refinement and "long" sets of five 150 μA hr runs for pair distribution function analysis, equivalent to data collection periods of 5 minutes and 1 hour for each run, respectively. For low temperatures (between 4 K and 293 K) a helium flow cryostat was used, whereas for higher temperatures from 293 K to 750 K a furnace was used. The furnace data were collected in two separate experiments, due to an unscheduled beam shut-off at the facility during the first experiment. The furnace data for 600 K and above were taken from the second experiment. Both experiments used the same ReO_3 sample, stil loaded in the same sample can. During these experiments, data were also collected from the empty instrument, empty sample environment, and an empty vanadium can for
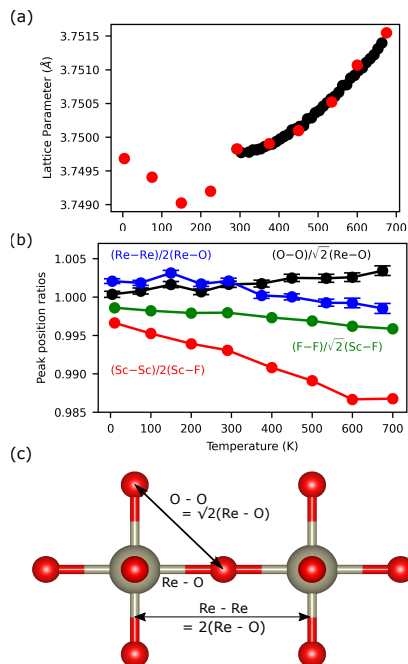

Figure 1. (a) Temperature variation in the cubic lattice parameter of ReO_3 from Rietveld refinement. The data points shown in red are from the longer collections which were used for total scattering measurements. (b) Plots of the PDF peak position ratios indicated in the legend. Peak positions for ScF_3 were extracted from atomistic configurations generated using the reverse Monte Carlo method on neutron PDF data[24] and OriginLab was used to fit the peaks for ReO_3. The error bars for ReO_3 correspond to the uncertainties from the peak fitting algorithm. We note that values of $(Re–Re)/2(Re–O)$ above 1 are not physically possible, but at worst they are less than 0.05 % too high. This is likely due to a systematic error and we believe that the trends with temperature are reliable. The uncertainty in these atom pair distances due to the r-space resolution ($\Delta r \approx 0.1$ Å) is an order of magnitude greater than this. (c) A diagram showing how the O–O and Re–O distances in the average structure of ReO_3 are related to one another.

background correction, as well as a solid vanadium rod for normalisation. For average structure determination, data reduction was carried out using Mantid[28]. The lattice parameter for each temperature was determined by Rietveld refinement using the EXPGUI[29] interface to
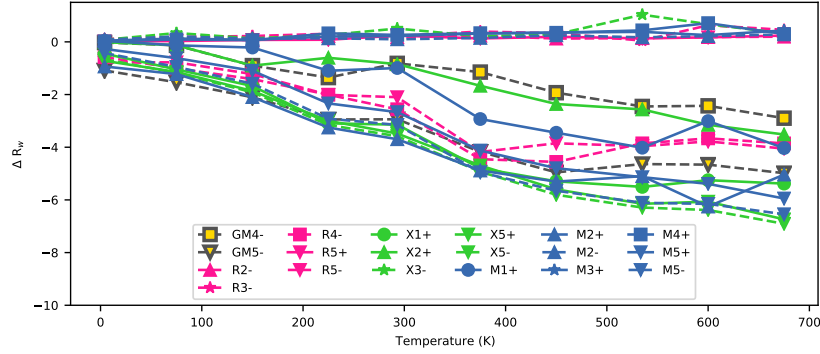
Figure 2. The results of the SAPA on ReO$_3$. The best individual fitting statistic is plotted for each irrep at each temperature. The R_w is shown relative to the R_w for the refinement with no symmetry adapted displacement modes active. The irreps are labelled as follows: colour denotes the k-point of the irrep, with blue referring to the M point, green to X, pink to R and yellow to Γ; marker shape denotes the irrep number, with a circle referring to 1, an upward-pointed triangle to 2, a star to 3, a square to 4 and a downward-pointed triangle to 5; linestyle denotes the parity of the irrep, with a solid line referring to a + irrep, and a dashed line referring to a − irrep. A representative fit of the average structure to the PDF at 293 K is shown in the SI.

GSAS[30] against the data from Polaris detector banks 3–5, refining both the unit cell and atomic displacement parameters (noting that all atomic coordinates for the Re and O atoms are fixed by symmetry in the $Pm\bar{3}m$ space group). A representative fit to the data at 150 K is included in the SI. The background was modelled using an 8-term shifted Chebyschev function. An absorption correction was refined to account for the neutron absorption of rhenium.

To ensure that the unit cell parameters were consistent between the cryostat and furnace environments, data were collected at 293 K in both environments. For the furnace data set, the unit cell parameter was fixed at the value determined from the cryostat data and the diffractometer constant DIFC for the backscattering detector bank was refined instead. This new value was held constant for subsequent furnace data sets to ensure self-consistency across the entire temperature range (with an identical approach used to ensure consistency between the first and second furnace data sets).

For local structure analysis, Gudrun[31] was used to subtract the background, correct the data for self-shielding, absorption, and multiple scattering, normalise them to give the scattering function $S(Q)$, and finally Fourier transform this to give the pair distribution function $D(r)$. The scattering function $S(Q)$ was determined over the Q range 0.6–50 Å^{-1} in steps of 0.02 Å^{-1}. This data normalisation is also dependent on the density of the powdered sample: the powder packing fraction was initially set to the value measured experimentally and then adjusted by hand for all data sets in order to set the limiting value of the total scattering structure factor, $F(Q)$[32] , as $Q \to 0$ to its theoretical value of $-\sum_i c_i \bar{b}_i^2$[33], and to set the coordination number for the first peak (Re–O) to its ideal value of six O atoms per Re atom.

Analysis of the pair distribution functions was carried out using the symmetry-adapted PDF analysis (SAPA) method described in ref. 23. For each sample, a $2 \times 2 \times 2$ $P1$ supercell of the $Pm\bar{3}m$ aristotype ReO$_3$ with Re at (0.5, 0.5, 0.5) and O at (0.5, 0.5, 0) was generated and parameterised in terms of symmetry adapted displacements using the ISODISTORT software[34]. The modes modelled using this supercell expansion only represent a small fraction of possible phonon modes. However, even if the exact wave vectors of the soft phonon modes do not coincide with the Γ, X, M or R points of reciprocal space, since their characters should vary continuously between high symmetry points, the nature of the local symmetry breaking should still be manifested in our analysis. The generated mode listings were output in .cif format and then converted to the .inp format of the TOPAS Academic software v6 using the Jedit macros[35]. In total, there were 96 modes which transformed according to one of 19 irreducible representations. For each irreducible representation (irrep) at each temperature, refinements of the corresponding modes were started from random starting mode amplitudes. This was repeated 500 times for each irrep at each temperature to ensure the global minimum of the refinement was reached. For all temperatures, the refinements were carried out with a fitting range of 1.5 to 10 Å. Refinements were carried out using the Topas Academic software v6[36].
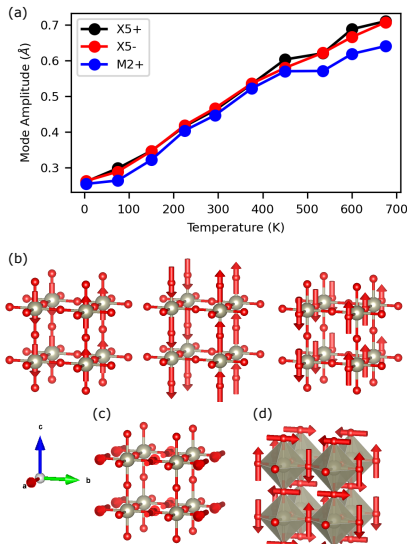
Figure 3. (a) Temperature variation of the normalised mode amplitudes of the modes belonging to the M_2^+, X_5^+ and X_5^- irreps. The values were calculated from the lowest R_w refinement for each temperature and irrep from the output of the SAPA. These values are supercell normalised mode amplitudes (A_s as defined in ISODISTORT). To convert to the A_p values, divide by a factor of $2\sqrt{2}$. Visualisations of the modes which transform as each irrep are shown below. Specifically, (b) the three distortions for the X_5^+ (a,0;0,0;0,0), (c) X_5^- (a,0;0,0;0,0) and (d) M_2^+ (a;0;0).

The DFT calculations were performed using the Vienna Ab Initio Simulation Package (VASP)[37–40], version 5.4.4. We employed the PBEsol exchange correlation potential[41] and projector augmented-wave (PAW) pseudopotentials[38,42], as supplied within the VASP package. A plane wave basis set with a 900 eV energy cutoff and a $12 \times 12 \times 12$ Monkhorst-Pack k-point mesh with respect to the parent cubic primitive cell (scaled accordingly for other supercells) were found suitable.

III. RESULTS AND DISCUSSION

Rietveld refinement of the **a** unit cell parameter from the Bragg reflection positions observed during the total scattering experiment shows we observe the same low temperature negative thermal expansion range as literature reports for ReO_3[13,14] (Fig. 1 (a)). The high tem-

perature measurements for both long and short runs do not show the second region of NTE observed by Chatterji *et al*[14]. Our conjecture is that the original observation of this phenomenon was likely due to sample decomposition, since above 673 K, ReO_3 starts to decompose *via* disproportionation[17].

We can gain some insights into the local structure from the PDFs of ReO_3 without performing any modelling. In Fig 1 (b), we quantitatively estimate the flexing of the O–Re–O right angle and Re–O–Re linkage. In the average structure, the plotted ratios are constrained to be constant at a value of one, due to a 90° O–Re–O bond angle and a straight Re–O–Re bond. The intercepts of these ratios at 0 K reflect the inherent flexibility of the structures, since the force constants governing both types of flexing motion do not change with temperature. This shows that ScF_3 is more flexible than ReO_3, presumably due to the lower charge of F^- compared to O^{2-}. The difference in flexibility with respect to distortions of the O–Re–O (F–Sc–F) bond angle is smaller than that for distortions of the Re–O–Re (Sc–F–Sc) linkage. However, molecular dynamics simulations have shown that the sign of the coefficient of thermal expansion is more sensitive to changes in the force constant governing the former[24]. Another difference of note is that the trends in the X–M–X bond angle for ReO_3 and ScF_3 are opposed. The average O–Re–O bond angle increasing with temperature while the F–Sc–F bond angle decreases. These differing trends could reflect that phonon modes with differing characters and amplitude cause the octahedral deformations.

To gain a fuller understanding of the character of the soft modes in ReO_3, we turn to the results from our SAPA method. In Fig 2, we can see there is a group of irreducible representations whose modes consistently give the best improvement in R_w compared to the average structure refinements at each temperature. These are M_2^+, M_5^+, M_5^-, X_5^+, X_5^- and Γ_5^-. All but M_2^+ have symmetry-adapted displacements associated with them which are of a scissoring character: the Re-O octahedral bond lengths remain unchanged, but some of the bond angles are distorted *via* transverse displacements of the O anions. The M_5^- and X_5^+ irreps both also support bond-stretching. However, this type of distortion is relatively high in energy so contributes negligibly both to the overall coefficient of thermal expansion and to the refined distortion. The amplitudes of these scissoring modes (Fig 3 (a)) are smaller than for ScF_3[23] which further supports the hypothesis that a lower flexibility is responsible for the reduced magnitude of NTE in ReO_3 compared to ScF_3.

The other local symmetry breaking which is consistently amongst those which show the most improvement in R_w from the average structure, and at some temperatures shows the most improvement overall, transform as irrep M_2^+. The distortions belonging to this irrep correspond to an in-phase tilt of the octahedra, with no other type of distortion associated with it, so it is of pure RUM character. This is a significant distortion for ReO_3 which

undergoes a phase transition with applied pressure (*ca.* 5 kbar at 300 K) during which the M_2^+ mode softens and the tilts are "frozen in" to the structure. To compare the relevant prevalence of this pure RUM mode with the scissoring modes, we refined a two-phase model, with displacements from the X_5^- irrep in one phase and from the M_2^+ in another. The X_5^- irrep was chosen here since all the displacements associated with it are of a scissoring mode character and it provides a better fitting statistic than other irreps for which this is also true (M_5^+ and Γ_5^-, Fig 2). At temperatures below 225 K, in the negative thermal expansion region, the RUM dominates as evidenced by the refined phase fraction in Fig 4 (a). At higher temperatures, there is a balance between the two phase fractions, indicating that both scissoring and RUM type motions account for a substantial proportion of the dynamic distortions.

At first glance, this increase in the proportion of motion arising from scissoring modes, coincident with the onset of PTE, is perhaps contradictory to the quasi-RUM mechanism for NTE which has been previously discussed for ScF_3. In ScF_3, the octahedral flexibility means a significant proportion of quasi-RUMs, modes which are of mixed scissoring and rigid unit mode character, will have a negative Grüneisen parameter. This expands the volume occupied in reciprocal space by NTE phonons, increasing the overall contribution of modes with negative mode Grüneisen parameters to the mean Grüneisen parameter. Previous analysis of both X-ray and neutron PDF data of ScF_3 finds that the majority of motion of fluorine atoms comes from scissoring modes, with approximate scissoring:RUM ratios of 4:1 (0.8 as a phase fraction) from SAPA analysis[23] and 3.5:1 (0.78) from reverse Monte Carlo analysis[24] at all temperatures. Our analysis in Fig 4 shows that in ReO_3, the scissoring:rotation ratio is close to 1:1 at 675 K, but drops to 1:10 by 4 K. These ratios suggest that there is significantly more resistance to octahedral deformations in ReO_3 than ScF_3. However, within renormalized phonon theory, we would expect the phase fractions[43] in Fig 4 to remain constant with temperature, as we observe in our RMC analysis of ScF_3. The fact that the proportion of the scissoring to RUM phase fraction increases at high temperatures is more likely to reflect a hardening of the RUM than a sudden increase in the flexibility of the structure. This supposition is supported by the observation that the pressure at which the first phase transition occurs, increases with temperature[20]. The increased energy of the phonon modes with RUM character on warming lowers their contribution to the mean Grüneisen parameter at a given temperature. This hardening also has a knock-on effect on the quasi-RUMs, since their RUM component will also have a higher energy. It is of course tempting to suggest that this hardening of the modes with RUM character above 200 K is responsible for the concurrent change in sign of the bulk thermal expansion coefficient. However, it is conversely evident from the negative sign of the Grüneisen parameters of these modes that an in-
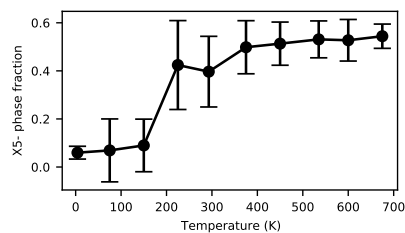

Figure 4. A plot of the weighted mean phase fraction of the X_5^- phase from two-phase refinements of M_2^+ in one phase and X_5^- OPD in the other. Similarly to the SAPA, 500 repeats were performed at each temperature from randomised starting values and the weighting, w, of each refinement towards the mean was calculated according to $w = \exp[(R_{min} - R_i)/0.1]$, where R_{min} is the minimum R_w for each temperature and the R_i are the R_w of each refinement.

crease in volume would result in their hardening. Hence, we can not establish a causal connection with the current set of observations.

Next, we consider the sequence of phase transitions in ReO_3 under pressure, since these are likely to be indicative of the character of the soft modes observed in the present study. The nature of the initial phase transition with pressure has come under question. The consensus in the literature is that at 5 kbar and 300 K, ReO_3 undergoes a transition to a tetragonal $P4/mbm$ structure involving an in-phase octahedral tilt along one pseudocubic axis, with only one arm of the propagation vector active (M_2^+ $(a; 0; 0)$). At 5.3 kbar it undergoes a further transition to a cubic $Im\bar{3}$ structure, with all 3 arms of the propagation vector active (M_2^+ $(a; a; a)$) and a tilt of equal amplitude along all three pseudo-cubic axes. In Glazer notation, this corresponds to a transition from an $a^+b^0b^0$ tilt system to $a^+a^+a^+$. Some experiments, however, report that there is no transition to the $P4/mbm$ structure[20], only observing the transition to the $Im\bar{3}$ phase.

Since we expect the distortion which is responsible for the phase transition to be a soft mode at ambient pressure, we can interrogate our PDFs to see if a precursor signature of this phase transition is already present. To do this, we parameterised the three dimensional M_2^+ order parameter direction (OPD) $(a; b; c)$ in terms of spherical polar coordinates with $a = r \cos \phi \sin \theta$, $b = r \sin \phi \sin \theta$ and $c = r \cos \theta$. Refinements were performed at fixed values on a grid covering the range of values of θ and ϕ, whilst allowing the amplitude of the mode to vary. In this parameterisation, the OPD corresponding to $P4/mbm$ symmetry occurs if both θ and ϕ are integer multiples of $\pi/2$, and for all values of ϕ when $\theta = 0, \pi$. The $Im\bar{3}$ OPD would occur when $\phi = \pi/4, 3\pi/4, 5\pi/4$ or
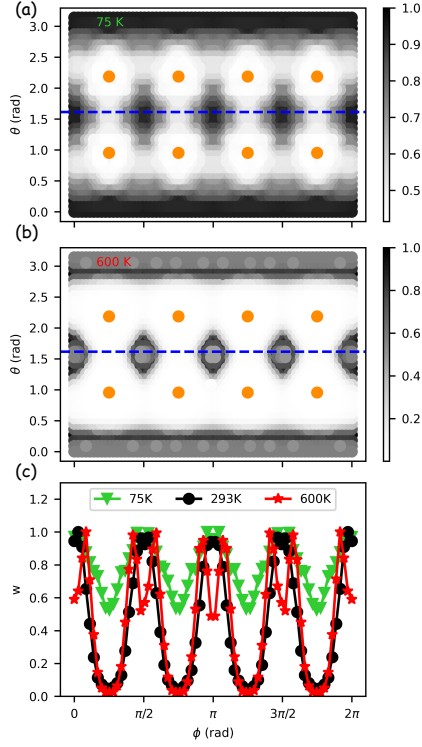
Figure 5. Plots showing the R_w of different M_2^+ OPDs parameterised by spherical coordinates at (a) 75 and (b) 600 K respectively. The greyscale color map corresponds to a value $w = \exp[(R_{min} - R_i)/0.1]$ where R_{min} is the minimum R_w for each temperature and the R_i are the R_w of each refinement. A value of $w = 1$ then indicates a refinement with a fitting statistic equal to the best fitting statistic across all refinements for that temperature. Thus, darker regions represent better fits than lighter regions. Different color bars are shown for the different temperatures since R_{min} changes with temperature. To aid the eye, points corresponding to an order parameter direction with $Im\bar{3}$ symmetry are shown in orange. (c) A cut through of the above plots, shown in (a) & (b) with a blue dashed line, showing the variation in the value w for a fixed value of θ. Equivalent plots for the remaining temperature points are shown in the SI.

$7\pi/4$ and $\theta = \arctan(\pm\sqrt{2})$.

In the Landau theory of phase transitions, the free energy expansion is written as a linear combination of sets of polynomials in the components of the order parameter. These polynomials must be invariant under all of the symmetry operations of the parent space group, $Pm\bar{3}m$ in this case. Since the invariant polynomial truncated at the second (harmonic) order is of the form $a^2 + b^2 + c^2$, which in the spherical coordinate parameterisation is equivalent to r^2, the anisotropic R_w distribution we observe over the spherical surface (Fig 5), is indicative of significant anharmonicity.

At low temperatures, the lowest R_w refinements are clustered around points corresponding to the $P4/mbm$ OPD (Fig 5 (a)), while the worst fitting refinements are clustered around points corresponding to $Im\bar{3}$ symmetry. Halfway in between points described by $P4/mbm$ and $Im\bar{3}$ symmetry, corresponding to the OPD $(a; a; 0)$ with $I4/mmm$ symmetry, a small improvement in the quality of fit is observed compared to the OPD with $Im\bar{3}$ symmetry. These areas correspond to distortions involving tilts about two orthogonal axes. This likely reflects a saddle point in the energy between the best ($P4/mbm$) and worst ($Im\bar{3}$) fitting OPDs. The anisotropy in the fitting statistics, that becomes more evident at higher temperatures and at large mode amplitudes, points towards significant anharmonicity, since, as discussed above, at the harmonic (quadratic) level, all OPDs must be equivalent with respect to the free energy expansion. Comparing OPDs against our PDF data for $Im\bar{3}$ and $P4/mbm$ phases also shows a clear preference for $P4/mbm$ at all temperatures, with an R_w of 7.28 % for $P4/mbm$ and 7.83 % for $Im\bar{3}$ at 293 K, respectively (Fig S3 in the SI). This supports the consensus that this distortion is the one first reached on the application of moderate pressure. However, it is surprising that even at high temperatures, such a pronounced anisotropic signature of this OPD is evident. We investigate the origin of this anisotropy below.

For small mode amplitudes (< 0.5 Å) of the M_2^+ $(a; 0; 0)$ and $(a; a; a)$ OPDs, such as we observe here, the distortions give rise to an almost identical volume strain in our DFT calculations (Fig 6 (a)). The two distortions are also found to be equally soft in energy over the range of amplitudes we expect to sample dynamically (Fig 6 (b&c)), hence these calculations do not explain the observed anisotropy with respect to the dynamic displacements transforming as M_2^+. Possible strain coupling is accounted for in the DFT calculations since the lattice parameters of each distorted structure were relaxed during the energy calculations. The only factor not accounted for by the DFT is that the M_2^+ $(a; a; a)$ OPD can couple to displacements that transform as the M_1^+ irrep, but this would only serve to decrease the energy of the $Im\bar{3}$ phase further, and so cannot explain why we observe the $P4/mbm$ distortion dynamically at ambient pressure. Since the ground state DFT calculations fail to account for the anisotropy in the OPDs, we must consider these effects to be either due to entropy or anharmonic couplings between phonons. We discount the latter proposal as the anisotropy persists even down to
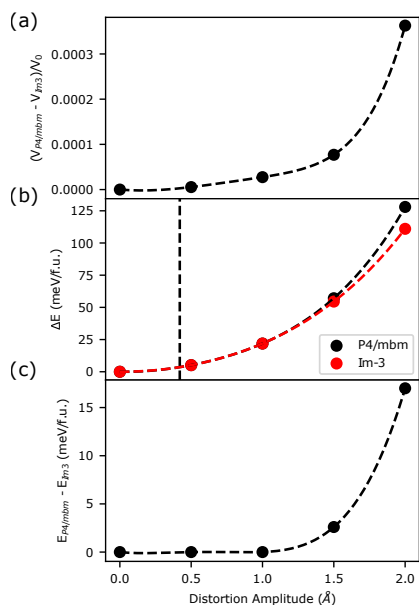
Figure 6. (a) The volume difference (normalised to the volume of the undistorted structure), (b) the energy increase and (c) the energy difference for M_2^+ OPDs with $P4/mbm$ and $Im\bar{3}$ symmetries for increasing $2 \times 2 \times 2$ supercell-normalised mode amplitudes. These values are obtained using DFT calculations. Lattice parameters were relaxed, respecting the space group symmetry. The vertical line shows the mode amplitude for M_2^+ at 293 K (Fig 3) The energy difference between the two is plotted (c). The lines shown in (b) are 4th order polynomial fits to the data points shown. The line in (c) is the difference between the fits in (b). The line in (a) is shown as a guide to the eye.

the lowest temperature, where we have shown that any dynamic deviations are small and are accounted for almost exclusively by the M_2^+ RUM (Fig 4). Hence, in the following paragraph, we explore the prior suggestion that entropy might dictate the anisotropy of the dynamic fluctuations.

By virtue of our experimental observation of the anisotropy of these modes, we have already shown them to be anharmonic in nature. For the OPD M_2^+ $(a; 0; 0)$ with $P4/mbm$ symmetry, the structural fluctuation, taken in the static limit, has additional degrees of freedom that may be realised as dynamic tilts in the directions perpendicular to the spontaneously condensed tilt,

corresponding to a line in the phonon dispersion curve between the R and M points in aristotypical perovskite symmetry. The $Im\bar{3}$ structure has tilts along all three pseudo-cubic axes, and consequently will have no additional degrees of freedom of this manner. This leads to the $P4/mbm$ phase, or indeed an anharmonic distortion of this character, having the greater vibrational entropy of the two. This means that it is favoured over other OPDs for the smaller distortion amplitudes that are realised at lower pressures or during dynamic, anharmonic fluctuations of the system.

The above scenario implies that we should be sensitive in our PDF analysis to low amplitude, harmonic distortions of RUM character that are orthogonal to the dominant anharmonic one. Indeed, we can see a signature of this from the spherical polar coordinate plots of the M_2^+ OPD at 600 K, in the form of "rings" around the $(a; 0; 0)$ OPD (Fig 5 (b)), corresponding to smaller amplitude tilts about the axes orthogonal to the propagation vector of the anharmonic RUM. This is further supported by a fit to the 600 K PDF data with a two-phase model. Each phase contained a large amplitude (0.6 Å) M_2^+ $(a; 0; 0)$ distortion, the "anharmonic part", and one smaller amplitude distortion (< 0.3 Å) of M_2^+ $(0; b; c)$ or R_5^- $(0; b; c)$ to mimic deviation in the data due to the line of mainly dispersionless harmonic RUMs running from k = [1/2 1/2 0] to [1/2 1/2 1/2]. All non-zero ratios of in-phase to out-of-phase tilts resulted in a slight improvement to the fit compared to an all in-phase model (Fig S6 in the SI).

The importance of entropy in determining the sequence of soft mode phase transitions in Ruddlesden-Popper perovskites has been highlighted by us recently[44]. In this instance, we discussed how the layering in this structure effectively affords phonon modes with an octahedral tilt character (RUMs about axes perpendicular to the layering axis) a greater vibrational entropy than those with an octahedral rotation character (about the layering axis). The sequence of temperature induced soft mode phase transitions we observed in these compounds were consistent with the idea that the entropic cost of ordering a tilt is higher than that of ordering a rotation. Given that the change in entropy associated with the ordering of a single mode is in principle vanishingly small, it is maybe surprising that the phase transition pathway is dictated in this manner. However, it is the associated renormalisation of phonon modes with RUM and quasi-RUM character, occupying a significant volume in reciprocal space, that provides the non-vanishing contribution to the Gibbs free energy, directing the soft mode transition pathway. Our present results tentatively go beyond these ideas in two respects. Firstly, ReO_3 is not a layered perovskite, so there is no distinction between octahedral tilts and rotations. However, it is clear that the same arguments about entropy and phonon renormalisation apply when considering the ordering of tilts about one axis compared to tilts about three. Secondly, our results imply that the anisotropic character of the phonon mode

is essentially determined by the entropic cost of the anharmonic fluctuation itself, even without this fluctuation reaching the static limit required to initiate a soft mode phase transition.

In conclusion, a symmetry-motivated analysis of the pair distribution functions of ReO_3 has shown that the presence of a rigid unit mode allows this material to exhibit NTE, but a lack of flexibility of the structure limits the magnitude and extent of the NTE behaviour. The rigid unit mode has been shown to be anisotropic, displaying a clear preference for an $(a; 0; 0)$ order parameter direction, even at elevated temperatures, which is consistent with the $P4/mbm$ space group the structure achieves after its phase transition with pressure. We tentatively suggest that the anisotropy we observe in the tilt direction of the M_2^+ RUM is effectively determined by the

entropic cost of the fluctuation itself.

* a.e.phillips@qmul.ac.uk
† m.senn@warwick.ac.uk

[1] Paul J. Attfield, "Mechanisms and materials for NTE," Front. Chem. **6**, 371 (2018).

[2] Cora Lind, "Two Decades of Negative Thermal Expansion Research: Where do we stand?" Materials **5**, 1125–1154 (2012).

[3] G D Barrera, J A O Bruno, T H K Barron, and N L Allan, "Negative Thermal Expansion," J. Phys. Condens. Matter **17**, 217–252 (2005).

[4] Martin T Dove and Hong Fang, "Negative thermal expansion and associated anomalous physical properties: Review of the lattice dynamics theoretical foundation," Rep. Prog. Phys. **79**, 066503 (2016).

[5] Brendan J. Kennedy, Yoshiki Kubota, and Kenichi Kato, "Negative thermal expansion and phase transition behaviour in Ag 2O," Solid State Commun. **136**, 177–180 (2005).

[6] Walter Tiano, Monica Dapiaggi, and Gilberto Artioli, "Thermal expansion in cuprite-type structures from 10 K to decomposition temperature: Cu2O and Ag2O," J. Appl. Crystallogr. **36**, 1461–1463 (2003).

[7] Hong Fang, Martin T Dove, Leila H.N. Rimmer, and Alston J Misquitta, "Simulation study of pressure and temperature dependence of the negative thermal expansion in Zn(CN)2," Phys. Rev. B **88**, 104306 (2013).

[8] Qilong Gao, Naike Shi, Qiang Sun, Andrea Sanson, Ruggero Milazzo, Alberto Carnera, He Zhu, Saul H. Lapidus, Yang Ren, Qingzhen Huang, Jun Chen, and Xianran Xing, "Low-Frequency Phonon Driven Negative Thermal Expansion in Cubic GaFe(CN)6 Prussian Blue Analogues," Inorg. Chem. **57**, 10918–10924 (2018).

[9] Volker Heine, Patrick R. L. Welche, and Martin T. Dove, "Geometrical Origin and Theory of Negative Thermal Expansion in Framework Structures," J. Am. Ceram. Soc. **82**, 1793–1802 (1999).

[10] J. S.O. Evans, T A Mary, T Vogt, M A Subramanian, and A W Sleight, "Negative thermal expansion in ZrW2O8and HfW 2O8," Chem. Mater. **8**, 2809–2823 (1996).

[11] M. T. Dove, P. R. L. Welche, and V. Heine, "Negative thermal expansion in beta-quartz," Phys. Chem. Miner. **26**, 63–77 (1998).

[12] M. S. Senn, A. Bombardi, C. A. Murray, C. Vecchini, A. Scherillo, X. Luo, and S. W. Cheong, "Negative thermal expansion in hybrid improper ferroelectric Ruddlesden-popper Perovskites by symmetry trapping," Phys. Rev. Lett. **114**, 23–27 (2015).

[13] Tapan Chatterji, Paul F. Henry, R. Mittal, and S. L. Chaplot, "Negative thermal expansion of ReO3: Neutron diffraction experiments and dynamical lattice calculations," Phys. Rev. B **78**, 134105 (2008).

[14] Tapan Chatterji, Thomas C. Hansen, Michela Brunelli, and Paul F. Henry, "Negative thermal expansion of ReO3 in the extended temperature range," Appl. Phys. Lett. **94**, 3–6 (2009).

[15] Benjamin K Greve, Kenneth L Martin, Peter L Lee, Peter J Chupas, Karena W Chapman, and Angus P Wilkinson, "Pronounced negative thermal expansion from a simple structure: Cubic ScF3," J. Am. Chem. Soc. **132**, 15496–15498 (2010).

[16] Efrain E. Rodriguez, Anna Llobet, Thomas Proffen, Brent C. Melot, Ram Seshadri, Peter B. Littlewood, and Anthony K. Cheetham, "The role of static disorder in negative thermal expansion in ReO3," J. Appl. Phys. **105** (2009), 10.1063/1.3120783.

[17] George Rouschias, "Recent advances in the chemistry of Rhenium," Chem. Rev. **74**, 531–566 (1974).

[18] J. D. Axe, Y. Fujii, B. Batlogg, M. Greenblatt, and S. Di Gregorio, "Neutron scattering study of the pressure-induced phase transformation in ReO3," Phys. Rev. B **31**, 663–667 (1985).

[19] J. E. Jorgensen, J. D. Jorgensen, B. Batlogg, J. P. Remeika, and J. D. Axe, "Order parameter and critical exponent for the pressure-induced phase transitions in ReO3," Phys. Rev. B **33**, 4793–4798 (1986).

[20] Tapan Chatterji and G. J. McIntyre, "Pressure-induced structural phase transition in ReO3," Solid State Commun. **139**, 12–15 (2006).

[21] Yaming Liu, Niu Zhang, Yu Jia, Qiang Sun, and Mingju Chao, "Phonon softening induced cubic-to-tetragonal phase transition in ReO3," Phys. Lett. A **379**, 2756–2760 (2015).

[22] K. S. Aleksandrov, V. N. Voronov, A. N. Vtyurin, A. S. Krylov, M. S. Molokeev, M. S. Pavlovski, S. V. Goryanov,

A. Yu Likhacheva, and A. I. Ancharov, "Pressure-induced phase transition in the cubic ScF3 crystal," Phys. Solid State **51**, 810–816 (2009).

[23] T. A. Bird, J. Woodland-Scott, L. Hu, M. T. Wharmby, J. Chen, A. L. Goodwin, and M. S. Senn, "Anharmonicity and scissoring modes in the negative thermal expansion materials ScF 3 and CaZrF 6," Phys. Rev. B **101**, 064306 (2020).

[24] Martin T. Dove, Juan Du, Zhongsheng Wei, David A. Keen, Matthew G. Tucker, and Anthony E. Phillips, "Quantitative understanding of negative thermal expansion in scandium trifluoride from neutron total scattering measurements," Phys. Rev. B **102**, 094105 (2020).

[25] Martin T. Dove, "Flexibility of network materials and the Rigid Unit Mode model: A personal perspective," Phil. Trans. R. Soc. A **377**, 1–18 (2019).

[26] Joseph T. Schick and Andrew M. Rappe, "Classical model of negative thermal expansion in solids with expanding bonds," Phys. Rev. B **93**, 214304 (2016).

[27] R. I. Smith, S. Hull, M. G. Tucker, H. Y. Playford, D. J. McPhail, S. P. Waller, and S. T. Norberg, "The upgraded Polaris powder diffractometer at the ISIS neutron source," Rev. Sci. Instrum. **90**, 115101–115113 (2019).

[28] O. Arnold, J. C. Bilheux, J. M. Borreguero, A. Buts, S. I. Campbell, L. Chapon, M. Doucet, N. Draper, R. Ferraz Leal, M. A. Gigg, V. E. Lynch, A. Markvardsen, D. J. Mikkelson, R. L. Mikkelson, R. Miller, K. Palmen, P. Parker, G. Passos, T. G. Perring, P. F. Peterson, S. Ren, M. A. Reuter, A. T. Savici, J. W. Taylor, R. J. Taylor, R. Tolchenov, W. Zhou, and J. Zikovsky, "Mantid - Data analysis and visualization package for neutron scattering and μ SR experiments," Nucl. Instrum. Methods **764**, 156–166 (2014).

[29] Brian H. Toby, "EXPGUI, a graphical user interface for GSAS," J. Appl. Crystallogr. **34**, 210–213 (2001).

[30] A.C. Larson and R. B Von Dreele, *General Structure Analysis System (GSAS)*, Tech. Rep. (Los Alamos National Laboratory, 2000).

[31] S. E. McLain, D. T. Bowron, A. C. Hannon, and A. K. Soper, "GUDRUN, a computer program developed for analysis of neutron diffraction data, Chilton: ISIS Facility, Rutherford Appleton Laboratory," (2012).

[32] Note1, The total scattering structure factor, $F(Q)$, is related to the scattering function $S(Q)$ by the relation $S(Q) - 1 = F(Q)/\left(\sum_{i=1}^{n} c_i \bar{b}_i\right)^2$.

[33] David A. Keen, "A comparison of various commonly used correlation functions for describing total scattering," J. Appl. Crystallogr. **34**, 172–177 (2001).

[34] Branton J Campbell, Harold T Stokes, David E Tanner, and Dorian M Hatch, "ISODISPLACE: A web-based tool for exploring structural distortions," J. Appl. Crystallogr. **39**, 607–614 (2006).

[35] John S.O. Evans, "Advanced input files & parametric quantitative analysis using topas," Mater. Sci. Forum **651**, 1–9 (2010).

[36] A. A. Coelho, P. A. Chater, and A. Kern, "Fast synthesis and refinement of the atomic pair distribution function," J. Appl. Crystallogr. **48**, 869–875 (2015).

[37] G. Kresse and J. Hafner, "Ab initio molecular-dynamics simulation of the liquid-metalamorphous- semiconductor transition in germanium," Phys. Rev. B **49**, 14251–14269 (1994).

[38] G. Kresse and J. Furthmüller, "Efficient iterative schemes for ab initio total-energy calculations using a plane-wave basis set," Phys. Rev. B **54**, 11169 – 11186 (1996).

[39] G. Kresse and J. Furthmüller, "Efficiency of ab-initio total energy calculations for metals and semiconductors using a plane-wave basis set," Comput. Mater. Sci. **6**, 15–50 (1996).

[40] G. Kresse and J. Hafner, "Ab initio molecular dynamics for liquid metals," J. Non-Cryst. Solids **47**, 558–561 (1993).

[41] John P. Perdew, Adrienn Ruzsinszky, Gábor I. Csonka, Oleg A. Vydrov, Gustavo E. Scuseria, Lucian A. Constantin, Xiaolan Zhou, and Kieron Burke, "Restoring the density-gradient expansion for exchange in solids and surfaces," Phys. Rev. Lett. **100**, 1–4 (2008).

[42] P E Blochl, "Projector augmented-wave method," Phys. Rev. B **50**, 17953–17979 (1994).

[43] Note2, It is important to note here that the phase fractions we discuss simply reflect an approximate measure of the proportion of the motion of O anions arising from the two different distortions. We do not believe that the two distortions exist in distinct phases within the material.

[44] Fernando Pomiro, Chris Ablitt, Nicholas C. Bristowe, Arash A. Mostofi, Choongjae Won, Sang Wook Cheong, and Mark S. Senn, "From first- To second-order phase transitions in hybrid improper ferroelectrics through entropy stabilization," Phys. Rev. B **102**, 014101 (2020).

[45] Martin T. Dove, "DOI: 10.5286/ISIS.E.RB1620329,".

Chapter 5

Large dynamic scissoring mode displacements coupled to band gap opening in Hybrid Perovskites

Large dynamic scissoring mode displacements coupled to band gap opening in Hybrid Perovskites

Tobias A. Bird,[1] Jungshen Chen,[2] Manila Songvilay,[3] Chris Stock,[4]
Michael T. Wharmby,[5] Nicholas C. Bristowe,[6] and Mark S. Senn[1, *]

[1]*Department of Chemistry, University of Warwick,*
Gibbet Hill, Coventry, CV4 7AL,United Kingdom
[2]*Nano-Science Center & Department of Chemistry,*
University of Copenhagen, Universitetsparken 5, 2100 Copenhagen, Denmark
[3]*Institut Néel, CNRS and Université Grenoble Alpes, 38000 Grenoble, France*
[4]*School of Physics and Astronomy, University of Edinburgh, Edinburgh EH9 3FD, United Kingdom*
[5]*Deutsches Elektronen-Synchrotron (DESY), Notkestr. 85, 22607 Hamburg, Germany*
[6]*Centre for Materials Physics, Durham University,*
South Road, Durham DH1 3LE, United Kingdom
(Dated: August 12, 2021)

Hybrid perovskites are a rapidly growing research area, having reached photovoltaic power conversion efficiencies of over 25 %. We apply a symmetry-motivated analysis method to analyse X-ray pair distribution function data of the cubic phases of the hybrid perovskites $MAPbX_3$ ($X =$ I, Br, Cl). We demonstrate that the local structure of the inorganic components of $MAPbX_3$ ($X =$ I, Br, Cl) are dominated by scissoring type deformations of the PbX_6 octahedra. We find these modes to have a larger amplitude than equivalent distortions in the A-site deficient perovskite ScF_3 and demonstrate that they show a significant departure from the harmonic approximation. Calculations performed on an all-inorganic analogue to the hybrid perovskite, $FrPbBr_3$, show that the large amplitudes of the scissoring modes are coupled to an opening of the electronic band gap. Finally, we use density functional theory calculations to show that the organic MA cations reorientate to accomodate the large amplitude scissoring modes.

I. INTRODUCTION

Molecular perovskites, also known as hybrid perovskites, are a fast growing research area in photovoltaics, due to their low cost to make and rapid increase in efficiency (from 3.9 % in 2009[1] to > 25 % today[2–4]). These materials have the general structure and chemical formula of traditional perovskites (ABX_3), but where they differ is that the A site cation is organic. The most frequently studied of this class of materials are the methylammonium (MA) lead halides, which have the general formula $CH_3NH_3PbX_3$ ($X =$ I, Br, Cl), commonly abbreviated to $MAPbX_3$. In addition to their high conversion efficiency, this class of hybrid perovskites have other desirable photovoltaic properties, such as long charge carrier lifetimes[5], mobility[6] and diffusion lengths[7], a high absorption coefficient[8], and a direct band gap[1]. These properties couple together to create a device that has a high density of charge carriers with a strong barrier against recombination, all whilst needing much less material than traditional solar cell materials, and without the need for a high energy input manufacturing process[9].

Whilst perovskite oxides are a well studied class of materials due to the wide range of desirable properties exhibited by them, less is understood about the structure-property relationship in halide perovskites, particularly the hybrid perovskite family. Having a methylammonium ion rather than a metal ion at the A site results in the A site possessing an electric dipole moment rather than a point charge, so the dynamics of these ions are the focus of a lot of research in these hybrid perovskites. In the higher temperature tetragonal and cubic phases, the alignment of the ions appears to be disordered[10–13], however they could form small domains below the length scale required for coherent diffraction where the molecules are aligned. The dynamics of their rotations, and any local order, could have a large contribution to the properties of the material. For example, the interaction between phonons and the rotational degrees of freedom of the MA cations has been shown to have an impact on thermal conductivity[14]. The changes in dynamics are thought to be closely linked to the structural changes of the material with temperature, and it is still unknown how the dynamics affect the properties of this material as a photovoltaic. Another question that has still not been fully solved is whether the configuration of the MA cations lead to this class of materials being ferroelectric[10,15–17].

Use of X-ray single crystal and powder diffraction has led to a good understanding of the different structural phases of these materials. Similarly to a large number of perovskites, all of the single-halide $MAPbX_3$ materials have cubic symmetry at high temperatures and undergo symmetry-lowering phase transitions to tetragonal and orthorhombic structures at lower temperatures[18]. Most experimental studies agree that there are 3 structural phases for $MAPbI_3$ and $MAPbCl_3$, however there is a 4th phase for $MAPbBr_3$ which is preferred for a small temperature range (*ca.* 150-155 K), commonly thought to be an incommensurate phase[19]. In the cubic phase, the MA cation is thought be fully disordered, with recent advances made using techniques such as NMR and

quasi-elastic neutron scattering showing that the MA cation is close to having the orientational freedom of a free MA cation[20,21]. As the inorganic framework undergoes structural phase transitions, lowering the average symmetry from cubic $Pm\bar{3}m$, the orientational freedom of the MA cation is restricted, becoming fully ordered in the orthorhombic phases[12,22]. This shows that the organic molecular and inorganic framework dynamics in MAPbX$_3$ are inherently linked[23,24]. In addition to experimental studies, computational methods have seen a lot of use in this, and other, areas of research in hybrid perovskites[25–29]. Both classical molecular dynamics and DFT simulations have demonstrated a link between the different phases of MAPbI$_3$ and the preferred orientations of the MA cations[30]. Work from Quarti *et al* has demonstrated that the configuration of the MA cations has a significant effect on the properties of the material, such as its electronic band structure[31,32]. This underlines why it is important to fully understand the structure-property relationship in these materials. Despite the knowledge that the organic molecular and inorganic framework dynamics are linked *via* hydrogen bonding interactions, it is currently unclear how this interaction affects the dynamics as a whole.

The bands forming the top of the valence bands and the bottom of the conduction band in the electronic structure of the methylammonium lead halides will be dominated by Pb and X (X = I, Br, Cl) electrons[24,33]. Therefore, regardless of the role of the MA cation in stabilising particular distortions, it is necessary to establish good models for the dynamic distortions in the PbX$_3$ framework. In this work, we aim to probe the dynamics of the inorganic framework of the cubic phases of the three single-halide MAPbX$_3$ materials. We have recently demonstrated how by using a symmetry motivated approach to analysing PDF data we can gain extra information on disorder and dynamics within a system. Our study on BaTiO$_3$ has shown that this method is very sensitive to primary order parameters and is a powerful tool to analyse order-disorder phase transitions[34]. Both this study and our more recent work on the negative thermal expansion materials ScF$_3$ and CaZrF$_6$ has demonstrated that this method is also sensitive to soft phonon modes and has also revealed substantial deviations from the crystallographic average structure in these materials[35]. Here, we use X-ray total scattering data, which is much more sensitive to the inorganic framework than the molecular cations, to probe the characters of the low lying excitations of the cubic phases of the methylammonium lead halides.

II. EXPERIMENTAL DETAILS AND DATA ANALYSIS

MAPbI$_3$ was prepared using the inverse temperature crystallisation method[36]. Briefly, equal molar amounts of MAI and PbI$_2$ were dissolved in a solvent
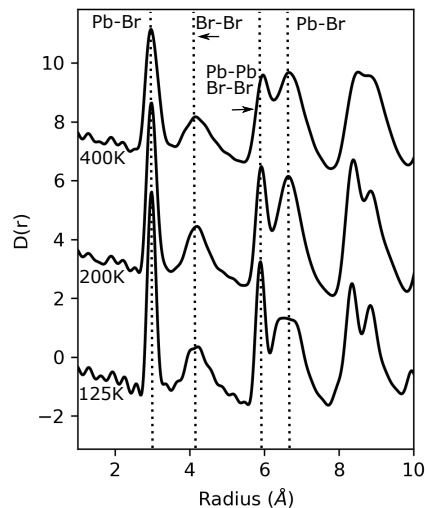

Figure 1. Pair distribution functions of MAPbBr$_3$ are shown in three different phases (orthorhomic, tetragonal and cubic, shown top to bottom). Each PDF is shown with a offset of 4 between them. Similar plots for X = I and Cl are given in the SI.

(γ-butyrolactone) at room temperature. Then the obtained MAPbI$_3$ solution was heated to 110 °C for the crystal growth. Powder samples of MAPbBr$_3$ were prepared by the reaction of stoichiometric amounts of lead acetate and methylamine hydrobromide in hydrobromic acid. The excess acid was then evaporated to leave an orange colored product which was washed with diethyl ether. Powder samples of MAPbCl$_3$ were prepared out of a solution of methylamine hydrochloride and lead acetate dissolved in hydrochloric acid. An excess of an approximately 8-10 molar ratio of methylamine hydrochloride was required to obtain these phase pure samples. The resulting powder was washed with diethyl ether.

For MAPbBr$_3$, synchrotron radiation X-ray total scattering experiments were conducted at the synchrotron facility PETRA III (beamline P02.1[37]) at DESY, Hamburg. A wavelength $\lambda = 0.2070$ Å was used to collect data. Data were collected at temperatures of 125, 140, 147, 152 K and at intervals of 25 K from 175 to 450 K.

For MAPbI$_3$ and MAPbCl$_3$, Synchrotron radiation X-ray total scattering experiments were conducted at the synchrotron facility Diamond Light Source (beamline I15-1). A wavelength of $\lambda = 0.161\,669$ Å was used to collect data. Data were collected at 20 K intervals over the temperature ranges 100 - 460 K (MAPbCl$_3$) and 100
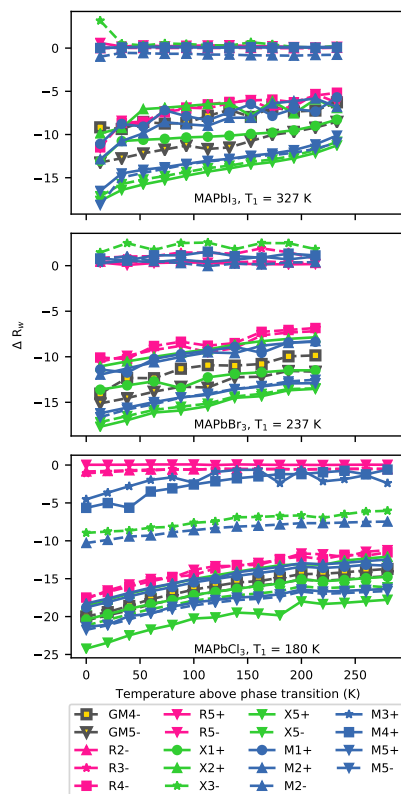
Figure 2. For each compound, the best individual fitting statistic is plotted for each irrep at each temperature. The R-factor is shown relative to the R-factor for the refinement with no symmetry adapted displacement modes active in the refinement, and the temperature shown is relative to the cubic phase transition as reported in the literature. The cubic transition temperature for each compound is indicated on the plot. The irreps are labelled as follows: colour denotes the k-point of the irrep, with blue referring to the M-point, green to X, pink to R and yellow to Γ; marker shape denotes the irrep number, with a circle referring to 1, an upward-pointed triangle to 2, a star to 3, a square to 4 and a downward-pointed triangle to 5; linestyle denotes the parity of the irrep, with a solid line referring to a "+" irrep, and a dashed line referring to a "-" irrep.

- 560 K (MAPbI$_3$).

The obtained 2D images were masked and radially integrated using the DAWN[38] software. $G(r)$ and $D(r)$ functions were computed using GudrunX[39], using Q_{max} values of 21, 30 and 28 Å^{-1} for MAPbBr$_3$, MAPbCl$_3$ and MAPbI$_3$ respectively. GudrunX was also used to perform background subtraction, sample absorption and fluorescence corrections.

Analysis of the pair distribution functions was carried out using the symmetry-adapted PDF analysis (SAPA) method described in ref. 32. For each sample, a $2 \times 2 \times 2$ $P1$ supercell of the $Pm\bar{3}m$ aristotype PbX$_3$ with Pb at (0.5, 0.5, 0.5) and X at (0.5, 0.5, 0) was generated and parameterised in terms of symmetry adapted displacements using the ISODISTORT software[40]. The generated mode listings were output in .cif format and then converted to the .inp format of the TOPAS Academic software v6 using the Jedit macros[41]. In total, there were 96 modes which transformed according to one of 19 irreducible representations. These supercells were generated without the organic A-site cation included, since the contribution of pairs involving the organic components of the structure will have a negligible contribution to the overall PDF due to their comparitively weak scattering power for X-rays. This lack of sensitivity of X-ray total scattering to the organic elements of hybrid perovskites can be seen by comparing recent publications by Malavasi *et al*[42–44]. For each irreducible representation (irrep) at each temperature, refinements of the corresponding modes were started from random starting mode amplitudes. This was repeated 500 times. For all samples, the refinements were carried out with a fitting range of 1.7 to 20 Å. Refinements were also tested using a fitting range with a maximum of 10 Å and found to be broadly similar.

The DFT calculations were performed using the Vienna Ab Initio Simulation Package (VASP)[45–48], version 5.4.4. We employed the optB86b-vdW exchange correlation potential[49] which includes VdW corrections previously found to suit hybrid perovskites[24]. Projector augmented-wave (PAW) pseudopotentials[46,50] were utilised, as supplied within the VASP package. A plane wave basis set with a 1100 eV energy cutoff and a $4 \times 4 \times 4$ Monkhorst-Pack k-point mesh with respect to the parent cubic primitive cell (scaled accordingly for other supercells) were found suitable. The energy landscape of the various modes in the hybrid system were studied by fixing the halide framework while allowing for Pb and MA to relax until the forces were less than 5 meV/Å. Results were compared with FrPbBr$_3$, which we used as a hypothetical inorganic analogue to the hybrid perovskite, since Fr best matches the ionic radii of MA[24].

III. RESULTS AND DISCUSSION

A key aspect of the local structure of the MAPbX_3 ($X=$ I, Br, Cl) family of hybrid perovskites is that the first four peaks of the inorganic component of the PDF do
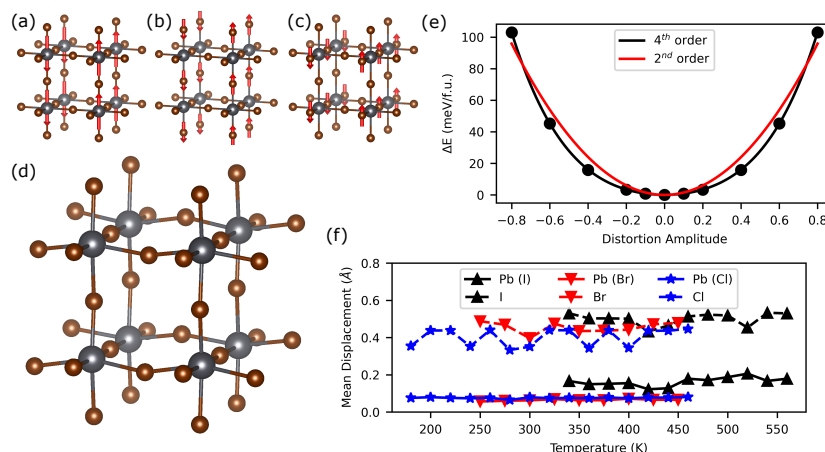
Figure 3. (a-c) A breakdown of the atomic basis that spans the X_5^+ irrep. Shown in (d) is the structure resulting from a refinement of the $Pnma$ order parameter direction of the X_5^+ irrep. (e) Mode energies with varying distortion mode amplitude for the $Pnma$ order parameter direction of FrPbBr$_3$. Harmonic (2nd order) and anharmonic (4th order) fits to the potential well are shown. (f) Mean displacement values for the general X_5^+ order parameter direction.

not change much beyond that expected for simply changing the temperature, i.e a change in peak width corresponding to a change in thermal energy, and a change in peak position corresponding to thermal expansion. For MAPbBr$_3$ (Fig. 1) and MAPbCl$_3$, the peaks stay the same from the low temperature orthorhombic phase into the high temperature cubic phase[42–44]. For MAPbI$_3$, there is a slight change upon the transition between the tetragonal and orthorhombic phases, but the peaks from the tetragonal phase persist in the cubic phase[51] (see SI). This has been taken to imply that the cubic phase consists of local symmetry-broken domains and there has been recent work to support this hypothesis[51]. This would suggest that the distortions most responsible for the local structure should be the rigid-unit modes (RUMs) that drive these phase transitions.

To gain a more robust understanding of the local structure of MAPbX_3 (X = I, Br, Cl), we perform a symmetry-adapted PDF analysis (SAPA)[34,35] to elucidate the character of the dominant lattice dynamics associated with the inorganic cage. We note that we are insensitive to MA orientation and displacement modes in the present X-ray PDF study, and so no attempt is made to model these against the experimental data. The symmetry-adapted displacements which show the most improvement in the R_w for the models against the PDFs for all compounds and all temperatures are those which transform according to irreps that permit a scissoring motion

of the X anions, i.e., the Br–Pb–Br bond angles are distorted away from 90° but the Pb–Br bond lengths remain undistorted. This result of the SAPA analysis does not imply that the RUMs are high energy modes, it simply means that the majority of the motion of the halide anions arise from these scissoring modes. This is supported by competetive two-phase refinements of the PDFs, in which we allow the X_5^+ displacements to refine in one phase and the displacements for one of the RUMs (R_5^- or M_2^+) in the other. These refinements show a preference for scissoring modes compared to the RUMs for all 3 samples, as evident from the refined scale factors of the two phases which show an approximate scissoring:rotation ratio of 2.3:1 (see SI for more details). For context, this ratio is approximately 4:1 in ScF$_3$, which is isostructural to the inorganic framework of MAPbX_3. The lower ratio compared to ScF$_3$ reflects a lower flexibility due to the presence of an A-site cation, which can interact with the inorganic framework via hydrogen bonding[23]. However, it is clear from our results that the majority of the halide anion motion still arises from scissoring-type deformations of the octahedra.

The above results are in line with a recent reverse Monte Carlo (RMC) analysis of neutron PDFs of MAPbI$_3$[52] between 10 and 400 K. This study demonstrates that a bending of the Pb-I-Pb bond angle dominates the local distortions of the PbI$_6$ octahedra. Our results show that the four best fitting modes all have

scissoring character, of which it is the X_5^+ (Fig 3 (c&d)) that performs best across all three compositions and temperatures. This could be due to the fact that there are more parameters for the X_5^+ irrep than the other three (18 modes transform as the X_5^+ irrep, compared to 12 for M_5^- and 6 for X_5^- and M_5^+), but the improvement could arise from the anti-polar Pb displacements that enter into the irrep X_5^+, although this is unlikely since they only have a small contribution to the overall displacements. The three distortions that span this irrep are shown in Fig 3. We find the amplitudes of these scissoring modes to be quite large; refinements of X_5^+ and X_5^- in the tetragonal phase of MAPbBr$_3$ resulted in supercell-normalised mode amplitudes of ≈ 1.35 Å. This is close in magnitude to the equivalent amplitude of the R_5^- distortion (≈ 1.65 Å) which is frozen into the structure in the tetragonal phase.

Given how large the local deviations are from the average structure, it is reasonable to assume they will have a substantial effect on the band structure. We used DFT calculations to investigate the impact that the scissoring modes could have on the electronic band structure of the hybrid perovskites. We chose to analyse MAPbBr$_3$, since it is cubic at room temperature where experimental band gap values have been reported, and to focus on the two X point modes that do the best job at describing the deviations away from local cubic symmetry, as evident in the PDF data. For a completely unrestrained order parameter direction transforming as X_5^+, there are a rather large number of degrees of freedom (18 in total), so, to make our results more robust, and to facilitate a direct comparison to X_5^-, we take results from refinements using higher symmetry OPDs with no more than 5 parameters. We use structures from refinements against our data with X_5^+ OPDs with $Pnma$ and $Cmcm$ symmetry ($(0, a; b, 0; 0, c)$ and $(0, a; b, b; a, 0)$ respectively) and the X_5^- OPD with $C2/c$ symmetry ($(a, b; c, -c; -b, -a)$) as input to our band structure calculations. For the two X_5^+ OPDs, only Br anion displacements were refined when generating the CIFs for the band structure calculations, although by symmetry, Pb displacements also enter into the irrep. For X_5^-, Pb displacements are forbidden by symmetry. We also sampled points of different overall distortion amplitude along the X_5^+ OPD with $Pnma$ symmetry and calculated the energy. These energy calculations were performed for the FrPbBr$_3$ structures used to calculate the band structure.

In the undistorted structure, the calculated band gap was 1.717 eV, which is slightly higher than other calculated band gaps for cubic MAPbBr$_3$ (1.64 eV[53]) at the same level of theory, and is direct. Previous work has shown that substitution of Fr for MA opens up the band gap slightly in orthorhombic MAPbI$_3$[24]. For each distortion, the band gap opens up significantly to values of 2.025, 2.138 and 2.162 eV for the $C2/c$, $Cmcm$ and $Pnma$ distortions with an amplitude of $0.8\times$ the maximum amplitude refined from PDF data for the X_5^+ distortions and $1.1\times$ the maximum amplitude for X_5^-, re-

spectively, and remains direct. These relative amplitudes were chosen so all 3 distortions were at similar mode amplitudes. These values are closer to the experimentally determined band gaps for MAPbBr$_3$ of ≈ 2.3 eV at room temperature[54], although this is likely due to a cancellation of errors. The distortions result in a reduced orbital overlap between Pb and Br p-orbitals, leading to a lower band curvature and therefore an increased effective mass in the distorted band structures (Fig 4 and SI). The mobility of polarons is inversely proportional to the electron band effective mass[55], and this increased effective mass in the distorted structures may explain the discrepancy between experimental and calculated values[56].

Spin-orbit coupling (SOC) interactions, which play a large role in systems involving Pb, have not been accounted for. Consequently, the exact shape of the electron bands and size of the band gap won't be accurate, since inclusion of SOC has been shown to lead to unconventional dispersion relations[57]. The effects from SOC on band gap size in halide perovskites tend to be canceled out by full treatment of electron Coulomb interactions beyond DFT[58,59]. Therefore, the trends we detect due to the different distortion modes will remain the same. In the two X_5^+ distortions, the degeneracy of the bands at the conduction band minimum (CBM) at the Γpoint are broken, leading to fewer available states at the CBM. Contrastingly, the X_5^+ $Pnma$ distortion appears to have the largest DOS at the valence band maximum due to the reduced bandwidth. Fluctuations in the band gap of hybrid perovskites due to their highly dynamic structure has been previously predicted[32], and is expected to assist the initial stages of charge separation. In addition, an increase of the band gap coinciding with a transverse displacement of I ions in MAPbI$_3$ due to an external strain field has been reported[33].

Our refinements against the PDF data show that all three modes have a large amplitude, with supercell-normalised mode amplitudes of 1.84, 1.82 and 1.36 Å for OPDs with $Pnma$, $Cmcm$ and $C2/c$ symmetries, respectively. These mode amplitudes correspond to maximum Br displacements of 0.486, 0.410 and 0.350 Å. Note that the refined distortions correspond to a time-averaged view of the structure, so these maximum Br displacements are a factor of $\sqrt{2}\times$ greater, in the harmonic approximation, than those found in the refined structures. As a consequence of their large amplitudes, the distortions would be expected to be anharmonic in nature, which is supported by the potential energy well we calculate for the X_5^+ $(0, a; b, 0; 0, c)$ OPD in FrPbBr$_3$ (Fig 3 (f)), which has a significant quartic component when fit with a 4th order polynomial fit ($\Delta E = 127x^4 + 79.7x^2$, where x is the distortion mode amplitude relative to its maximum value at 400 K). This breakdown in the harmonic approximation would then allow the scissoring modes of the inorganic framework to couple directly to the anharmonic modes that correspond to the organic cation dynamics[60,61]. Despite the presence of an A-site in these materials, the amplitude of these scissoring modes

are greater than those in ScF_3, suggesting the MA cations move to accomodate the large-amplitude modes. The implication of this, then, is that the band gap opening we detect as a response to the scissoring modes is likely influenced by the dynamics of the MA cations, although our refinements are only sensitive to the inorganic framework.

To investigate the above hypothesis, we consider the X_5^+ OPD with $Pnma$ symmetry. This breaks the equivalency of the $< 100 >$ directions and leads to two distinct A-site symmetries (see SI). Therefore, if the inorganic and organic dynamics are coupled together, we would expect to see the MA cations located at different points of the unit cell to respond differently to the distortion mode, to reflect the different local environments they would experience. To test this, we relaxed the MA cations from an initial anti-polar configuration with the C-N bonds aligned with the [1 0 0] direction, in a structure with a $0.8\times$ X_5^+ $(0, a; b, 0; 0, c)$ distortion (relative to the maximum amplitude at 400 K) frozen in. The MA cations showed significant reorientation, with the "edge" $((0.5, 0, 0)$ and equivalents) and "corner" $((0, 0, 0))$ cations rotating to include significant components along c. There is a split amongst the "face" cations, with two (at $(0.5, 0.5, 0)$ and $(0, 0.5, 0.5)$) rotating to include smaller components along the b- and c-axes. The remaining "face" cation and the cation located at the centre of the supercell both rotate to include a significant component along c and a smaller component along b. In all, there are 5 distinct C–N bond alignments, which may reflect the 5 distinct Br sites. In addition, all cations show a slight displacement from the high-symmetry-unique positions. Full details can be found in the SI. This demonstrates that the MA cations can rotate to accommodate the distortions of the inorganic framework, indicating that the dynamics of the two components of the structure may be linked. However, it is important to note that our calculations are effectively performed at 0 K, where the ground state is the fully ordered orthorhombic phase. It is quite possible that the configurational entropy associated with the MA orderings may effectively act to decouple these dynamics at higher temperatures in the cubic phase. Indeed, there is evidence to suggest the organic and inorganic dynamics are decoupled in MAPbCl$_3$[13]. Additionally, a similar computational result in CsPbBr$_3$ showing coupling between large amplitude distortions of the Br ions and head-to-head Cs motion[62] suggest this feature may not be exclusive to hybrid inorganic systems. We have also shown that acoustic phonon lifetimes for the all-inorganic CsPbBr$_3$ are very similar to those in MAPbCl$_3$[63], further supporting the idea that at high temperatures the MA rotational modes may have little effect on the lattice phonon modes.

There has been recent literature support for the idea that cubic halide perovskites, rather than being treated as a single repeating unit, should be thought of as a network of polymorphs showing different symmetry-lowering deformations of the average structure, such as varying degrees of octahedral tilting or differing amplitudes of
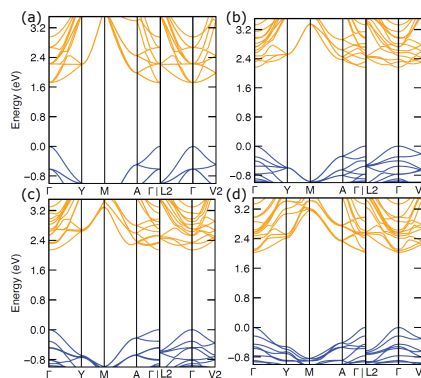

Figure 4. The calculated electronic band structure of FrPbBr$_3$ for the undistorted structure (a), the $Pnma$ and $Cmcm$ order parameter directions of the X_5^+ irrep (b and c, respectively) and the $C2/c$ order parameter direction of the $X5_5^-$ irrep (d). These figures were created using sumo[65]

B-site displacement[64]. Our work is broadly consistent with this picture. The sterochemical behaviour of the Pb cation, in conjunction with the coupling between organic cation and inorganic framework dynamics, is likely to have a large impact on the possible polymorphs the material exhibits within this hypothesis of the nature of the structure of halide perovskites.

In summary, we have shown that large scissoring modes of the halide ions describe the dominant deviations from the average structure in the cubic phases of the hybrid perovskites. These modes have a similar amplitude to those of the static RUMs below the phase transition temperature. These distortions have the effect of opening up the band gap of the electronic structure. In addition, we have shown that the organic cations can move to accomodate the distortions of the inorganic framework, suggesting the dynamics of the two components could be inherently linked, and that the inorganic lattice is likely to be significantly distorted from the average at a local level. These dynamic structures should be accounted for in simulations performed on the hybrid perovskites, since they can have a significant effect on the calculated properties.

The PDF data used in this study are available as a supporting dataset.

ACKNOWLEDGEMENTS

[*] m.senn@warwick.ac.uk

[1] Akihiro Kojima, Kenjiro Teshima, Yasuo Shirai, and Tsutomu Miyasaka, "Organometal Halide Perovskites as Visible- Light Sensitizers for Photovoltaic Cells," J. Am. Chem. Soc. **131**, 6050–6051 (2009).

[2] Martin A. Green, Anita Ho-Baillie, and Henry J. Snaith, "The emergence of perovskite solar cells," Nat. Photonics **8**, 506–514 (2014).

[3] Olga Malinkiewicz, Aswani Yella, Yong Hui Lee, Guillermo Mínguez Espallargas, Michael Graetzel, Mohammad K. Nazeeruddin, and Henk J. Bolink, "Perovskite solar cells employing organic charge-transport layers," Nat. Photonics **8**, 128–132 (2014).

[4] Giorgio Schileo and Giulia Grancini, "Halide perovskites: current issues and new strategies to push material and device stability," J. Phys.: Energy **2**, 021005 (2020).

[5] Christian Wehrenfennig, Giles E. Eperon, Michael B. Johnston, Henry J. Snaith, and Laura M. Herz, "High charge carrier mobilities and lifetimes in organolead trihalide perovskites," Adv. Mater. **26**, 1584–1589 (2014).

[6] Daming Zhao, Jonathan M. Skelton, Hongwei Hu, Chan La-o vorakiat, Jian-Xin Zhu, Rudolph A. Marcus, Maria-Elisabeth Michel-Beyerle, Yeng Ming Lam, Aron Walsh, and Elbert E. M. Chia, "Low-frequency optical phonon modes and carrier mobility in the halide perovskite CH$_3$NH$_3$PbBr$_3$ using terahertz time-domain spectroscopy," Appl. Phys. Lett. **111**, 201903 (2017).

[7] Guichuan Xing, Nripan Mathews, Shuangyong Sun, Swee Sien Lim, Yeng Ming Lam, Michael Grätzel, Subodh Mhaisalkar, and Tze Chien Sum, "Long-range balanced electron- and hole-transport lengths in organic-inorganic CH3NH3PbI3." Science **342**, 344–347 (2013).

[8] Shuangyong Sun, Teddy Salim, Nripan Mathews, Martial Duchamp, Chris Boothroyd, Guichuan Xing, Tze Chien Sum, and Yeng Ming Lam, "The origin of high efficiency in low-temperature solution-processable bilayer organometal halide hybrid solar cells," Energy Environ. Sci. **7**, 399–407 (2014).

[9] Yu-Che Hsiao, Ting Wu, Mingxing Li, Qing Liu, Wei Qin, and Bin Hu, "Fundamental physics behind high-efficiency organo-metal halide perovskite solar cells," J. Mater. Chem. A **3**, 15372–15385 (2015).

[10] Aurélien M. A. Leguy, Alejandro R. Goñi, Jarvist M. Frost, Jonathan Skelton, Federico Brivio, Xabier Rodríguez-Martínez, Oliver J. Weber, Anuradha Pallipurath, M. Isabel Alonso, Mariano Campoy-Quiles, Mark T. Weller, Jenny Nelson, Aron Walsh, and Piers R. F. Barnes, "Dynamic disorder, phonon lifetimes, and the assignment of modes to the vibrational spectra of methylammonium lead halide perovskites," Phys. Chem. Chem. Phys. **18**, 27051–27066 (2016).

[11] Antoine Létoublon, Serge Paofai, Benoît Rufflé, Philippe Bourges, Bernard Hehlen, Thierry Michel, Claude Ecolivet, Olivier Durand, Stéphane Cordier, Claudine Katan, and Jacky Even, "Elastic Constants, Optical Phonons, and Molecular Relaxations in the High Temperature Plastic Phase of the CH3NH3PbBr3 Hybrid Perovskite," J. Phys. Chem. Lett. **7**, 3776–3784 (2016).

[12] K. L. Brown, S. F. Parker, I. Robles García, S. Mukhopadhyay, V. García Sakai, and C. Stock, "Molecular orientational melting within a lead-halide octahedron framework: The order-disorder transition in CH3NH3PbBr3," Phys. Rev. B **96**, 174111 (2017).

[13] M. Songvilay, Zitian Wang, V. Garcia Sakai, T. Guidi, M. Bari, Z. G. Ye, Guangyong Xu, K. L. Brown, P. M. Gehring, and C. Stock, "Decoupled molecular and inorganic framework dynamics in CH3NH3PbCl3," Phys. Rev. Mater. **3**, 125406 (2019).

[14] Andrea Pisoni, Jaćim Jaćimović, Osor S. Barišić, Massimo Spina, Richard Gaál, László Forró, and Endre Horváth, "Ultra-low thermal conductivity in organic-inorganic hybrid perovskite CH3NH3PbI3," J. Phys. Chem. Lett. **5**, 2488–2492 (2014).

[15] M Nadim Ferdous Hoque, Mengjin Yang, Zhen Li, Nazifah Islam, Xuan Pan, Kai Zhu, and Zhaoyang Fan, "Polarization and Dielectric Study of Methylammonium Lead Iodide Thin Film to Reveal its Nonferroelectric Nature under Solar Cell Operating Conditions," ACS Energy Lett. **1**, 142–149 (2016).

[16] Joanna Jankowska and Oleg V. Prezhdo, "Ferroelectric Alignment of Organic Cations Inhibits Nonradiative Electron-Hole Recombination in Hybrid Perovskites: Ab Initio Nonadiabatic Molecular Dynamics," J. Phys. Chem. Lett. **8**, 812–818 (2017).

[17] J. Breternitz, F. Lehmann, S. A. Barnett, H. Nowell, and S. Schorr, "Role of the Iodide–Methylammonium Interaction in the Ferroelectricity of CH3NH3PbI3," Angew. Chem. Int. Ed. **59**, 424–428 (2020).

[18] A. Poglitsch and D. Weber, "Dynamic disorder in methylammoniumtrihalogenoplumbates (II) observed by millimeter-wave spectroscopy," J. Chem. Phys. **87**, 6373–6378 (1987).

[19] Yinsheng Guo, Omer Yaffe, Daniel W. Paley, Alexander N. Beecher, Trevor D. Hull, Guilherme Szpak, Jonathan S. Owen, Louis E. Brus, and Marcos A. Pimenta, "Interplay between organic cations and inorganic framework and incommensurability in hybrid lead-halide perovskite CH3NH3PbBr3," Phys. Rev. Mater. **1**, 042401 (2017).

[20] Tianran Chen, Benjamin J. Foley, Bahar Ipek, Madhusudan Tyagi, John R. D. Copley, Craig M. Brown, Joshua J. Choi, and Seung-Hun Lee, "Rotational dynamics of organic cations in the CH$_3$NH$_3$PbI$_3$ perovskite," Phys. Chem. Chem. Phys. **17**, 31278–31286 (2015).

[21] Aurelien M.A. Leguy, Jarvist Moore Frost, Andrew P. McMahon, Victoria Garcia Sakai, W. Kochelmann, Chunhung Law, Xiaoe Li, Fabrizia Foglia, Aron Walsh, Brian C. O'Regan, Jenny Nelson, João T. Cabral, and Piers R.F. Barnes, "The dynamics of methylammonium ions in hybrid organic-inorganic perovskite solar cells," Nat. Commun. **6**, 7124 (2015).

[22] Mark T. Weller, Oliver J. Weber, Paul F. Henry, Antonietta M. Di Pumpo, and Thomas C. Hansen, "Complete structure and cation orientation in the perovskite photovoltaic methylammonium lead iodide between 100 and 352 K," Chem. Commun. **51**, 4180–4183 (2015).

[23] Jung Hoon Lee, Nicholas C. Bristowe, Paul D. Bristowe, and Anthony K. Cheetham, "Role of hydrogen-bonding and its interplay with octahedral tilting in CH3NH3PbI3," Chem. Commun. **51**, 6434–6437 (2015).

[24] Jung Hoon Lee, Nicholas C. Bristowe, June Ho Lee, Sung Hoon Lee, Paul D. Bristowe, Anthony K. Cheetham, and Hyun Myung Jang, "Resolving the Physical Origin of Octahedral Tilting in Halide Perovskites," Chem. Mater. **28**, 4259–4266 (2016).

[25] Nicholas Aristidou, Christopher Eames, Irene Sanchez-Molina, Xiangnan Bu, Jan Kosco, M. Saiful Islam, and Saif A. Haque, "Fast oxygen diffusion and iodide defects mediate oxygen-induced degradation of perovskite solar cells," Nat. Commun. **8**, 15218 (2017).

[26] Dibyajyoti Ghosh, Philip Walsh Atkins, M. Saiful Islam, Alison B. Walker, and Christopher Eames, "Good Vibrations: Locking of Octahedral Tilting in Mixed-Cation Iodide Perovskites for Solar Cells," ACS Energy Lett. **2**, 2424–2429 (2017).

[27] Christopher Eames, Jarvist M. Frost, Piers R.F. Barnes, Brian C. O'Regan, Aron Walsh, and M. Saiful Islam, "Ionic transport in hybrid lead iodide perovskite solar cells," Nat. Commun. **6**, 7497 (2015).

[28] Ana L. Montero-Alejo, E. Menéndez-Proupin, D. Hidalgo-Rojas, P. Palacios, P. Wahnón, and J. C. Conesa, "Modeling of Thermal Effect on the Electronic Properties of Photovoltaic Perovskite CH3NH3PbI3: The Case of Tetragonal Phase," J. Phys. Chem. C **120**, 7976–7986 (2016).

[29] Marcelo A. Carignano, Ali Kachmar, and Jürg Hutter, "Thermal Effects on CH 3 NH 3 PbI 3 Perovskite from Ab Initio Molecular Dynamics Simulations," J. Phys. Chem. C **119**, 8991–8997 (2015).

[30] A. Mattoni, A. Filippetti, M. I. Saba, and P. Delugas, "Methylammonium Rotational Dynamics in Lead Halide Perovskite by Classical Molecular Dynamics: The Role of Temperature," J. Phys. Chem. C **119**, 17421–17428 (2015).

[31] Claudio Quarti, Edoardo Mosconi, and Filippo De Angelis, "Interplay of orientational order and electronic structure in methylammonium lead iodide: Implications for solar cell operation," Chem. Mater. **26**, 6557–6569 (2014).

[32] Claudio Quarti, Edoardo Mosconi, and Filippo De Angelis, "Structural and electronic properties of organo-halide hybrid perovskites from ab initio molecular dynamics," Phys. Chem. Chem. Phys. **17**, 9394–9409 (2015).

[33] Le Zhang, Wei Geng, Chuan Jia Tong, Xueguang Chen, Tengfei Cao, and Mingyang Chen, "Strain induced electronic structure variation in methyl-ammonium lead iodide perovskite," Sci. Rep. **8**, 7760 (2018).

[34] M. S. Senn, D. A. Keen, T. C.A. Lucas, J. A. Hriljac, and A. L. Goodwin, "Emergence of Long-Range Order in BaTiO3 from Local Symmetry-Breaking Distortions," Phys. Rev. Lett. **116**, 207602 (2016).

[35] T. A. Bird, J. Woodland-Scott, L. Hu, M. T. Wharmby, J. Chen, A. L. Goodwin, and M. S. Senn, "Anharmonicity and scissoring modes in the negative thermal expansion materials ScF 3 and CaZrF 6," Phys. Rev. B **101**, 064306 (2020).

[36] Makhsud I. Saidaminov, Ahmed L. Abdelhady, Banavoth Murali, Erkki Alarousu, Victor M. Burlakov, Wei Peng, Ibrahim Dursun, Lingfei Wang, Yao He, Giacomo MacUlan, Alain Goriely, Tom Wu, Omar F. Mohammed, and Osman M. Bakr, "High-quality bulk hybrid perovskite single crystals within minutes by inverse temperature crystallization," Nat. Commun. **6**, 7586 (2015).

[37] Ann-Christin Dippel, Hanns-Peter Liermann, Jan Torben Delitz, Peter Walter, Horst Schulte-Schrepping, Oliver H. Seeck, and Hermann Franz, "Beamline P02.1 at PETRA III for high-resolution and high-energy powder diffraction," J. Synchrotron Radiat. **22**, 675–687 (2015).

[38] Mark Basham, Jacob Filik, Michael T. Wharmby, Peter C.Y. Chang, Baha El Kassaby, Matthew Gerring, Jun Aishima, Karl Levik, Bill C.A. Pulford, Irakli Sikharulidze, Duncan Sneddon, Matthew Webber, Sarnjeet S. Dhesi, Francesco Maccherozzi, Olof Svensson, Sandor Brockhauser, Gabor Náray, and Alun W. Ashton, "Data Analysis WorkbeNch (DAWN)," J. Synchrotron Radiat. **22**, 853–858 (2015).

[39] S. E. McLain, D. T. Bowron, A. C. Hannon, and A. K. Soper, "GUDRUN, a computer program developed for analysis of neutron diffraction data, Chilton: ISIS Facility, Rutherford Appleton Laboratory," (2012).

[40] Branton J Campbell, Harold T Stokes, David E Tanner, and Dorian M Hatch, "ISODISPLACE: A web-based tool for exploring structural distortions," J. Appl. Crystallogr. **39**, 607–614 (2006).

[41] John S.O. Evans, "Advanced input files & parametric quantitative analysis using topas," Mater. Sci. Forum **651**, 1–9 (2010).

[42] Katharine Page, Joan E. Siewenie, Paolo Quadrelli, and Lorenzo Malavasi, "Short-Range Order of Methylammonium and Persistence of Distortion at the Local Scale in MAPbBr3Hybrid Perovskite," Angew. Chem. Int. Ed. **55**, 14320–14324 (2016).

[43] Andrea Bernasconi and Lorenzo Malavasi, "Direct evidence of permanent octahedra distortion in MAPbBr3 hybrid perovskite," ACS Energy Lett. **2**, 863–868 (2017).

[44] Andrea Bernasconi, Katharine Page, Zhenbang Dai, Liang Z. Tan, Andrew M. Rappe, and Lorenzo Malavasi, "Ubiquitous Short-Range Distortion of Hybrid Perovskites and Hydrogen-Bonding Role: The MAPbCl 3 Case," J. Phys. Chem. C **122**, 28265–28272 (2018).

[45] G. Kresse and J. Hafner, "Ab initio molecular-dynamics simulation of the liquid-metalamorphous- semiconductor transition in germanium," Phys. Rev. B **49**, 14251–14269 (1994).

[46] G. Kresse and J. Furthmüller, "Efficient iterative schemes for ab initio total-energy calculations using a plane-wave basis set," Phys. Rev. B **54**, 11169 – 11186 (1996).

[47] G. Kresse and J. Furthmüller, "Efficiency of ab-initio total energy calculations for metals and semiconductors using a plane-wave basis set," Comput. Mater. Sci. **6**, 15–50 (1996).

[48] G. Kresse and J. Hafner, "Ab initio molecular dynamics for liquid metals," J. Non-Cryst. Solids **47**, 558–561 (1993).

[49] Jiří Klimes, David R. Bowler, and Angelos Michaelides, "Van der Waals density functionals applied to solids,"

Phys. Rev. B **83**, 195131 (2011).

[50] P E Blochl, "Projector augmented-wave method," Phys. Rev. B **50**, 17953–17979 (1994).

[51] Alexander N. Beecher, Octavi E. Semonin, Jonathan M. Skelton, Jarvist M. Frost, Maxwell W. Terban, Haowei Zhai, Ahmet Alatas, Jonathan S. Owen, Aron Walsh, and Simon J.L. Billinge, "Direct Observation of Dynamic Symmetry Breaking above Room Temperature in Methylammonium Lead Iodide Perovskite," ACS Energy Lett. **1**, 880–887 (2016).

[52] Jiaxun Liu, *Local structure of lead halide perovskites for photovoltaic applications*, Doctor of philosophy, Queen Mary, University of London (2017).

[53] Edoardo Mosconi, Paolo Umari, and Filippo De Angelis, "Electronic and optical properties of MAPbX3 perovskites (X = I, Br, Cl): A unified DFT and GW theoretical analysis," Phys. Chem. Chem. Phys. **18**, 27158–27164 (2016).

[54] G. C. Papavassiliou and I. B. Koutselas, "Structural, optical and related properties of some natural three- and lower-dimensional semiconductor systems," Synth. Met. **71**, 1713–1714 (1995).

[55] Jarvist Moore Frost, "Calculating polaron mobility in halide perovskites," Phys. Rev. B **96**, 195202 (2017).

[56] Mischa Bonn, Kiyoshi Miyata, Euan Hendry, and X. Y. Zhu, "Role of Dielectric Drag in Polaron Mobility in Lead Halide Perovskites," ACS Energy Lett. **2**, 2555–2562 (2017).

[57] Federico Brivio, Keith T. Butler, Aron Walsh, and Mark Van Schilfgaarde, "Relativistic quasiparticle self-consistent electronic structure of hybrid halide perovskite photovoltaic absorbers," Phys. Rev. B **89**, 155204 (2014).

[58] Jacky Even, Laurent Pedesseau, Jean Marc Jancu, and Claudine Katan, "Importance of spin-orbit coupling in hybrid organic/inorganic perovskites for photovoltaic applications," J. Phys. Chem. Lett. **4**, 2999–3005 (2013).

[59] Paolo Umari, Edoardo Mosconi, and Filippo De Angelis, "Relativistic GW calculations on CH3 NH3 PbI 3 and CH3 NH3 SnI3 Perovskites for Solar Cell Applications," Sci. Rep. **4**, 4467 (2014).

[60] Bing Li, Yukinobu Kawakita, Yucheng Liu, Mingchao Wang, Masato Matsuura, Kaoru Shibata, Seiko Ohira-Kawamura, Takeshi Yamada, Shangchao Lin, Kenji Nakajima, and Shengzhong Frank Liu, "Polar rotor scattering as atomic-level origin of low mobility and thermal conductivity of perovskite CH 3 NH 3 PbI 3," Nat. Commun. **8**, 16086 (2017).

[61] Tufan Ghosh, Sigalit Aharon, Lioz Etgar, and Sanford Ruhman, "Free Carrier Emergence and Onset of Electron-Phonon Coupling in Methylammonium Lead Halide Perovskite Films," J. Am. Chem. Soc. **139**, 18262–18270 (2017).

[62] Omer Yaffe, Yinsheng Guo, Liang Z. Tan, David A. Egger, Trevor Hull, Constantinos C. Stoumpos, Fan Zheng, Tony F. Heinz, Leeor Kronik, Mercouri G. Kanatzidis, Jonathan S. Owen, Andrew M. Rappe, Marcos A. Pimenta, and Louis E. Brus, "Local Polar Fluctuations in Lead Halide Perovskite Crystals," Phys. Rev. Lett. **118**, 136001 (2017).

[63] M. Songvilay, N. Giles-Donovan, M. Bari, Z. G. Ye, J. L. Minns, M. A. Green, Guangyong Xu, P. M. Gehring, K. Schmalzl, W. D. Ratcliff, C. M. Brown, D. Chernyshov, W. Van Beek, S. Cochran, and C. Stock, "Common acoustic phonon lifetimes in inorganic and hybrid lead halide perovskites," Phys. Rev. Mater. **3**, 093602 (2019).

[64] Xin Gang Zhao, Gustavo M. Dalpian, Zhi Wang, and Alex Zunger, "Polymorphous nature of cubic halide perovskites," Phys. Rev. B **101**, 155137 (2020).

[65] Alex M. Ganose, Adam J. Jackson, and David O. Scanlon, "sumo: Command-line tools for plotting and analysis of periodic ab initio calculations," J. Open Source Softw. **3**, 717 (2018).

Chapter 6

Conclusions and Further Work

6.1 Conclusions

In this section, I will discuss the research presented in the previous chapters and outline the significance of the work.

6.1.1 Symmetry Adapted Pair Distribution Function Analysis (SAPA): A Novel Approach to Evaluating Lattice Dynamics and Local Distortions from Total Scattering Data

In this paper, we sought to demonstrate the work which encompassed the primary goal of my project: an unbiased, symmetry-motivated approach to analysing the local structure of crystalline materials, measured by the use of total scattering experiments. The primary goal of this method is to determine how the local structure deviates from the long-range average structure and, therefore, gain insight into the dynamics of the studied materials. There have been previous attempts in the literature to use total scattering data to quantify the dynamics of a material, but these methods have their drawbacks. The first of these methods involves pre-selection of a standard phonon model and the refinement of the theoretical pair distribution functions of the model against the experimental pair distribution function obtained from the total scattering data. The pre-selection of a phonon model introduces bias into the analysis, and the method itself has been shown to be inaccurate for all but the simplest of systems. The second method uses the reverse Monte Carlo algorithm to generate several atomistic configurations which all fit the data. These configurations are then treated like different time-steps in a molecular dynamics simulation and phonon dispersion curves can be calculated[160, 32]. This technique also introduces bias due to the inclusion of constraints in the "energy" function

the RMC algorithm minimises, and, while the method is certainly more accurate than the standard phonon model approach, it has its limits and is a fairly complex and computationally intensive procedure. The SAPA approach I present in this paper is used to identify the symmetry-adapted displacements which best describe the deviation of the local structure from the average. Displacements which transform as the same irrep are tested simultaneously, and the refinements for each set of modes are repeated several times from random starting values. By doing this, an unbiased view of the dynamics can be obtained. In the first example presented in the paper, we identify scissoring modes, which cause a distortion of the intra-octahedral bond angles, to be the dominant distortion modes in ScF_3. Importantly, they involve transverse displacements of the F anions, which could lead to negative thermal expansion *via* the tension or "guitar-string" effect. These findings are discussed further in chapter 3. In the second example, modes belonging to the Γ_4^- irrep, which correspond to polar displacements of the Ti and O ions, are found to be the primary order parameter for the phase transitions of $BaTiO_3$. This is unsurprising, as the general nature of this phase transition has been known for some time. We find that the underlying nature of this order parameter to be rhombohedral, or quasi-rhombohedral, at all temperatures, supporting the order-disorder picture of $BaTiO_3$. This example points to another strength of the SAPA approach: the modes identified, using SAPA, which best describe the local structural deviations, can be further interrogated to determine any underlying symmetry. This is used in the work presented in chapters 4 and 5.

The motivation behind this paper is to provide other researchers with a step-by-step guide to using Symmetry Adapted Pair Distribution Function Analysis (SAPA) in their work. The paper, along with the examples provided at the GitHub repository in ref [161], should provide enough information for others intending to perform analysis using SAPA.

6.1.2 Anharmonicity and Scissoring Modes in the Negative Thermal Expansion Materials ScF_3 and $CaZrF_6$

For this paper, we analyse the local structure of two negative thermal expansion materials, ScF_3 and $CaZrF_6$, using the symmetry-adapted pair distribution function analysis presented in chapter 2. Both materials exhibit isotropic NTE over a wide temperature range, with a coefficient of thermal expansion similar in magnitude to that of ZrW_2O_8. While the former compound, ScF_3, is often used as an example to illustrate the rigid unit mode model of negative thermal expansion[36], the mechanism driving the NTE is not fully understood. Rigid unit modes are soft

in ScF_3, since a RUM-driven phase transition is observed with applied pressure[162]. Recently, however, a new model for the NTE in ScF_3 has been proposed, in which the motions of F anions are completely uncorrelated, in analogy with the entropic elasticity of freely-jointed polymer chains[77]. Less is known about the negative thermal expansion of $CaZrF_6$, but previous reports had highlighted flexibility of the M–F (M = Ca, Zr) linkages as having an effect[163, 164, 165].

Applying the SAPA method to X-ray pair distribution data of both compounds reveals that the dominant distortions for both compounds are "scissoring modes", a distortion in which the intra-octahedral bond angles are distorted *via* transverse displacements of the F anions, with the bond lengths unchanged. These modes have a higher amplitude in $CaZrF_6$ than in ScF_3, which correlates well with the greater magnitude of NTE in $CaZrF_6$ reported in the literature. We also compare two-phase and single-phase models, in which distortions can either act competetively or cooperatively, respectively, to test coupling between modes from different irreps. We find that scissoring modes associated with the X_5^+ and M_5^- irreps couple together in $CaZrF_6$. This is permitted within the harmonic approximation, since the lower $Fm\bar{3}m$ symmetry of this structure due to the rock-salt ordering of Ca and Zr ions means these displacements transform as one irrep. Additionally, we find evidence for anharmonic coupling between the scissoring modes of the X_5^+ and the rigid unit modes of the R_5^- irreps in ScF_3.

This paper acts as an introduction, of sorts, to an emerging theme of this thesis. We find that scissoring modes are a key distortion for all the systems studied in this thesis and have often been left unstudied in the literature. All the systems studied consist of a network of corner-sharing octahedra, with either an "empty" *A*-site (ScF_3, $CaZrF_6$, ReO_3) or a highly dynamic *A*-site (MAPbX_3, X = I, Br, Cl). I envisage that studies of similar systems, previously thought rigid, could be enhanced by considering the possibility of structural flexibility in the form of scissoring modes.

6.1.3 Soft mode anisotropy in negative thermal expansion material ReO_3

This work builds on the analysis of ScF_3 and $CaZrF_6$ presented in chapter 3. The studied material, ReO_3, is isostructural to ScF_3 and also exhibits negative thermal expansion, but only for a limited temperature range. We also build on the work of Dove *et al*[166], who came to a similar conclusion about the importance of scissoring modes in ScF_3 using reverse Monte Carlo analysis of neutron PDF data. In perovskites, and perovskite-related materials, pure RUMs are restricted to the M-R line in reciprocal space. As we move away from this line, we find modes

with a mixed RUM and scissoring mode character, with an increasing component of scissoring modes for wave vectors further from the M-R line. Dove hypothesised that the prevalence of scissoring modes in ScF_3 allow a significant proportion of these quasi-RUMs to have a negative Grüneisen parameter, increasing the overall contribution of NTE phonons to the thermal expansion properties.

In this paper, we investigate the hypothesis that the increased charge on the O anions in ReO_3 compared to the F anions in ScF_3 lead to reduced structural flexibility which is ultimately responsible for the restricted temperature range of negative thermal expansion. The results of the SAPA method support this hypothesis: at low temperatures, at which ReO_3 shows negative thermal expansion, the deviation of the local structure from the average is best desribed by in-phase rotations of the octahedra. The SAPA analysis, in conjunction with a two-phase model with competetive scissoring and rigid unit modes, shows that the scissoring modes become dominant only after the onset of positive thermal expansion. This coincides with a hardening of the RUM, causing the RUMs and quasi-RUMs to contribute less to the mean Grüneisen parameter, resulting in a switch from negative to positive thermal expansion.

Between this and the preceeding chapter, I have shown that structural flexibility is a key determining factor in determining the magnitude and extent of NTE within network materials. Work by Rimmer *et al.* has shown that flexibility is a key factor in driving the NTE in materials where units smaller than a polyhedra are the "rigid element", such as Cu-O-Cu bonds in Cu_2O[167] or Y-O rods in $Y_2W_3O_12$[168]. My work also shows that flexibility must also be considered an integral part of the rigid unit mode model.

In section 6.1.1, I stated that an advantage of the SAPA method is the ability to further interrogate the underlying symmetry of the distortions the analysis finds to be significant. In this paper, we do this by parameterising the three arms of the M_2^+ order parameter in terms of spherical polar coordinates and refining the amplitude of the distortion at different points on a grid covering the angular coordinates. We found the distribution in the R-factor of the refinements to be highly anisotropic across the whole temperature range, showing a clear preference for the M_2^+ $(a; 0; 0)$ order parameter direction. This OPD generates structures with a $P4/mbm$ symmetry, which is the first phase achieved with applied pressure, before a further transition to a phase with the $Im\bar{3}$ space group. This anisotropy indicates that the dynamic displacements associated with the M_2^+ irrep are anharmonic. Further investigation of the anisotropy using DFT calculations revealed that for small mode amplitudes, order parameter directions with $P4/mbm$ and $Im\bar{3}$ symmetry

have an almost identical energy cost. We therefore argue that the entropic cost of the fluctuation must determine the character of the phonon modes.

This work links to the general theme of the thesis that structural flexibility of many apparently rigid materials is a key factor in determining their observed properties. In addition, throughout this thesis, the underlying symmetry of distortions is found to be important, in this case leading to key insights into the role of entropy in determining the character of distortion modes.

6.1.4 Large dynamic scissoring mode displacements coupled to band gap opening in Hybrid Perovskites

In this paper, we use the SAPA method presented in chapter 2 to analyse the cubic phases of the hybrid perovskites MAPbX_3, $X = $ I, Br, Cl. These materials have been widely studied in recent years due to their promise as low-cost, high-efficiency solar cell materials. Despite this, the origin of their desirable properties as photovoltaics is not fully understood. The presence of the methylammonium cation on the A-site, rather than a metal ion, is likely to have an influence, although devices made with MAPbBr$_3$ and CsPbBr$_3$ have been shown to have similar performances[138]. The dynamics of the organic cations and the inorganic backbone of the material are known to be inherently linked, and we sought to probe this using the SAPA method.

This work uses X-ray PDF data, so we were only able to directly probe the dynamics of the inorganic framework due to the low scattering power for X-rays of the organic components. As a continuation of the theme of this thesis, we find scissoring modes to best describe the deviation of the local structure from the average in all three studied materials. Using DFT calculations, we show that the large amplitude scissoring modes have a significantly anharmonic energy well, meaning they are able to couple to the dynamic modes of the organic cation. Further calculations show that MA cations rotate to accomodate the large amplitude of the scissoring modes. We also show that the scissoring mode distortions lead to significant band gap opening. We hypothesise that the average structure of the hybrid perovskites are likely highly distorted locally. Calculations performed on these materials should take this into account.

6.1.5 Summary

In this thesis, I have presented a new method to extract dynamics information from total scattering experiments. This method uses the structure of the material being studied, or a higher symmetry parent structure, along with a user-defined

supercell expansion, as input. This reduces the possible sources of bias within the analysis. I have also presented 3 demonstrations of this method to perovskite-related materials. It has proven useful in extracting the dominant distortion modes in the studied systems.

6.2 Further Work

In this section, I will explore how the work presented in this thesis could be developed further. The two primary aspects of my research, the development of the SAPA method and the materials I have applied this method to, will be discussed separately.

6.2.1 Further Development of Symmetry-Adapted Pair Distribution Function Analysis

At the moment, the SAPA method has only been used to analyse the local structures of compounds with high-symmetry cubic structures, or, in the case of $BaTiO_3$, structures distorted from a high-symmetry cubic structure. Lower-symmetry structures with well understood distortions would prove a good test case. A good example of this is the $Ca_{2-x}Sr_xMn_{1-y}Ti_yO_4$ family of materials. They have the $n = 1$ Ruddlesden-Popper structure and show switching between positive thermal expansion and uniaxial negative thermal expansion for different values of x and y[169]. These, and similar, materials have been extensively analysed by the Senn Group and collaborators, and the mechanism driving the uniaxial negative thermal expansion is well understood. The negative thermal expansion is facilitated by a "corkscrew" mechanism that couples the tilts and rotations of octahedra in the perovskite layers to the tetragonal strain. If applying SAPA to these structures as a function of x and y, rather than the temperature dependent experiments performed in this thesis, it would prove a good inital test on lower-symmetry structures.

A good test case for a lower symmetry structure would be to analyse the chalcohalide photovoltaic absorber $Sn_2SbS_2I_3$. This compound was originally reported to have a centrosymmetric structure with the $Cmcm$ space group[170]. Recently, computational work by Walsh *et al* has shown the structure to actually be an average over multiple polar $Cmc2_1$ configurations[171]. The local structure should be sensitive to this, so SAPA should detect polar modes of the Sb ions as the largest deviation from the $Cmcm$ structure. A similar analysis could be performed on the Pb analogue, $Pb_2SbS_2I_3$. This compound has also been reported to have an orthorhombic structure with space group $Cmcm$ at room temperature. In addition, Sb can be substituted for Bi in both compounds. Since displacements of the Sb ions

are the origin of disorder in $Sn_2SbS_2I_3$, it would be interesting to see the effect of substituting these for Bi.

Another useful development would be to expand the range of software the technique is available for. In chapter 2, I present scripts that convert .CIF files generated by the ISODISTORT software into an input file for the *Topas Academic* software. Expanding this to include scripts for use with the *DiffPy-CMI* python library or other software would increase the accessibility of the SAPA method.

The spherical polar coordinate parameterisation of the modes transforming as the M_2^+ irrep in ReO_3 proved valuable in revealing the underlying anisotropy in the order parameter direction of this distortion. While we can use this to analyse other 3 (or fewer) component order parameters, a method of performing a similar analysis on irreps with more parameters would be useful. This would allow more of the distortion space to be explored for irreps such as X_5^+ for MAPbX_3 (X = I, Br, Cl), rather than refining specific order parameter directions as I did in chapter 5. Analagously to the spherical polar coordinates, one can define polar coordinates for an n-dimensional sphere using a radial coordinate, r, and $n-1$ angular coordinates. Rather than visualising the distribution of R_w as a heatmap, as done in chapter 4, the variation of R_w with respect to the different polar coordinates would need to be viewed individually. Further difficulty comes in the "gridding" of the polar coordinate space. In chapter 4, I used 36 grid points for θ and 72 for ϕ, resulting in 2592 data points per temperature. An identical grid size for the 6-dimensional sphere would result in approximately $1.2 \cdot 10^8$ data points and file sizes on the order of 10 GB. This also doesn't take into account the computational time to perform these refinements: assuming approximately 1 second per refinement, each temperature point for the M_2^+ irrep takes about 40 minutes. Extending this to a 6-component order parameter would take over 3 years. This can be reduced by using a less fine grid, but without further parameterising the order parameter in some way, this analysis remains unfeasible.

During the development of the SAPA approach, I also developed a different approach to modelling distortions within the Topas Academic software. For a harmonic oscillator, the displacement of the atoms undergoing the distortion of interest varies as a sine curve with respect to time. We can sample different points along this sine curve in different phases and therefore determine the amplitude of the distortion. For an anharmonic oscillator, the oscillation is less simple. Using an approximate solution to a 4th order anharmonic oscillator (*i.e*, an oscillator with potential $V(x) = \frac{1}{2}m\omega^2x^2 + \frac{1}{4}\epsilon mx^4$), an attempt could be made to determine the quartic component of the oscillation.

There are some downsides to the SAPA method. Firstly, it requires that the local deviations from the average structure are somewhat ordered. Uncorrelated disorder would still be best analysed using reverse Monte Carlo analysis. Secondly, the PDF is much more sensitive to low-frequency than high-frequency information, therefore non total scattering based techniques need to be used to analyse this information. Finally, the SAPA method can not differentiate between static and dynamic distortions, although recent developments have allowed energy-resolved pair distribution functions to be measured[172]. The SAPA method could be extended to apply to this dynamic pair distribution function technique.

6.2.2 Further Analysis of Negative Thermal Expansion Materials

In this thesis, I have presented a thorough analysis of the mechanism driving the negative thermal expansion in the materials ScF_3, ReO_3 and $CaZrF_6$. This analysis could be taken further by performing SAPA on neutron PDF data on ScF_3, to see if the higher Q_{max} available for spallation sources such as ISIS, compared to the comparitively low value of the P02.1 beamline at PETRA III, has an impact upon results. In addition, the greater Q_{max} would allow the nature of the RUMs to be investigated, in comparison with the spherical parameterisation performed for ReO_3.

By using a gas pressure cell, the sequence of phase transitions with applied pressure could be investigated using SAPA. This could lead credence to our theories that the additional vibrational entropy due to uncondensed RUMs are key in stabilising the $P4/mbm$ phase in ReO_3.

The theory that the reduced interaction strength of F^- compared to O^{2-}, which leads to lower force constants governing octahedral deformation and a greater magnitude for NTE could be further investigated by analysing other fluorine analogues of oxide NTE materials, such as ZnF_2, an analogue of TiO_2.

6.2.3 Further Analysis of Hybrid and Halide Perovskites

There is still a lot to be determined about both fully inorganic and hybrid organic-inorganic halide perovskites. My work in chapter 5 shows that the dynamics of the organic cations and inorganic framework in the methylammonium lead halides are inherently linked, with the organic cations reorienting to accomodate the large amplitude scissoring modes. The extent to which they are linked is still to be fully assessed. This could be performed using a combination of theoretical work and total scattering studies. Using molecular dynamics, the response of the cations to different distortions of the inorganic framework, chosen by the user, could be

assessed at a range of temperatures. The reverse analysis could also be performed: choosing different alignments and orderings of the organic cations and determining the resulting distortions of the framework.

The linked organic and inorganic dynamics could also be studied experimentally by using a combination of the SAPA and RMC methods for analysing total scattering data. As I have demonstrated in chapter 5, applying the SAPA method to X-ray PDF data of the methylammonium lead halides allows the inorganic dynamics to be analysed without having to account for the organic component of the structure, since it has a very weak scattering power for X-rays. The distortions found from SAPA could then be used as an input for RMC analysis of neutron PDF data. The methylammonium cation, if deuterated, is a good coherent scatterer of neutrons, and the RMC method has proven to be a powerful tool for studying disordered materials. These methods could also be used to analyse other hybrid perovskites, such as the family of formamadinium lead halides.

The RMC method would also prove useful in investigating the polymorphic nature of cubic halide perovskites. The RMC method could generate atomistic configurations which agree with both the local and average structure which could be broken down into smaller cells. The variation in structure across these smaller components could then be analysed by a number of means. For example, the ISODISTORT program could be used to determine the distortion modes which give rise to the possible polymorphs if they are related by symmetry to the parent structure.

Bibliography

[1] E. Prince et al, *International Tables for Crystallography Volume C*, Springer, 3rd edn., 2004.

[2] P. A. Chater, *Diamond Light Source, Beamline I15-1*, `https://www.diamond.ac.uk/Instruments/Crystallography/I15-1/layout.html`.

[3] A.-C. Dippel, H.-P. Liermann, J. T. Delitz, P. Walter, H. Schulte-Schrepping, O. H. Seeck and H. Franz, *J. Synchrotron Radiat.*, 2015, **22**, 675–687.

[4] S. Sasaki, C. T. Prewitt, J. D. Bass and W. A. Schulze, *Acta Crystallogr. Sect. C*, 1987, **43**, 1668–1674.

[5] C. Kittel, *Introduction to Solid State Physics*, Wiley, 8th edn., 2004.

[6] T. Hahn et al, *International Tables for Crystallography, Volume A*, International Union of Crystallography by Springer, 5th edn., 2005.

[7] A. Authier, *Early Days of X-ray Crystallography*, Oxford University Press, 2013.

[8] W. L. Bragg, *Proc. Cambridge Phil. Soc.*, 1913, **17**, 43–57.

[9] W. Friedrich, P. Knipping and M. Laue, *Ann. Phys.*, 1913, **346**, 971–988.

[10] E. Fermi, *Nuclear Physics*, University of Chicago Press, 1950.

[11] D. L. Price and F. Fernandez-Alonso, *An Introduction to Neutron Scattering*, Elsevier Inc., 1st edn., 2013, vol. 44, pp. 1–136.

[12] R. G. Newton, *Scattering theory of waves and particles*, Springer, 2nd edn., 1982.

[13] M. Born, *Z. Phys.*, 1926, **38**, 803.

[14] J. Baruchel, J.-L. Hodeau, M. S. Lehmann and J.-R. Regnard, *Neutron and Synchrotron Radiation for Condensed Matter Studies*, Springer, 1994.

[15] S. J. Billinge and T. Egami, *Underneath the Bragg Peaks*, Pergamom, 2nd edn., 2012.

[16] D. A. Keen, *J. Appl. Crystallogr.*, 2001, **34**, 172–177.

[17] D. A. Keen, *Crystallogr. Rev.*, 2020, **26**, 141–199.

[18] T. E. Faber and J. M. Ziman, *Philos. Mag.*, 1965, **11**, 153–173.

[19] A. K. Soper and E. R. Barney, *J. Appl. Cryst*, 2011, **44**, 714–726.

[20] G. S. Pawley, *J. Appl. Cryst*, 1980, **13**, 630–633.

[21] A. Le Bail, H. Duroy and J. L. Fourquet, *Mat. Res. Bull.*, 1988, **23**, 447–452.

[22] H. M. Rietveld, *J. Appl. Cryst*, 1969, **2**, 65–71.

[23] C. L. Farrow, P. Juhas, J. W. Liu, D. Bryndin, E. S. Boin, J. Bloch, T. Proffen and S. J. Billinge, *J. Phys. Condens. Matter*, 2007, **19**, 335219.

[24] A. A. Coelho, P. A. Chater and A. Kern, *J. Appl. Crystallogr.*, 2015, **48**, 869–875.

[25] R. L. Mcgreevy and L. Pusztai, *Mol. Simul.*, 1988, **1**, 359–367.

[26] M. G. Tucker, D. A. Keen, M. T. Dove, A. L. Goodwin and Q. Hui, *J. Phys. Condens. Matter*, 2007, **19**, year.

[27] W. Reichardt and L. Pintschovius, *Phys. Rev. B*, 2001, **63**, 174302.

[28] D. A. Dimitrov, D. Louca and H. Röder, *Phys. Rev. B*, 1999, **60**, 6204–6207.

[29] M. Graf, I. K. Jeong, D. Starr and H. Heffner, *Phys. Rev. B*, 2003, **68**, 064305.

[30] A. L. Goodwin, M. G. Tucker, M. T. Dove and D. A. Keen, *Phys. Rev. Lett.*, 2004, **93**, 075502.

[31] A. L. Goodwin, M. G. Tucker, E. R. Cope, M. T. Dove and D. A. Keen, *Phys. Rev. B*, 2005, **72**, 214304.

[32] M. T. Dove, *Introduction to Lattice Dynamics*, Cambridge University Press, 1st edn., 1993.

[33] A. M. Kosevich, *The Crystal Lattice: Phonons, Solitons, Dislocations, Superlattices*, Wiley, 2nd edn., 2005.

[34] H. T. Stokes and D. M. Hatch, *Introduction to Isotropy Subgroups and Displacive Phase Transitions*, 2006, `https://iso.byu.edu/iso/2006Stokes.pdf`.

[35] M. S. Senn, *Irreducible Representation Analysis - descriptions of some of the terminology used in the field*, 2018, `https://pcgschool2018.files.wordpress.com/2018/06/pcgsummerschool2018_irreps_descriptions_of_terminology.pdf`.

[36] M. T. Dove and H. Fang, *Rep. Prog. Phys.*, 2016, **79**, 066503.

[37] Y. Oba, T. Tadano, R. Akashi and S. Tsuneyuki, *Physical Rev. Mater.*, 2019, **3**, 033601.

[38] H. T. Stokes and D. M. Hatch, *Phase Transit.*, 1991, **34**, 53–67.

[39] A. Saxena, D. M. Hatch and G. R. Barsch, *Phase Transit.*, 1994, **46**, 89–142.

[40] C. J. Howard and H. T. Stokes, *Acta Crystallogr. Sect. A*, 2005, **61**, 93–111.

[41] M. I. Aroyo, C. Capillas, G. De la Flor, A. K. Kirov, D. Orobengoa, J. M. Perez-Mato and H. Wondraschek, *Representations of Crystallographic Groups*, 2010, `http://cloud.crm2.univ-lorraine.fr/pdf/nancy2010/Aroyo_reps2010.pdf`.

[42] B. J. Campbell, H. T. Stokes, D. E. Tanner and D. M. Hatch, *J. Appl. Crystallogr.*, 2006, **39**, 607–614.

[43] S. C. Miller and W. F. Love, *Tables of Irreducible Representations of Space Groups and Co-Representations of Magnetic Space Groups*, Pruett, 1967.

[44] C. Lind, *Materials*, 2012, **5**, 1125–1154.

[45] J. S. O. Evans, T. A. Mary, T. Vogt, M. A. Subramanian and A. W. Sleight, *Chem. Mater.*, 1996, **8**, 2809–2823.

[46] R. Huang, L. Li, F. Cai, X. Xu and L. Qian, *Appl. Phys. Lett.*, 2008, **93**, 081902.

[47] T. Hamada and K. Takenaka, *J. Appl. Phys.*, 2011, **109**, 2009–2012.

[48] K. Takenaka and H. Takagi, *Appl. Phys. Lett.*, 2005, **87**, 261902.

[49] Y. Qiao, Y. Song, K. Lin, X. Liu, A. Franz, Y. Ren, J. Deng, R. Huang, L. Li, J. Chen and X. Xing, *Inorg. Chem.*, 2019, **58**, 5380–5383.

[50] J. Chen, K. Nittala, J. S. Forrester, J. L. Jones, J. Deng, R. Yu and X. Xing, *J. Am. Chem. Soc.*, 2011, **133**, 11114–11117.

[51] M. Azuma, W. T. Chen, H. Seki, M. Czapski, S. Olga, K. Oka, M. Mizumaki, T. Watanuki, N. Ishimatsu, N. Kawamura, S. Ishiwata, M. G. Tucker, Y. Shimakawa and J. P. Attfield, *Nat. Commun.*, 2011, **2**, 347.

[52] P. J. Attfield, *Front. Chem.*, 2018, **6**, 371.

[53] E. Grüneisen, *Ann. Phys.*, 1912, **344**, 257–306.

[54] T. H. K. Barron and M. L. Klein, in *Dynamical Properties of Solids*, ed. G. K. Horton and A. A. Maradudin, Elsevier, 1974, ch. 7, pp. 391–451.

[55] V. Heine, P. R. L. Welche and M. T. Dove, *J. Am. Ceram. Soc.*, 1999, **82**, 1793–1802.

[56] M. T. Dove, P. R. L. Welche and V. Heine, *Phys. Chem. Miner.*, 1998, **26**, 63–77.

[57] V. Korthuis, N. Khosrovani, A. W. Sleight, N. Roberts, R. Dupree and W. W. Warren, *Chem. Mater.*, 1995, **7**, 412–417.

[58] A. K. Pryde, K. D. Hammonds, M. T. Dove, V. Heine, J. D. Gale and M. C. Warren, *J. Phys. Condens. Matter*, 1996, **8**, 10973–10982.

[59] M. Dapiaggi, H. J. Kim, E. S. Božin, S. J. Billinge and G. Artioli, *J. Phys. Chem. Solids*, 2008, **69**, 2182–2186.

[60] G. Artioli, M. Dapiaggi, P. Fornasini, A. Sanson, F. Rocca and M. Merli, *J. Phys. Chem. Solids*, 2006, **67**, 1918–1922.

[61] A. Sanson, F. Rocca, G. Dalba, P. Fornasini, R. Grisenti, M. Dapiaggi and G. Artioli, *Phys. Rev. B*, 2006, **73**, 214305.

[62] M. P. Attfield and A. W. Sleight, *Chem. Mater.*, 1998, **10**, 2013–2019.

[63] P. Daniel, A. Bulou, M. Rousseau and J. Nouet, *Phys. Rev. B*, 1990, **42**, 10545–10552.

[64] M. T. Dove, *Phil. Trans. R. Soc. A*, 2019, **377**, 1–18.

[65] W. Miller, C. W. Smith, D. S. MacKenzie and K. E. Evans, *Materia. Sci. Eng.*, 1987, **95**, 303–308.

[66] Q. Gao, N. Shi, Q. Sun, A. Sanson, R. Milazzo, A. Carnera, H. Zhu, S. H. Lapidus, Y. Ren, Q. Huang, J. Chen and X. Xing, *Inorg. Chem.*, 2018, **57**, 10918–10924.

[67] M. T. Dove, D. A. Keen, A. C. Hannon and I. P. Swainson, *Phys. Chem. Miner.*, 1997, **24**, 311–317.

[68] S. J. Hibble, A. M. Chippindale, E. Marelli, S. Kroeker, V. K. Michaelis, B. J. Greer, P. M. Aguiar, E. J. Bilbé, E. R. Barney and A. C. Hannon, *J. Am. Chem. Soc.*, 2013, **135**, 16478–16489.

[69] K. W. Chapman and P. J. Chupas, *Chem. Mater.*, 2009, **21**, 425–431.

[70] K. W. Chapman, P. J. Chupas and C. J. Kepert, *J. Am. Chem. Soc.*, 2005, **127**, 15630–15636.

[71] S. J. Hibble, S. M. Cheyne, A. C. Hannon and S. G. Eversfield, *Inorg. Chem.*, 2002, **41**, 4990–4992.

[72] S. J. Hibble, S. M. Cheyne, A. C. Hannon and S. G. Eversfield, *Inorg. Chem.*, 2002, **41**, 1042–1044.

[73] M. G. Tucker, A. L. Goodwin, M. T. Dove, D. A. Keen, S. A. Wells and J. S. O. Evans, *Phys. Rev. Lett.*, 2005, **95**, 255501.

[74] M. G. Tucker, D. A. Keen, J. S. O. Evans and M. T. Dove, *J. Phys. Condens. Matter*, 2007, **19**, 335215.

[75] F. Bridges, T. Keiber, P. Juhas, S. J. Billinge, L. Sutton, J. Wilde and G. R. Kowach, *Phys. Rev. Lett.*, 2014, **112**, 045505.

[76] A. Sanson, *Chem. Mater.*, 2014, **26**, 3716–3720.

[77] D. Wendt, E. Bozin, J. Neuefeind, K. Page, W. Ku, L. Wang, B. Fultz, A. Tkachenko and I. Zaliznyak, *Science Adv.*, 2019, **5**, 1–7.

[78] A. R. Chakhmouradian and P. M. Woodward, *Phys. Chem. Miner.*, 2014, **41**, 387–391.

[79] E. Knittle and R. Jeanloz, *Science*, 1987, **235**, 668–670.

[80] A. S. Bhalla, R. Guo and R. Roy, *Mater. Res. Innov.*, 2000, **4**, 3–26.

[81] K. S. Aleksandrov, *Ferroelectrics*, 1978, **20**, 61–67.

[82] R. Ali and M. Yashima, *J. Solid State Chem.*, 2005, **178**, 2867–2872.

[83] V. M. Goldschmidt, *Die Naturwissenschaften*, 1926, **14**, 477–485.

[84] C. J. Bartel, C. Sutton, B. R. Goldsmith, R. Ouyang, C. B. Musgrave, L. M. Ghiringhelli and M. Scheffler, *Science Adv.*, 2019, **5**, 1–10.

[85] S. V. Krivovichev, *Z. Kristallogr.*, 2008, **223**, 109–113.

[86] A. M. Arévalo-Lõpez, G. M. McNally and J. P. Attfield, *Angew. Chem. Int. Ed.*, 2015, **54**, 12074–12077.

[87] K. Kobayashi, T. Kimura, H. Sawada, K. Terakura and Y. Tokura, *Nature*, 1998, **395**, 677–680.

[88] M. S. Senn, A. Bombardi, C. A. Murray, C. Vecchini, A. Scherillo, X. Luo and S. W. Cheong, *Phys. Rev. Lett.*, 2015, **114**, 23–27.

[89] S. N. Ruddlesden and P. Popper, *Acta Crystallogr.*, 1958, **11**, 54–55.

[90] L. T. Nguyen and R. J. Cava, *Chem. Rev.*, 2021, **121**, 2935–2965.

[91] M. S. Senn and N. C. Bristowe, *Acta Crystallogr. Sect. A*, 2018, **74**, 308–321.

[92] M. S. Senn, D. A. Keen, T. C. Lucas, J. A. Hriljac and A. L. Goodwin, *Phys. Rev. Lett.*, 2016, **116**, 207602.

[93] A. M. Glazer, *Acta Crystallogr. Sect. B*, 1972, **28**, 3384–3392.

[94] A. M. Glazer, *Acta Crystallogr. Sect. A*, 1975, **31**, 756–762.

[95] H. T. Stokes, E. H. Kisi, D. M. Hatch and C. J. Howard, *Acta Crystallogr. Sect. B*, 2002, **58**, 934–938.

[96] H. L. Boström, M. S. Senn and A. L. Goodwin, *Nat. Commun.*, 2018, **9**, 2380.

[97] A. Poglitsch and D. Weber, *J. Chem. Phys.*, 1987, **87**, 6373–6378.

[98] A. Kojima, K. Teshima, Y. Shirai and T. Miyasaka, *J. Am. Chem. Soc.*, 2009, **131**, 6050–6051.

[99] G. Schileo and G. Grancini, *J. Phys.: Energy*, 2020, **2**, 021005.

[100] M. A. Green, A. Ho-Baillie and H. J. Snaith, *Nat. Photonics*, 2014, **8**, 506–514.

[101] S. Sun, T. Salim, N. Mathews, M. Duchamp, C. Boothroyd, G. Xing, T. C. Sum and Y. M. Lam, *Energy Environ. Sci.*, 2014, **7**, 399–407.

[102] C. Wehrenfennig, G. E. Eperon, M. B. Johnston, H. J. Snaith and L. M. Herz, *Adv. Mater.*, 2014, **26**, 1584–1589.

[103] G. Xing, N. Mathews, S. Sun, S. S. Lim, Y. M. Lam, M. Grätzel, S. Mhaisalkar and T. C. Sum, *Science*, 2013, **342**, 344–347.

[104] M. Scott, J. Suh, J. Wu and A. M. Minor, *Microsc. Microanal.*, 2016, **22**, 1510–1511.

[105] G. Abdelmageed, L. Jewell, K. Hellier, L. Seymour, B. Luo, F. Bridges, J. Z. Zhang and S. Carter, *Appl. Phys. Lett.l*, 2016, **109**, 233905.

[106] J. Chun-Ren Ke, A. S. Walton, D. J. Lewis, A. Tedstone, P. O'Brien, A. G. Thomas and W. R. Flavell, *Chem. Commun.*, 2017, **53**, 5231–5234.

[107] H. J. Snaith, *Nat. Mater.*, 2018, **17**, 372–376.

[108] S. Yang, W. Fu, Z. Zhang, H. Chen and C.-Z. Li, *J. Mater. Chem. A*, 2017, **5**, 11462–11482.

[109] S. Colella, E. Mosconi, P. Fedeli, A. Listorti, A. Rizzo, F. Gazza, F. Orlandi, P. Ferro, T. Besagni, G. Calestani, F. De Angelis, R. Mosca and G. Gigli, *Chem. Mater.*, 2013, **25**, 4613–4618.

[110] H. Zhang, Y. Lv, J. Wang, H. Ma, Z. Sun and W. Huang, *ACS Appl. Mater. Interfaces*, 2019, **11**, 6022–6030.

[111] G. Niu, W. Li, J. Li, X. Liang and L. Wang, *RSC Adv.*, 2017, **7**, 17473–17479.

[112] D. Liu, S. Li, F. Bian and X. Meng, *Materials*, 2018, **11**, 1141.

[113] P. Zhao, B. J. Kim and H. S. Jung, *Mater. Today Energy*, 2018, **7**, 267–286.

[114] S. Shao, J. Liu, G. Portale, H. H. Fang, G. R. Blake, G. H. ten Brink, L. J. A. Koster and M. A. Loi, *Adv. Energy Mater.*, 2018, **8**, 1702019.

[115] D. Ding, L. Lanzetta, X. Liang, G. Min, M. Giza, T. J. Macdonald and S. A. Haque, *Chem. Commun.*, 2021, **57**, 5047–5050.

[116] A. M. Leguy, J. M. Frost, A. P. McMahon, V. G. Sakai, W. Kochelmann, C. Law, X. Li, F. Foglia, A. Walsh, B. C. O'Regan, J. Nelson, J. T. Cabral and P. R. Barnes, *Nat. Commun.*, 2015, **6**, 7124.

[117] T. Chen, B. J. Foley, B. Ipek, M. Tyagi, J. R. D. Copley, C. M. Brown, J. J. Choi and S.-H. Lee, *Phys. Chem. Chem. Phys.*, 2015, **17**, 31278–31286.

[118] O. Knop, R. E. Wasylishen, M. A. White, T. S. Cameron and M. J. M. V. Oort, *Can. J. Chem.*, 1990, **68**, 412–422.

[119] I. P. Swainson, C. Stock, S. F. Parker, L. Van Eijck, M. Russina and J. W. Taylor, *Phys. Rev. B*, 2015, **92**, 100303.

[120] M. Songvilay, Z. Wang, V. G. Sakai, T. Guidi, M. Bari, Z. G. Ye, G. Xu, K. L. Brown, P. M. Gehring and C. Stock, *Phys. Rev. Mater.*, 2019, **3**, 125406.

[121] H. Mashiyama, Y. Kawamura, H. Kasano, T. Asahi, Y. Noda and H. Kimura, *Ferroelectrics*, 2007, **348**, 182–186.

[122] M. T. Weller, O. J. Weber, P. F. Henry, A. M. Di Pumpo and T. C. Hansen, *Chem. Commun.*, 2015, **51**, 4180–4183.

[123] A. Mattoni, A. Filippetti, M. I. Saba and P. Delugas, *J. Phys. Chem. C*, 2015, **119**, 17421–17428.

[124] K. P. Ong, T. W. Goh, Q. Xu and A. Huan, *J. Phys. Chem. Lett.*, 2015, **6**, 681–685.

[125] Y. Kawamura, H. Mashiyama and K. Hasebe, *J. Phys. Soc. Japan*, 2002, **71**, 1694–1697.

[126] J. Breternitz, F. Lehmann, S. A. Barnett, H. Nowell and S. Schorr, *Angew. Chem. Int. Ed.*, 2020, **59**, 424–428.

[127] C. C. Stoumpos, C. D. Malliakas and M. G. Kanatzidis, *Inorg. Chem.*, 2013, **52**, 9019–9038.

[128] I. P. Swainson, R. P. Hammond, C. Soullière, O. Knop and W. Massa, *J. Solid State Chem.*, 2003, **176**, 97–104.

[129] L. Chi, I. Swainson, L. Cranswick, J. H. Her, P. Stephens and O. Knop, *J. Solid State Chem.*, 2005, **178**, 1376–1385.

[130] Y. Guo, O. Yaffe, D. W. Paley, A. N. Beecher, T. D. Hull, G. Szpak, J. S. Owen, L. E. Brus and M. A. Pimenta, *Phys. Rev. Mater.*, 2017, **1**, 042401.

[131] D. Wiedemann, J. Breternitz, D. W. Paley and S. Schorr, *J. Phys. Chem. Lett.*, 2021, **12**, 2358–2362.

[132] K. Page, J. E. Siewenie, P. Quadrelli and L. Malavasi, *Angew. Chem. Int. Ed.*, 2016, **55**, 14320–14324.

[133] A. Bernasconi and L. Malavasi, *ACS Energy Lett.*, 2017, **2**, 863–868.

[134] A. Bernasconi, K. Page, Z. Dai, L. Z. Tan, A. M. Rappe and L. Malavasi, *J. Phys. Chem. C*, 2018, **122**, 28265–28272.

[135] A. N. Beecher, O. E. Semonin, J. M. Skelton, J. M. Frost, M. W. Terban, H. Zhai, A. Alatas, J. S. Owen, A. Walsh and S. J. Billinge, *ACS Energy Lett.*, 2016, **1**, 880–887.

[136] D. H. Fabini, R. Seshadri and M. G. Kanatzidis, *MRS Bull.*, 2020, **45**, 467–477.

[137] R. J. Worhatch, H. J. Kim, I. P. Swainson, A. L. Yonkeu and S. J. Billinge, *Chem. Mater.*, 2008, **20**, 1272–1277.

[138] D. A. Egger, A. Bera, D. Cahen, G. Hodes, T. Kirchartz, L. Kronik, R. Lovrincic, A. M. Rappe, D. R. Reichman and O. Yaffe, *Adv. Mater.*, 2018, **30**, 1800691.

[139] S. Dastidar, S. Li, S. Y. Smolin, J. B. Baxter and A. T. Fafarman, *ACS Energy Lett.*, 2017, **2**, 2239–2244.

[140] M. Kulbak, D. Cahen and G. Hodes, *J. Phys. Chem. Lett.*, 2015, **6**, 2452–2456.

[141] J. H. Lee, N. C. Bristowe, J. H. Lee, S. H. Lee, P. D. Bristowe, A. K. Cheetham and H. M. Jang, *Chem. Mater.*, 2016, **28**, 4259–4266.

[142] T. J. Jacobsson, W. Tress, J. P. Correa-Baena, T. Edvinsson and A. Hagfeldt, *J. Phys. Chem. C*, 2016, **120**, 11382–11393.

[143] S. M. Vorpahl, R. Giridharagopal, G. E. Eperon, I. M. Hermes, S. A. Weber and D. S. Ginger, *ACS Appl. Energy Mater.*, 2018, **1**, 1534–1539.

[144] Y. Rakita, O. Bar-Elli, E. Meirzadeh, H. Kaslasi, Y. Peleg, G. Hodes, I. Lubomirsky, D. Oron, D. Ehre and D. Cahen, *Proc. Natl. Acad. Sci. USA*, 2017, **114**, E5504–E5512.

[145] Y. Kutes, L. Ye, Y. Zhou, S. Pang, B. D. Huey and N. P. Padture, *J. Phys. Chem. Lett.*, 2014, **5**, 3335–3339.

[146] H. Röhm, T. Leonhard, A. D. Schulz, S. Wagner, M. J. Hoffmann and A. Colsmann, *Adv. Mater.*, 2019, **31**, 1806661.

[147] J. Jankowska and O. V. Prezhdo, *J. Phys. Chem. Lett.*, 2017, **8**, 812–818.

[148] J. M. Frost, K. T. Butler and A. Walsh, *APL Mater.*, 2014, **2**, 081506.

[149] J. M. Frost, K. T. Butler, F. Brivio, C. H. Hendon, M. Van Schilfgaarde and A. Walsh, *Nano Lett.*, 2014, **14**, 2584–2590.

[150] C. Quarti, E. Mosconi and F. De Angelis, *Chem. Mater.*, 2014, **26**, 6557–6569.

[151] K. Frohna, T. Deshpande, J. Harter, W. Peng, B. A. Barker, J. B. Neaton, S. G. Louie, O. M. Bakr, D. Hsieh and M. Bernardi, *Nat. Commun.*, 2018, **9**, 1829.

[152] E. Mosconi, T. Etienne and F. De Angelis, *J. Phys. Chem. Lett.*, 2017, **8**, 2247–2252.

[153] T. Etienne, E. Mosconi and F. De Angelis, *J. Phys. Chem. Lett.*, 2016, **7**, 1638–1645.

[154] M. T. Pham, E. Amerling, H. M. Luong, H. T. Pham, G. K. Larsen, L. Whittaker-Brooks and T. D. Nguyen, *Sci. Rep.*, 2020, **10**, 1–10.

[155] J. M. Frost, *Phys. Rev. B*, 2017, **96**, 195202.

[156] A. J. Neukirch, W. Nie, J. C. Blancon, K. Appavoo, H. Tsai, M. Y. Sfeir, C. Katan, L. Pedesseau, J. Even, J. J. Crochet, G. Gupta, A. D. Mohite and S. Tretiak, *Nano Lett.*, 2016, **16**, 3809–3816.

[157] M. Bonn, K. Miyata, E. Hendry and X. Y. Zhu, *ACS Energy Lett.*, 2017, **2**, 2555–2562.

[158] C. Quarti, E. Mosconi and F. De Angelis, *Phys. Chem. Chem. Phys.*, 2015, **17**, 9394–9409.

[159] M. A. Carignano, A. Kachmar and J. Hutter, *J. Phys. Chem. C*, 2015, **119**, 8991–8997.

[160] M. T. Dove and R. M. Lynden-Bell, *Phil. Mag. B*, 1986, **54**, 443–463.

[161] T. A. Bird and M. S. Senn, *github.com/tabmapi/sapa*, 2021.

[162] B. K. Greve, K. L. Martin, P. L. Lee, P. J. Chupas, K. W. Chapman and A. P. Wilkinson, *J. Am. Chem. Soc.*, 2010, **132**, 15496–15498.

[163] L. Hu, J. Chen, J. Xu, N. Wang, F. Han, Y. Ren, Z. Pan, Y. Rong, R. Huang, J. Deng, L. Li and X. Xing, *J. Am. Chem. Soc.*, 2016, **138**, 14530–14533.

[164] J. C. Hancock, K. W. Chapman, G. J. Halder, C. R. Morelock, B. S. Kaplan, L. C. Gallington, A. Bongiorno, C. Han, S. Zhou and A. P. Wilkinson, *Chem. Mater.*, 2015, **27**, 3912–3918.

[165] A. Sanson, M. Giarola, G. Mariotto, L. Hu, J. Chen and X. Xing, *Mater. Chem. Phys.*, 2016, **180**, 213–218.

[166] M. T. Dove, J. Du, Z. Wei, D. A. Keen, M. G. Tucker and A. E. Phillips, *Phys. Rev. B*, 2020, **102**, 094105.

[167] L. H. Rimmer, M. T. Dove, B. Winkler, D. J. Wilson, K. Refson and A. L. Goodwin, *Phys. Rev. B*, 2014, **89**, 214115.

[168] L. H. Rimmer and M. T. Dove, *J. Phys. Condens. Matter*, 2015, **27**, 185401.

[169] C. Ablitt, H. McCay, S. Craddock, L. Cooper, E. Reynolds, A. A. Mostofi, N. C. Bristowe, C. A. Murray and M. S. Senn, *Chem. Mater.*, 2020, **32**, 605–610.

[170] P. J. Olivier-Fourcade, J. C. Jumas, E. Philippot and M. Maurin, *Z. anorg. allg. Chem.*, 1980, **468**, 91–98.

[171] S. R. Kavanagh, C. N. Savory, D. O. Scanlon and A. Walsh, *Mater. Horiz.*, 2021, Advance Article.

[172] A. M. Fry-Petit, A. F. Rebola, M. Mourigal, M. Valentine, N. Drichko, J. P. Sheckelton, C. J. Fennie and T. M. McQueen, *J. Chem. Phys.*, 2015, **143**, 124201.

Appendix A

Supplementary Material for "Anharmonicity and Scissoring Modes in the Negative Thermal Expansion Materials ScF$_3$ and CaZrF$_6$"

Supporting Information: Anharmonicity and scissoring modes in the negative thermal expansion materials ScF_3 and $CaZrF_6$

T. A. Bird, J. Woodland-Scott, L. Hu, M. T. Wharmby, J. Chen, A. L. Goodwin, M. S. Senn
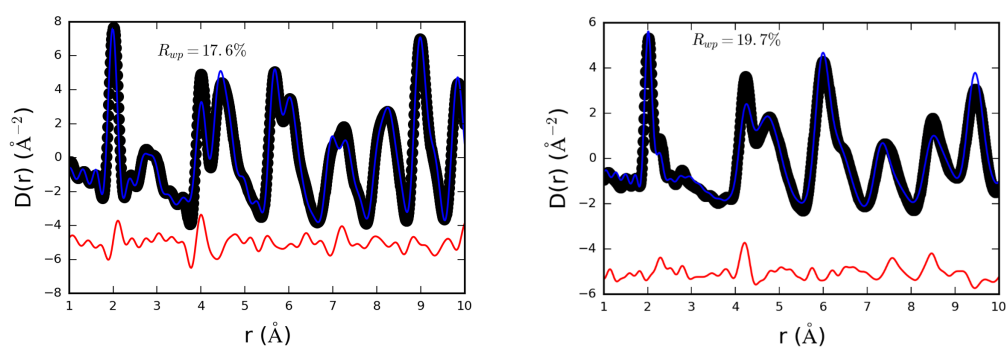
Figure S1: Fits (blue) to pair distribution functions (black) of ScF_3 (left) and $CaZrF_6$ (right) at 400 K using the average structure. The difference between the fit and data is shown in red, with an offset. The TOPAS v6 implementation of the PDFFit peak width function was used.
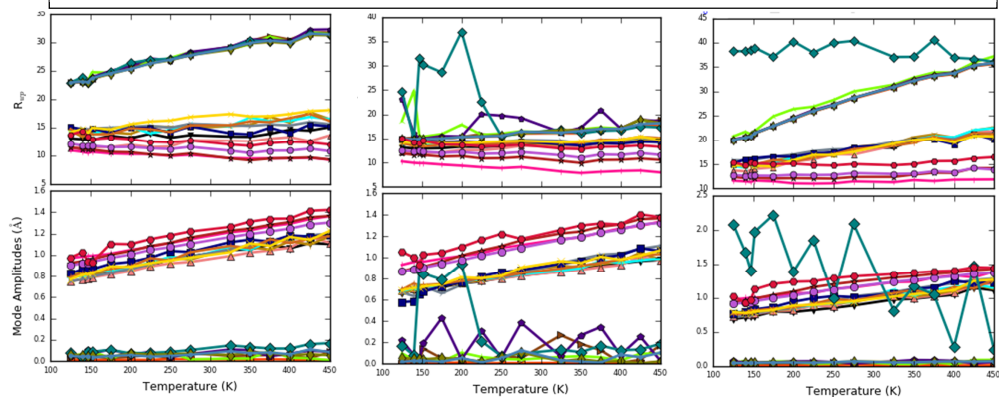
Figure S2: Plots of the best R_{wp} for each single irrep refinement (top) and the weighted mean mode amplitudes (bottom) for ScF_3 for three different thermal parameter functions; the model discussed in the paper (left), the TOPAS v6 implementation of the PDFfit function (middle), and an approximate Debye model (right).
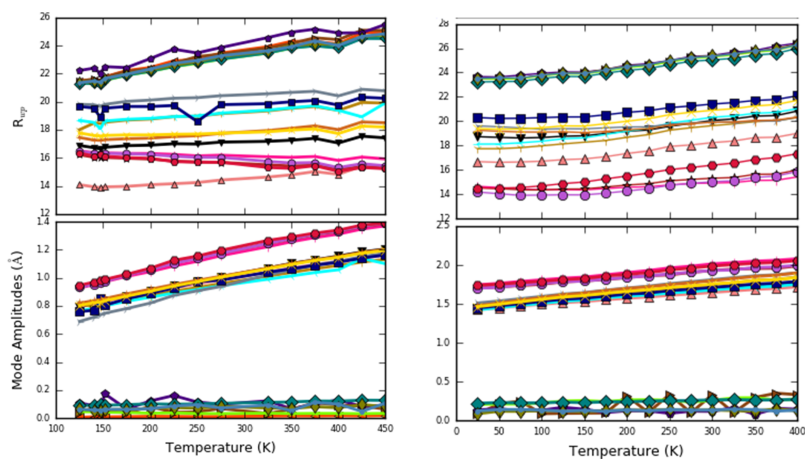
Figure S3: Plots of the best R_{wp} for each single irrep refinement (top) and the weighted mean mode amplitudes (bottom) for ScF_3 and $CaZrF_6$ out to a radius of 30 Å.
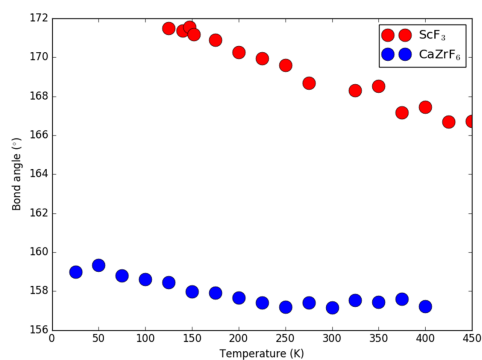
Figure S4: M-F-M (M = Ca, Zr, Sc) bond angles calculated from positions of peaks in the pair distribution functions of ScF_3 (red) and $CaZrF_6$ (blue).
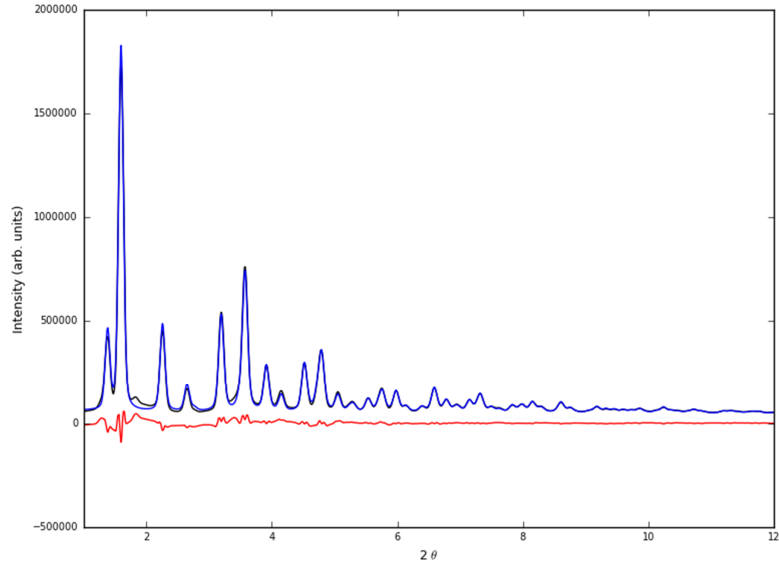
Figure S5: Rietveld fit of CaZrF₆ X-ray powder diffraction data at 125 K, collected at the 11-ID-C of APS, Argonne National Laboratory with a wavelength of 0.117418 Å. The data was fit using the $Fm\bar{3}m$ average structure using anisotropic atomic displacement parameters, resulting in an R_{wp} = 6.97 %.

Table S1: R_{wp} of different directions of the stated irreps. NB: The central column (with OPDs (a,a,0) and (a,b;a,b;0,0) does not correspond to any real OPD, however the effect could be achieved by the coupling of two irreps

Irrep	OPD R_{wp}		
-	(a,0,0)	(a,a,0)	(a,a,a)
R_5^-	20.10	20.39	19.91
-	(a,b;0,0;0,0)	(a,b;a,b;0,0)	(a,b;a,b;a,b)
X_5^+	17.69	13.19	16.0
X_5^-	21.50	12.58	15.11
M_5^+	16.53	12.71	15.84
M_5^-	21.87	14.25	17.60
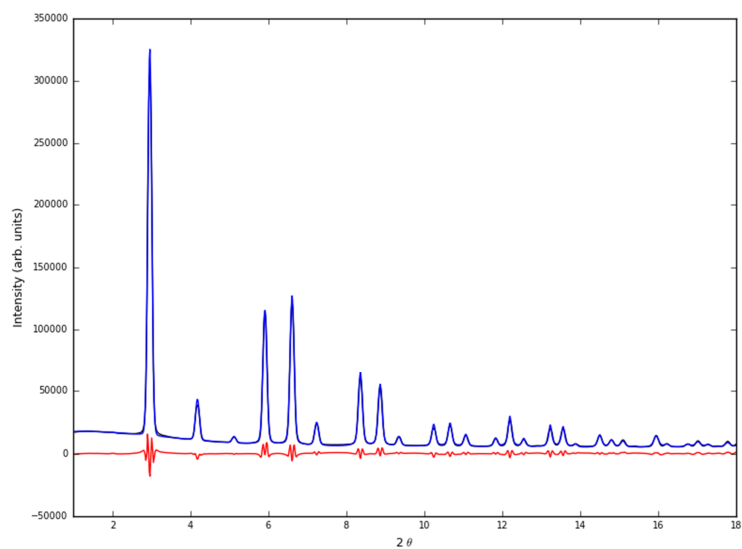
Figure S6: Rietveld fit of ScF_3 X-ray powder diffraction data at 125 K, collected at the P02.1 beamline at PETRA III, DESY using a wavelength of 0.207 Å. The data was fit with the $Pm\overline{3}m$ average structure of ScF_3 using anisotropic atomic displacement parameters, resulting in an R_{wp} = 5.7 %.
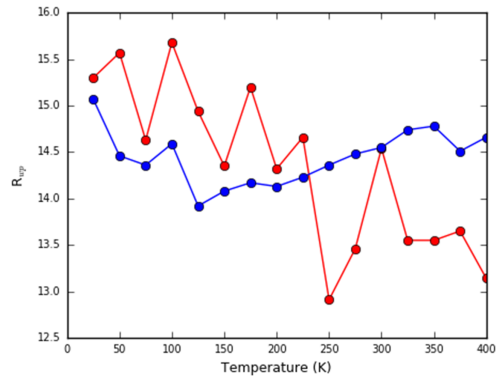
Figure S7: Comparison of fits for $X_5^+ \oplus R_5^-$ using a coupled (red) and a 2 phase model (blue) for $CaZrF_6$

Appendix B

Supplementary Material for "Soft mode anisotropy in negative thermal expansion material ReO$_3$"

Supporting Information for Soft mode anisotropy in negative thermal expansion material ReO₃

Tobias A. Bird, Mark G. L. Wilkinson, David A. Keen, Ron I. Smith
Nicholas C. Bristowe, Martin T. Dove, Anthony E. Phillips, Mark S. Senn

August 4, 2021
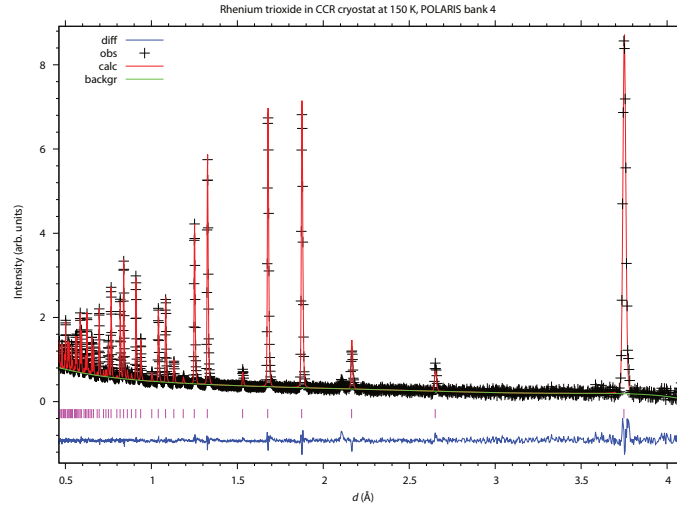
Figure 1: A Rietveld fit to the neutron powder diffraction data at 150 K, here only showing data collected on Bank 4 of Polaris. The model was refined simultaneously against data from detector banks 3–5 using the EXPGUI interface to GSAS.
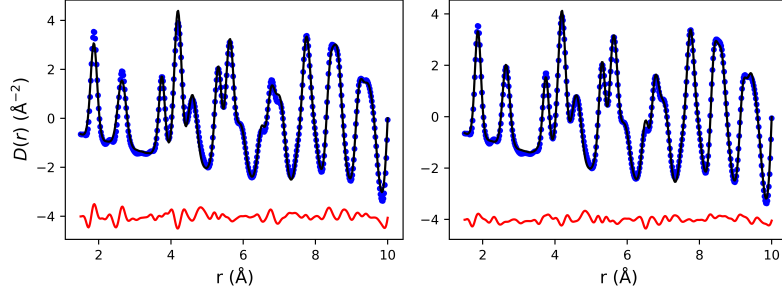
Figure 2: Fits to the 293 K PDF of ReO$_3$ for the average structure (left) and the $P4/mbm$ phase (right). The calculated PDF is shown in black, and the difference between calculated and observed is shown in red with a -4 offset. Both refinements were performed using the Topas Academic v6 software.
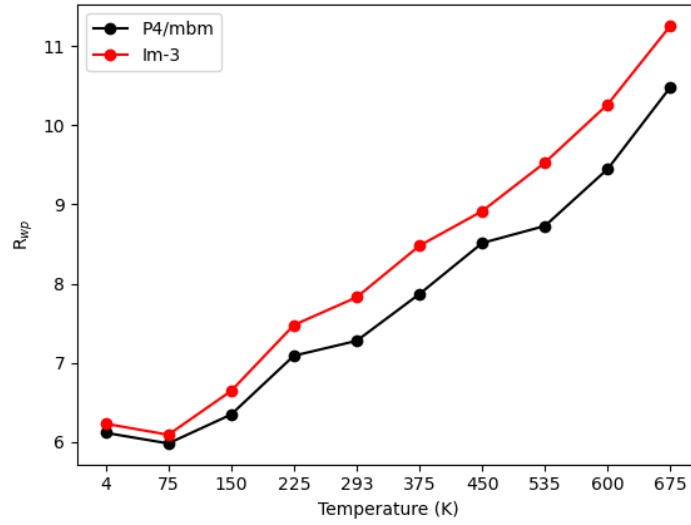
Figure 3: A plot showing the R_w of the $P4/mbm$ and $Im\bar{3}$ OPDs of the M$_2^+$ irrep against temperature, refined against the ReO$_3$ neutron PDF data using Topas Academic v6 software.
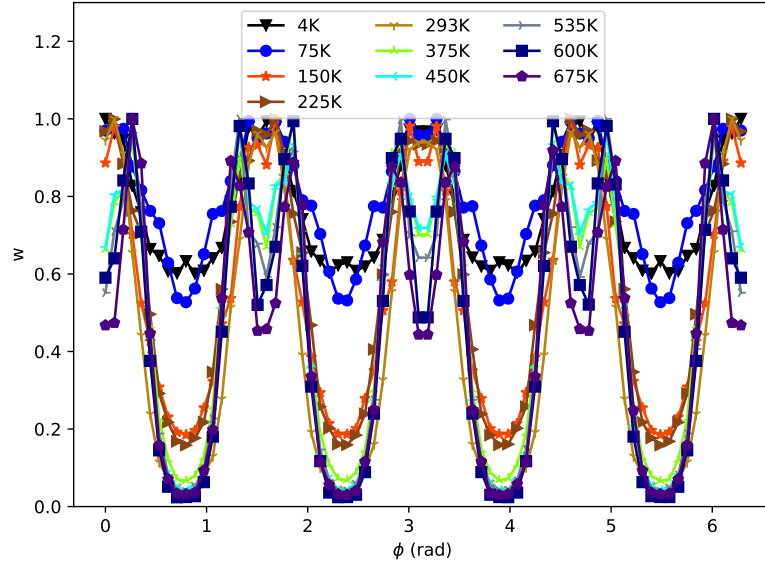
Figure 4: Cut-throughs of the spherical polar parameterisation plots in figure 5 for fixed $\theta = \pi/2$. The value plotted is $w = \exp[(R_{min} - R_i)/0.1]$, where R_{min} is the minimum R_w for each temperature and the R_i are the R_w of each refinement. A value of $w = 1$ then indicates a refinement with a fitting statistic equal to the best fitting statistic across all refinements for that temperature.
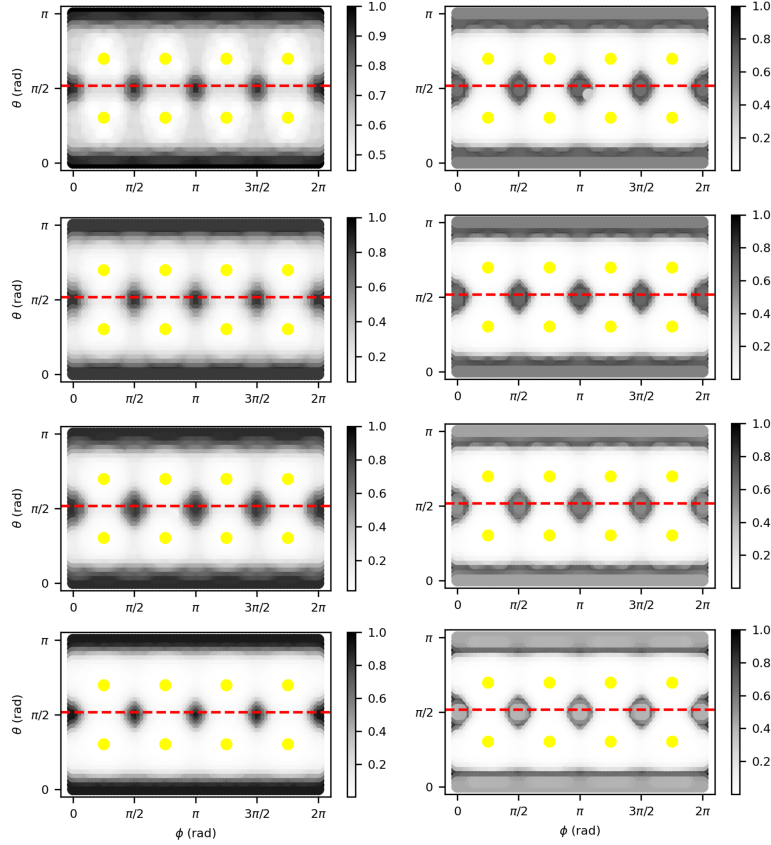
Figure 5: Plots showing the R_w of different M_2^+ OPDs parameterised by spherical coordinates. The greyscale color map corresponds to a value $w = \exp[(R_{min} - R_i)/0.1]$ where R_{min} is the minimum R_w for each temperature and the R_i are the R_w of each refinement. A value of $w = 1$ then indicates a refinement with a fitting statistic equal to the best fitting statistic across all refinements for that temperature. Thus, darker regions represent better fits than lighter regions. The left column shows temperatures 4, 150, 225 and 293 K in order, and the right shows temperatures 375, 450, 535 and 675 K in order.
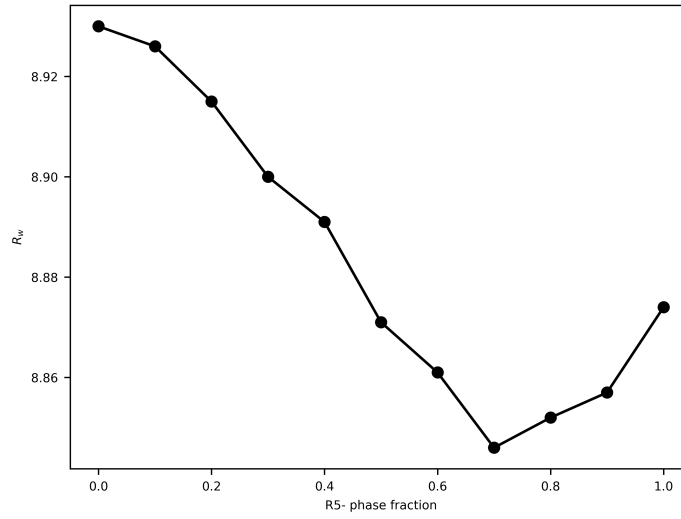
4

Figure 6: A plot showing the change in R_w for the 600 K neutron PDF for ReO$_3$ whilst performing two-phase refinements of a large amplitude M$_2^+$ (a;0;0) mode with smaller amplitude perpendicular tilt modes transforming as the M$_2^+$ irrep in one phase, and as the R$_5^-$ irrep in the other. All refinements have an additional 3 parameters compared to the single phase $P4/mbm$ refinements shown in figure 3, and show an improvement from the R_w of 9.45 % for the single phase model at 600 K.

Appendix C

Supplementary Material for "Large dynamic scissoring mode displacements coupled to band gap opening in Hybrid Perovskites"

Supporting Information for Large dynamic scissoring mode displacements coupled to band gap opening in Hybrid Perovskites

Tobias A. Bird, Junsheng Chen, Manila Songvilay, Chris Stock,
Michael T. Wharmby, Nicholas C. Bristowe and Mark S. Senn
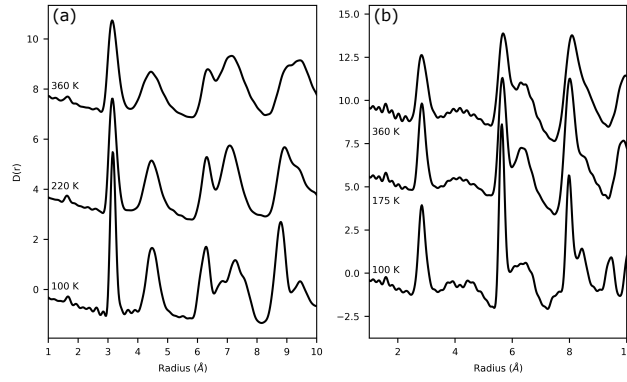
August 13, 2021

Figure 1: Plots of the MAPbI$_3$ (a) and MAPbCl$_3$ (b) PDFs at the different indicated temperatures, showing the different structural phases. The peak positions from the tetragonal phase of MAPbI$_3$ persist in the cubic phase. The peak positions from the orthorhombic phase of MAPbCl$_3$ persist in both the tetragonal and cubic phases. The PDFs are shown with an offset to aid comparison.
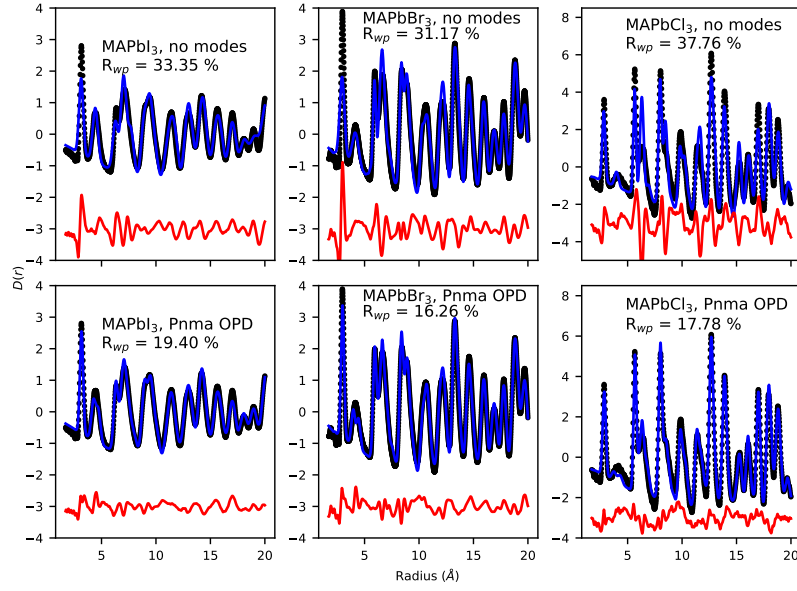
Figure 2: Fits with no modes active and with the X_5^+ OPD with $Pnma$ symmetry to the lowest temperature PDFs in the cubic phase for each compound (340, 250 and 180 K for X = I, Br and Cl, respectively). The data is shown as black circles, the calculated PDF as a blue line and the difference between the two is shown as a red line, with a -3 offset.
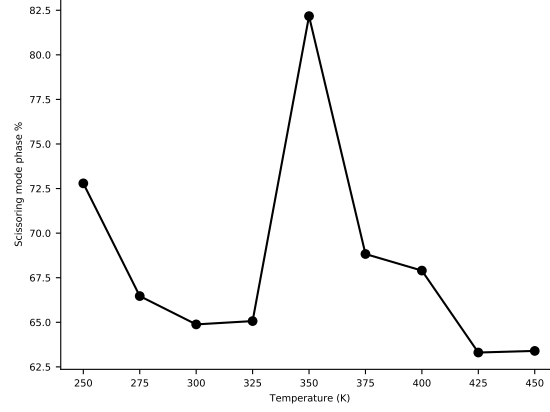
Figure 3: A plot of the X_5^- phase percentage for a competitive two-phase refinement for MAPbBr$_3$, with a general X_5^- OPD in one phase, as a pure scissoring mode, and general M_2^+ and R_5^- OPDs in the other phase.
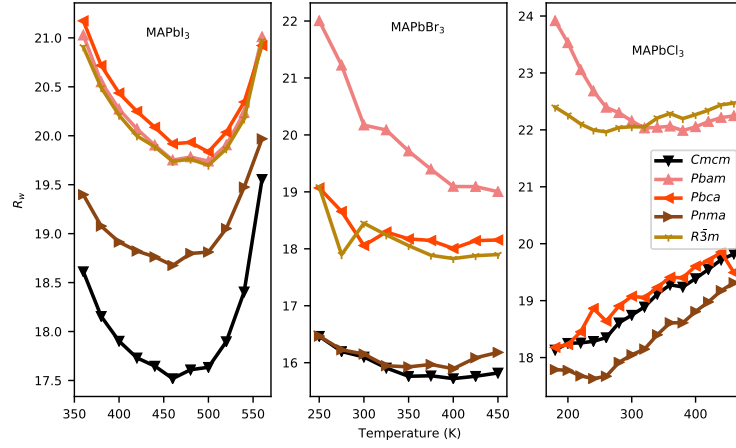

Figure 4: A plot showing the R_w vs. temperature for OPDs with different symmetries for the three studied compounds. All OPDs have 5 or fewer parameters. OPDs with 5 or fewer parameters that have a symmetry corresponding to a space group which has a group-subgroup relationship with one of the plotted symmetries are omitted.
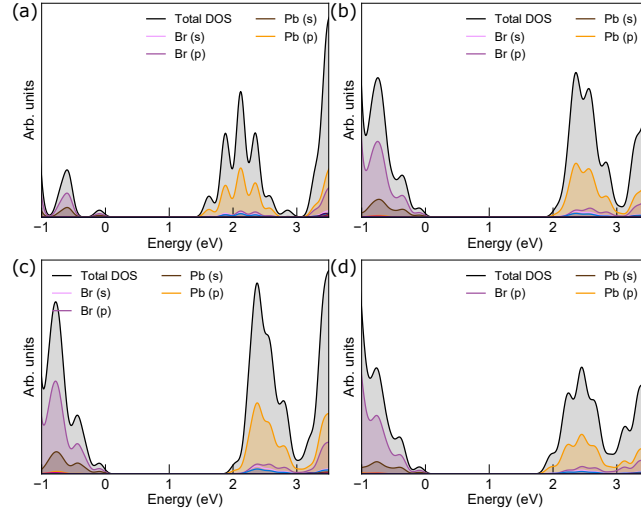
3

Figure 5: Partial electronic Density of States plots for FrPbBr$_3$ for the undistorted structure (a), $0.8\times$ X$_5^+$ $Pnma$ (b) and $Cmcm$ (c) distortions and a $1.1\times$ X$_5^-$ $C2/c$ distortion (d).
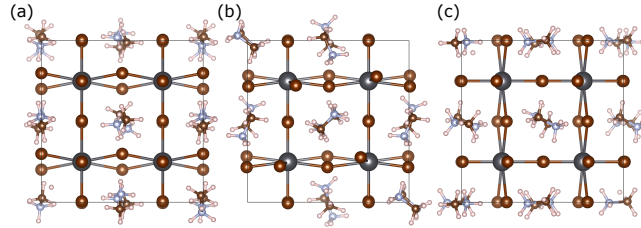

Figure 6: A diagram showing the relaxed alignments of the MA cations after a simulation of MAPbBr$_3$, with an X$_5^+$ distortion with $Pnma$ symmetry frozen in, with an amplitude $0.8 times$ the maximum amplitude.

Table 1: A table showing the structure of MAPbBr$_3$ with the OPD with *Pnma* symmetry frozen in. The distortion has an amplitude of 0.8× its maximum value. This maximum value is $\sqrt{2}\times$ the refined amplitude. The coordinates shown are fractional.

Atom Type	Multiplicity	Wyckoff Label	x	y	z
Fr	4	b	0	0	0.5
Fr	4	a	0	0	0
Pb	4	c	0.75	0.25	0.75
Pb	4	c	0.75	0.25	0.25
Br	4	c	0.70427	0.25	0.50711
Br	4	c	0.70427	0.25	0.00711
Br	4	c	0.99119	0.25	'0.75
Br	4	c	0.99917	0.25	0.25
Br	8	d	0.28786	0.5	0.18254

Table 2: A table of the C–N bond directions in a simulation of MAPbBr$_3$ with the OPD with *Pnma* symmetry frozen in. The distortion has an amplitude of 0.8× its maximum value. This maximum value is $\sqrt{2}\times$ the refined amplitude. The coordinates shown are fractional. Initially, all bonds were aligned along the [1 0 0] direction. The vectors shown are unit vectors in the direction from C to N.

Position			Direction		
x	y	z	x	y	z
1/2	1/2	1/2	0.597	-0.379	0.707
1/2	1/2	0	-0.853	0.459	-0.246
1/2	0	1/2	-0.733	-0.129	-0.668
0	1/2	1/2	-0.855	0.468	0.223
0	0	0	-0.572	-0.044	0.819
0	1/2	0	0.684	-0.058	-0.728
1/2	0	0	0.897	0.082	0.433
0	0	1/2	0.900	0.067	-0.431